

A Thesis Submitted for the Degree of PhD at the University of Warwick

Permanent WRAP URL:

<http://wrap.warwick.ac.uk/101295>

Copyright and reuse:

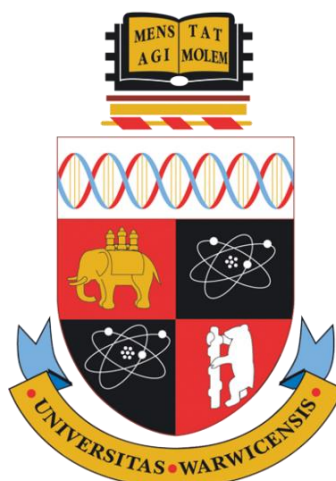
This thesis is made available online and is protected by original copyright.

Please scroll down to view the document itself.

Please refer to the repository record for this item for information to help you to cite it.

Our policy information is available from the repository home page.

For more information, please contact the WRAP Team at: wrap@warwick.ac.uk



**Innovative Approaches towards Understanding the
Dissolution and Growth of Active Pharmaceutical
Ingredients**

by

Faduma Mohammed Maddar

Thesis

*Submitted to the University of Warwick for the degree of
Doctor of Philosophy in Chemistry with Industrial Collaboration*

Department of Chemistry

September 2017



*For my family,
gaar ahaan hooyo iyo aabo.*

CONTENTS

List of Figures.....	vi
List of Tables	xiv
Abbreviations	xv
Acknowledgements.....	xvii
Declaration.....	xviii
Abstract.....	xx
Chapter 1: Introduction	1
1.1. Crystal Dissolution	2
1.2. Solubility Improvements.....	3
1.3. Nucleation and Growth of Crystals	12
1.4. Crystal Growth/Dissolution Reactions	16
1.5. Traditional Dissolution Testing	20
1.6. Scanning Probe Microscopies (SPMs)	22
1.6.1. Atomic Force Microscopy	22
1.6.2. Scanning Electrochemical Microscopy	25
1.6.3. Scanning Ion-conductance Microscopy	28
1.6.4. Scanning Electrochemical Cell Microscopy	30

1.7.	Nanopipettes	32
1.8.	Resistive Pulse Detection.....	33
1.9.	Research Aims	35
1.10.	References.....	37
Chapter 2: Experimental.....		53
2.1.	Chemicals.....	54
2.2.	Carbon Electrodes	55
2.2.1.	Highly Oriented Pyrolytic Graphite (HOPG)	55
2.2.2.	Polycrystalline Boron-Doped Diamond (pBDD)	56
2.3.	Macroscale Electrochemistry.....	57
2.4.	Quad-Probe Fabrication.....	58
2.5.	Preparation of Bicalutamide Microcrystals	59
2.6.	Peak Force Tapping Atomic Force Microscopy	60
2.7.	References.....	61
Chapter 3: Dissolution of Bicalutamide Single Crystals in Aqueous Solution: Significance of Evolving Topography in Accelerating Face-Specific Kinetics ...		62
3.1.	Introduction.....	64
3.2.	Experimental Section.....	66
3.2.1.	Solutions and Sample Preparation	66
3.2.2.	X-ray Characterization.....	66

3.2.3.	<i>In Situ</i> Atomic Force Microscopy.....	67
3.2.4.	Finite Element Method Simulations	68
3.3.	Results and Discussion	71
3.3.1.	Bicalutamide Crystals	71
3.3.2.	Dissolution Rates and Surface Dynamics	74
3.3.3.	Determination of Interfacial Concentrations and Kinetic Regime.....	86
3.4.	Conclusions.....	89
3.5.	Supporting Information.....	91
3.5.1.	Interfacial Concentration Values	91
3.6.	References.....	92

**Chapter 4: Functional Multimicroscopy Approach to Assess the Dissolution
Performance of Amorphous Solid Dispersions (ASDs) 96**

4.1.	Introduction.....	97
4.2.	Experimental Section.....	99
4.2.1.	Solutions and Sample Preparation	99
4.2.2.	Optical Microscopy.....	99
4.2.3.	<i>In situ</i> Atomic Force Microscopy	99
4.2.4.	Raman Spectroscopy.....	100
4.2.5.	Quad-Probe Fabrication	100
4.2.6.	Electrochemistry	100

4.3.	Results and Discussion	101
4.3.1.	Optical Microscopy.....	101
4.3.2.	Topographical Changes: <i>In situ</i> Atomic Force Microscopy Analysis.....	102
4.3.3.	Raman Spectroscopy.....	103
4.3.4.	<i>In situ</i> Electrochemical Monitoring of Initial Dissolution...	105
4.4.	Conclusions.....	110
4.5.	References.....	110
 Chapter 5: Confined Crystallization of Organic Materials in Nanopipettes: Tracking the Early Stages of Crystal Growth and Making Seeds for Unusual Polymorphs		115
5.1.	Introduction.....	116
5.2.	Experimental Section.....	119
5.2.1.	Materials and Solutions	119
5.2.2.	Nanopipettes	119
5.2.3.	BIC Crystallization Measurements	120
5.2.4.	Raman Spectroscopy.....	121
5.2.5.	Finite Element Method Simulations	121
5.3.	Results and Discussion	125
5.3.1.	Crystallization of Bicalutamide in a Nanopipette.....	125
5.4.	Conclusions.....	139

5.5.	Supporting Information.....	140
5.5.1.	Finite Element Method Simulations	140
5.5.2.	Diffusion Coefficients.....	142
5.6.	References.....	143
 Chapter 6: Electrochemical oxidation of dihydronicotinamide adenine dinucleotide (NADH): Comparison of highly oriented pyrolytic graphite (HOPG) and polycrystalline boron-doped diamond (pBDD) electrodes 148		
6.1.	Introduction.....	149
6.2.	Experimental Section.....	151
6.2.1.	Materials and Solutions	151
6.2.2.	Macroscale Electrochemistry	152
6.2.3.	Scanning Electrochemical Cell Microscopy	153
6.2.4.	Atomic Force Microscopy	156
6.3.	Results and Discussion	156
6.3.1.	Voltammetry of NADH Oxidation on HOPG and pBDD ...	156
6.3.3.	Adsorption Behavior of NADH on HOPG	161
6.3.4.	High Resolution Imaging of Electrochemical Activity	164
6.4.	Conclusions.....	168
6.5.	References	169
 Chapter 7: Conclusions 174		

List of Figures

Figure 1.1. Biopharmaceutics classification system.	3
Figure 1.2. Solubility versus pH.....	5
Figure 1.3. Representation of API cocrystal.	6
Figure 1.4. Representation of structural polymorphism.....	8
Figure 1.5. Energy versus temperature diagram of (i) monotropic system and (ii) enantiotropic where T_p is the transition temperature.....	8
Figure 1.6. Energy states of polymorphs explaining Ostwald's rule of stages.	9
Figure 1.7. Representation of the composition of ASD.	11
Figure 1.8. (a) Formation of a spherical nucleus of radius r . (b) Total free energy as a function of the radius r of the cluster.	15
Figure 1.9. Schematic of the elementary steps involved in dissolution processes....	16
Figure 1.10. Concentration profiles under different dissolution modes: (i) diffusion rate controlled; (ii) mixed rate control and (iii) reaction rate controlled dissolution.	17
Figure 1.11. Kossel model of a crystal surface.	19
Figure 1.12. (a) Macrocrystal showing predominantly planar diffusion and (b) microcrystal showing predominantly hemispherical diffusion. Diagrams not to scale.	20
Figure 1.13. Illustration of dissolution Apparatus I (Basket) and II (Paddle).....	21
Figure 1.14. (a) Schematic of the key features of an AFM, (b) different modes of AFM and (c) shows the force-distance curve.	25

Figure 1.15. Schematic of the principles of SECM showing hemispherical diffusion of the tip far away from the substrate surface, blocking of diffusion by insulating substrate and positive feedback at a conductive substrate.	27
Figure 1.16. Schematic of SICM set-up.	28
Figure 1.17. Schematic of SECCM setup. Theta pipette is used to create a tiny meniscus electrochemical cell on a substrate. The working electrode size is determined by the size of the pipette opening and meniscus wetting of the substrate.	31
Figure 1.18. (a) Schematic mechanistic of the laser puller used to make the sharp nanopipette tips. (b) Illustration of the several types of nanopipettes that can be made with different capillaries.	33
Figure 1.19. Schematic showing how nanopipettes can act as resistive pulse sensors. When a particle moves towards the pore the system feels an increase in resistance resulting in a drop in current as the particle translocates the pore.	34
Figure 2.1. Structural illustration of HOPG.	55
Figure 2.2. (a) Schematic diagram of the in-house fabricated pBDD electrode. (b) An optical microscope image of pBDD electrode face with a diameter of 1 mm.	57
Figure 2.3. Schematic of the Teflon cell used to hold solution on HOPG with a defined contact area.	58
Figure 2.4. Schematic of the carbon deposition process for the fabrication of a quad-probe. Butane is passed through the pulled pipet barrels and pyrolyzed using a hand held butane torch under an argon atmosphere.	59
Figure 2.5. Optical images of BIC crystals	60
Figure 2.6. (i) Plot of fore and z position as a function of time. (ii) Force versus Z position, typical force curve performed at every pixel position on the sample surface.	61

Figure 3.1. Three-dimensional domain (not to scale) used for FEM simulations of BIC dissolution. The numbers correspond to the boundaries described in Table 3.1.	68
Figure 3.2. Crystal morphology of BIC (Form I). (a) Bright field microscopy image of a typical grown crystal acquired normal to the (100) face. (b) Representation of the single crystal X-ray diffraction of BIC with crystal faces assigned. Red line represents the 2D crystal outline.	71
Figure 3.3. Comparison of calculated and experimental PXRD patterns of BIC polymorph I.....	72
Figure 3.4. (a) AFM images of a single BIC microcrystal (initially 36 μm in length and 10.5 μm in width) during dissolution in aqueous solution. (b) 2D BIC crystal morphology indicating how displacement data were extracted. (c) Plot showing the changes in width and length over time of the dissolving BIC crystal shown in (a)...	76
Figure 3.5. (a) Plots showing changes in crystal dimensions over time: (i) Height (100), (ii) Width $\{051\}$ and (iii) Length $\{\bar{1}02\}$. (b) Corresponding dissolution rates (flux) over time: (i) Height (100), (ii) Width $\{051\}$ and (iii) Length $\{\bar{1}02\}$. Data are fitted to an exponential function (solid red curves) and the blue linear portions highlight the change in the rate for the basal surface and roughened surfaces at early and advanced dissolution times. (c) Plot showing the change in surface roughness of (100) face normalized by the geometric surface area as a function of time.	78
Figure 3.6. Graphs showing cross-sections of dissolved BIC crystals at various time points.....	80
Figure 3.7. AFM topography images of aqueous dissolution sequence of 3 different single BIC crystals.	81
Figure 3.8. Plots showing changes in crystal dimensions over time of the crystals shown in Figure 3.7.....	82

Figure 3.9. Corresponding dissolution rates (flux per unit area) over time of the crystals shown in Figure 3.7.	82
Figure 3.10. Structure of BIC crystal faces: (a) (100), (b) ($\bar{1}02$) and (c) (051). Black dotted lines highlight hydrogen bonds. Acquired using Mercury 3.8, CCDC Cambridge using the structure JAYCES.....	85
Figure 3.11. FEM simulation for the dissolution of a BIC crystal in bulk aqueous solution at different time points: (a) model formulated from experimental data. (b) a MT1 model where the dissolution of all faces is purely diffusion-controlled; and (c) MT2 model where only the {051} and { $\bar{1}02$ } faces are diffusion-controlled and the (100) face dissolves as observed experimentally. Note the difference in the concentration ranges for (a) and (b)-(c)	88
Figure 3.12. Comparative plots of J_{MT}/J_{obs} versus time for the (100) faces (black), {051} faces (red) and { $\bar{1}02$ } faces (blue), showing the extent to which each face evolves towards increasing mass transport contribution during dissolution in the case where all the crystal faces are diffusion-limited (MT1) and where only the {051} and { $\bar{1}02$ } faces are diffusion-limited (MT2).	89
Figure 4.1. Optical microscope images taken before and after the addition of water to the two formulations of amorphous solid dispersions. (a) 15 % felodipine ASD and (b) 50 % felodipine ASD (i) represents dry sample and (ii) when in contact with water.	102
Figure 4.2. Series of <i>in situ</i> AFM images over time showing the recrystallization of felodipine during the aqueous dissolution of 50% felodipine ASD.....	104
Figure 4.3. Raman spectra relative to the aqueous dissolution of: (a) (i) 15% felodipine and (b) (i) 50% felodipine ASD over time. Spectrum in red highlights Raman signal of crystalline felodipine for comparison. (b) (ii) (iii) show the peak height intensity of amorphous felodipine and copovidone as a function of time.	104

Figure 4.4. (a) Rotating disk electrode voltammogram run on glassy carbon electrode of 3 μM felodipine solution containing 100 mM KCl. (b) Shows the current response of a carbon quad probe ($\sim 10\ \mu\text{m}$ diameter) in 1 mM FcTMA⁺ containing 100 mM KCl. (c) CV of saturated felodipine solution containing 100 mM KCl at 100 mVs^{-1} 107

Figure 4.5. (a) Schematic of the electrochemical quad-probe. The probe moves down so that the meniscus is in contact with the amorphous solid surface. Carbon electrodes detect the release of felodipine upon water contact and the QRCEs in the open barrels in the probe act as the reference/counter electrodes. (b) (i) SEM micrograph of the end of a typical quad-probe showing carbon electrodes (top and bottom) and open barrels (left and right). (ii) Optical microscope image of the probe tip positioned above a single solid before landing. (c) (i) Current-potential response recorded at the quad-probe during approach and after the meniscus came into contact with the surface of the ASD containing (a) 15 % felodipine and (b) 50 % felodipine..... 109

Figure 5.1. Schematic representation of the free energy profiles for two competing nuclei corresponding to polymorphs A and B, over a range of sizes..... 116

Figure 5.2. Schematic showing the crystallization of bicalutamide in a nanopipette. 118

Figure 5.3. Using the same experimental setup as shown in Figure 5.4 and having no BIC in the bath solution, the stability of the Ag wire-coated Ag/AgCl in DMSO was measured by recording the potential of the electrode over time. 121

Figure 5.4. UV-Vis spectra of BIC dissolved in different ratios of DMSO: H₂O solutions. 124

Figure 5.5. Setup (not to scale) for voltage dependent nucleation of BIC in conical nanopipettes. A bias was applied between an electrode in a nanopipette containing aqueous electrolyte and an electrode in DMSO solution containing BIC. The current response was measured as a function of time and applied potential..... 126

Figure 5.6. Current-time response with 5 mM BIC in the DMSO bath at different potentials applied to the tip with respect to the Ag/AgCl electrode in bulk: (a) (i) -0.3 V, with inset (ii) showing expanded view of highlighted event; (b) -0.1 V; and (c) -0.5 V.....	127
Figure 5.7. Current-time response at 0.3 V with different concentrations of BIC in the DMSO bath; 5mM, 10 mM and 20 mM. Shown are 3 sets of repeats (i-iii) for each concentration.	129
Figure 5.8. Current-time response at a nanopipette electrode potential of -0.3 V for: (a) (i) no BIC in DMSO and (b) (i) 200 mM BIC in DMSO. Corresponding <i>I-V</i> curves of each nanopipette prior to current-time measurements are shown in (a) (ii) and (b) (ii).	130
Figure 5.9. Water-DMSO mixing near the mouth of the nanopipette and the subsequent transfer and protonation of BIC in the water phase.....	132
Figure 5.10. Current-time response at a nanopipette electrode potential of -0.3 V using 10 mM TBA ⁺ Cl ⁻ in each phase and 5 mM BIC in the DMSO phase. Expanded views of highlighted events (1-3) are shown.....	133
Figure 5.11. Concentration profiles of water, DMSO and BIC saturation levels ($\Omega = [\text{BIC}]_{\text{total}} / [\text{BIC}]_{\text{sat}}$) at times of 0 ms, 1 ms, 10 ms and 100 ms after immersing a nanopipette containing aqueous electrolyte into DMSO (5 mM BIC and electrolyte). Nanopipette electrode bias of -0.3 V.....	134
Figure 5.12. Predicted BIC saturation levels with a bias of -0.3 V (a) and +0.3 V (b) applied to the upper nanopipette boundary. Simulations were performed in 100 mM TBA ⁺ Cl ⁻ with 5 mM BIC in the DMSO phase initially.	135
Figure 5.13. Single molecule diagrams of bicalutamide form I and II.	136
Figure 5.14. (a) Optical image of a typical nanopipette used in time-current measurements with 200 mM BIC in bath showing the formation of crystals inside the	

tip. (b) Additional formation of crystals in the bath containing 200 mM BIC after a nanopipette crystallization experiment. (c) Raman spectrum of BIC crystals formed, with main peak positions marked. The peaks highlighted at 1582 and 1600 cm^{-1} are most useful in resolving the BIC crystal type. 138

Figure 5.15. Schematic of FEM simulation domain with applied boundary conditions. 141

Figure 6.1. Schematic of the SECCM setup in which a theta pipette was used to create a tiny meniscus electrochemical cell on a carbon electrode surface (HOPG or pBDD) with the working electrode size determined by the size of the pipette opening and meniscus wetting of the substrate. An ion conductance current (i_{DC}) was generated by the potential bias, V_1 , between the two barrels of the pipette, while the voltage, V_2 , provided additional control of the potential of the working electrode. The resulting electrochemical current, i_{sub} , was measured to determine the local electroactivity. The conductance current has an AC component (see text for details), at the frequency of the pipette. 155

Figure 6.2. Oxidation of 1 mM NADH in 0.1 M PBS at various potential scan rates: 50, 100, 200, 400, 600 and 800 mV s^{-1} . For (a) pBDD and (b) ZYB the surface was cleaned or cleaved, respectively, prior to the first 50 mV s^{-1} scan, after which subsequent scans at increasing scan rates were run without further pretreatment or preparation of the electrode surface. For (c) pBDD* and (d) ZYB*, each voltammetric scan was made on a freshly polished pBDD or a freshly cleaved HOPG surface. The insets show plots of peak current vs. the square root of scan rate. 158

Figure 6.3. Repetitive cyclic voltammograms for the oxidation of 1 mM NADH on (a) AM, (b) ZYB, (c) SPI-3 grade HOPG and (d) pBDD in 0.1 M PBS, at a potential sweep rate of 100 mV s^{-1} . Each voltammogram was run with a 5 s interval between for a total of 10 cycles..... 160

Figure 6.4. AFM topography images of freshly cleaved HOPG: (a) AM, (b) ZYB and (c) SPI-3 grades..... 161

Figure 6.5. Oxidation of 5 μM NADH in 0.1 M PBS at various scan rates: 50, 100, 200, 400, and 600 mV s^{-1} at (a) (i) AM (b) (i) ZYB and (c) (i) SPI-3. (a-c) (ii) Plots of current density (forward wave) against scan rate and (a-c) (iii) variation of forward peak charge with the log of scan rate for the 3 different HOPG grades. 163

Figure 6.6. (a) SECCM CVs for the oxidation of 1 mM NADH in 0.1 M PBS at 100 mVs^{-1} . SECCM maps of (b) surface electrochemical activity and (c) conductance current (DC component) recorded at the half-wave potential for the oxidation of 1 mM NADH at HOPG (AM), obtained with a ca. 400 nm diameter pipette..... 165

Figure 6.7. (a) (i) Optical microscope image of the pBDD substrate, taken using the in-rig camera before performing the SECCM map and (ii) after scan. (iii) FE-SEM micrograph of the scanned area, covered by spots of reaction products formed during each local voltammetric scan. (iv) FE-SEM micrograph showing a zoom of typical spots after hopping voltammetric mode SECCM imaging. (b) (i) FE-SEM image of the same area of pBDD after cleaning to remove the adsorbed material. (ii-iv) Snapshot SECCM electrochemical maps ($60\text{ }\mu\text{m} \times 45\text{ }\mu\text{m}$) at different potentials, as marked above each map. 167

List of Tables

Table 2.1. List of chemicals used in this thesis.	54
Table 3.1. Boundary conditions applied to the numerical models as defined in Figure 3.1, where \mathbf{n} denotes the outward vector normal to the boundary, c_{bulk} is the bulk concentration (0 μM) and c_{sat} is the saturation solubility of 11.6 μM	70
Table 3.2. Crystal data and structure refinement for BIC	72
Table 3.3. Concentration near the crystal/solution interface and normal total fluxes at various times for the different crystal faces calculated from FEM simulations.	91
Table 5.1. Solubility concentrations of BIC	125
Table 5.2. Diffusion coefficients of H_2O and DMSO in different compositions of DMSO and H_2O , ⁵⁹ as used for FEM simulations.....	142
Table 5.3. Calculated Diffusion coefficients of bicalutamide in H_2O and DMSO using the Wilke Chang equation. ⁶⁰	143

Abbreviations

AC Alternating Current

AFM Atomic Force Microscopy

API Active Pharmaceutical Ingredient

ASD Amorphous Solid Dispersion

BCS Biopharmaceutics Classification System

BIC Bicalutamide

BM-SICM Bias Modulated Scanning Ion Conductance Microscopy

BPPG Basal plane pyrolytic graphite

CCD Charge Coupled Device

CV Cyclic Voltammogram

DC Direct Current

DM-SICM Distance Modulated Scanning Ion Conductance Microscopy

DNA Deoxyribonucleic acid

DOS Density of Electronic States

FDA Food and Drug Administration

FEM Finite Element Method

FE-SEM Field Emission-Scanning Electron Microscopy

FIB-SEM Focused Ion Beam-Scanning Electron Microscopy

EPPG Edge Plane Pyrolytic Graphite

FPGA Field Programmable Graphics Array

HOPG Highly Oriented Pyrolytic Graphite

IDR Intrinsic Dissolution Rate

I-V Current-Voltage

I-t Current-Time

NADH Nicotinamide Adenine Dinucleotide, Reduced

pBDD Polycrystalline Boron Doped Diamond

PBS Phosphate Buffer Saline

QRCE Quasi-Reference Counter Electrode
SECCM Scanning Electrochemical Cell Microscopy
SECM Scanning Electrochemical Microscopy
SICM Scanning Ion Conductance Microscopy
SPM Scanning Probe Microscopy
STM Scanning Tunneling Microscope
SG/TC Substrate Generation/Tip Collection
TEM Transmission Electron Microscopy
TG/SC Tip Generation/Substrate Collection
UME Ultra-Microelectrode
USP United States Pharmacopeia
UV Ultraviolet
UV-Vis Ultraviolet–visible

Acknowledgements

I would like to sincerely thank my supervisor, Prof Patrick Unwin for giving me the opportunity to be part of Warwick Electrochemistry and Interfaces Group and undertake this research project. I highly appreciate his valuable guidance and encouraging charisma throughout the years. I have truly learnt a lot. My interest in pursuing this field has initiated from him together with Prof Julie Macpherson, who taught me electrochemistry in my master's studies. I highly acknowledge their excellent teaching and enthusiasm for the subject.

From AstraZeneca, I would like to thank Dr Leslie Hughes and Dr Stephen Warren for their consistent feedback and guidance. I also thank AstraZeneca, MOAC Doctoral Training Centre and EPSRC, for funding this work.

I appreciate the expertise and advice from current and past group members of Warwick Electrochemistry and Interfaces Group. Thanks to Guohui Zhang, Robert Lazenby, David Perry, and Ashley Page. And of course, to all of the group members for their willingness to share and help at all times.

Special thanks to Maria Adobes-Vidal, Emma Ravenhill and Sze-Yin Tan for making that 4 o'clock coffee time funnily crazy. I am glad to have shared this journey with you all, full of enjoyable cherished moments. Also, a special mention goes to Minkyung Kang and Cameron Bentley for always sharing one or two "dank memes", bringing laughter to all times. Cheers guys for expressively being my meme dealers. And thank you all for being great friends.

Finally, I want to thank my family for making these challenging years more bearable. Your patience and support has been limitless. I am so grateful for all that you have done for me. I dedicate this thesis to you as a sign of love from me.

(Oh...Little bro Omar, keep on reading the rest of this thesis).

Declaration

This thesis is submitted to the University of Warwick in support of my application for the degree of Doctor of Philosophy. I confirm that this thesis has not been submitted for any degree at another University.

The work presented in this thesis is entirely original and my own work, except where acknowledged below.

Chapter 3 was published as:

F. M. Maddar, [†] M. Adobes-Vidal, [†] L. P. Hughes, S. A. Wren and P. R. Unwin. *Cryst. Growth & Des.* **2017**, 10.1021/acs.cgd.7b00401

[†] Contributed equally to this work. M. Adobes-Vidal performed the finite element method simulations presented in this work. This manuscript also formed a chapter in M. Adobes-Vidal's thesis.

Chapter 4 finalized for submission as:

F.M. Maddar, L. P. Hughes, S. A. Wren and P. R. Unwin. *J. Pharm. Sci.* **2017**.

Chapter 5 was published as:

F. M. Maddar, D. Perry and P. R. Unwin. *Growth & Des.* **2017**.

D. Perry performed the finite element method simulations presented in this work.

Chapter 6 was published as:

F. M. Maddar, R. A. Lazenby, A.N. Patel and P. R. Unwin. *Phys. Chem. Chem. Phys.* **2016**, 18, 26404-26411.

Additionally, I have contributed to the following papers whose results are not featured in this thesis:

M. Adobes-Vidal; **F. M. Maddar**; D. Momotenko; L. P. Hughes; S. A. Wren; L. N. Poloni; M. D. Ward; P. R. Unwin. *Cryst. Growth Des.* **2016**, 16, 4421-4429.

C. L. Bentley; M. Kang; **F. M. Maddar**; F. Li; M. Walker; J. Zhang; P. R. Unwin.
Chem. Sci. **2017**, 8, 6583-6593.

Abstract

Studies of the kinetics and mechanisms of the dissolution and growth of crystals and other solids are beneficial in many areas of science. In pharmaceutical science, dissolution testing is a key quality control procedure used to determine the rate at which an active pharmaceutical ingredient (API) is released and is thus available for absorption in the gastro-intestinal tract. However, the general processes governing the dissolution and growth of crystals are poorly understood despite many years of study. This thesis focuses on the implementation of various microscopy and electrochemical techniques as a novel approach to further understand the dissolution and growth of API crystals and amorphous solids. The motive of the first part of the thesis, was the use of atomic force microscopy (AFM) to obtain new insight into API dissolution and growth from both the crystalline form and amorphous solid state. Studies of the crystalline API, bicalutamide have focused on measuring the 3D morphological changes of individual microcrystals in aqueous solution, in real time, from which the intrinsic dissolution rates of each crystal surface exposed to solution have been extracted. In addition, with finite element method (FEM) modelling, interfacial concentrations around the dissolving crystal have been obtained, allowing the elucidation of the kinetic regime of the overall dissolution reaction. A major conclusion of this work is that the dissolution kinetics accelerate significantly during the process, due to changes in nanoscale features on the surface. AFM was then used to examine targeted regions of dissolving amorphous solid dispersions (ASDs), comprising of felodipine API and the water-soluble polymer copovidone, in aqueous solution, together with a localized electrochemical-droplet (flux measuring) technique and Raman spectroscopy. This multi-microscopy approach allowed real-time information about initial API release rates, and changes in solid-state composition and morphology during dissolution. This thesis then transitions to the study of nanocrystallization of APIs using nanopipettes under electrochemical control in a nanoscale anti-solvent configuration using bicalutamide, as an example system. A key feature of the technique is that a bias between an electrode in the nanopipette, and one in bulk solution, can be used to control the supersaturation level at the end of the nanopipette and the current-time response detects nucleation and growth events. Using Raman microscopy the formation of the least stable crystal polymorph of Form II was demonstrated. To highlight the generality of nanopipette-based electrochemical techniques, a final results chapter reports the use of scanning electrochemical cell microscopy (SECCM) to study the electro-oxidation of nicotinamide adenine dinucleotide (NADH), on various carbon electrodes, showing how active surface sites are readily identified and quantified.

Chapter 1

Introduction

The development of pharmaceutical compounds with important therapeutic benefits is of considerable importance. Unfortunately, many active pharmaceutical ingredients (APIs) that enter the pharmaceutical pipeline lack the desired characteristics for maximum in vivo performance, which is governed in part by dissolution of the API from a crystalline or other solid form. This chapter introduces the basic concepts of crystal dissolution and shows the importance of fundamental understanding of both crystal growth and dissolution. In addition, this chapter highlights and discusses general methods used to provide better aqueous solubility and bioavailability of pharmaceutical drugs. This chapter gives an overview of scanning probe microscopy techniques and how they can be implemented in the study of dissolution and growth of crystals which is a major focus of the work herein. Finally, a brief summary of the work undertaken in this thesis is provided.

1.1. Crystal Dissolution

Various areas of science and a number of industries require a fundamental understanding of crystal dissolution. Focusing on the pharmaceutical domain, dissolution testing is a key quality control procedure used to determine the rate at which a crystalline drug product releases an active pharmaceutical ingredient (API) in a suitable fashion, such that the API is released from the tablet into solution, and is available for absorption in the gastrointestinal tract.

However, before any absorption can take place at all, a significant property to address is solubility.¹ Solubility is the concentration of solute in a saturated solution at a defined temperature and pressure.² If a drug exhibits very low solubility in water, only small amounts of the drug will be available for diffusion and permeate across the various barriers in the living organism to reach the site of action. Hence, solubility is considered as the limiting factor in the absorption process of a poorly water soluble API and have been reported in many cases.³⁻⁸ This has led to the implementation of solubility screens in the early stages of drug design. It is estimated that ~40% or more of the new pharmaceutical products developed through drug discovery companies are poorly water soluble.^{9,10}

Together with the intestinal permeability (i.e. molecules must penetrate the biological membrane to be absorbed), the solubility behavior of an API is a key factor of its oral bioavailability.^{11,12} Thus, because of the importance of interplay between the two in biopharmaceutics of products, API candidates are classified by using the biopharmaceutics classification system (BCS) devised by Amidon *et al* in 1995¹³ (illustrated in Figure 1.1). As shown, the system defines APIs as a combination of solubility and permeability. APIs are highly soluble when the highest dose strength is soluble in 250 ml or less of aqueous media across the physiological pH range (1-7.5).^{2,14} Whereas, APIs that are insoluble in these conditions are considered to have low solubility.² Putting such system into application provides several benefits, including shortened drug product

development time and large cost savings. While the BCS provides vital information on the solubility and permeation characteristics of a drug, the intrinsic dissolution rate (IDR) is an important concept that further characterizes solution concentration of a drug.¹⁵⁻¹⁸ In pharmaceutical sciences, IDR is defined as the dissolution rate of a pure drug compound under the condition of constant surface area, agitation or stirring speed, ionic strength and pH of the dissolution medium. It is generally expressed as the mass of solute appearing in the dissolution medium per unit time, also known as dissolution flux (as the rate is normalized by surface area). Accordingly, it allows the study of the effects of surfactants and pH on the solubilization of poorly soluble drugs which can result in better correlation with *in vivo* drug dissolution rate than solubility.¹⁹

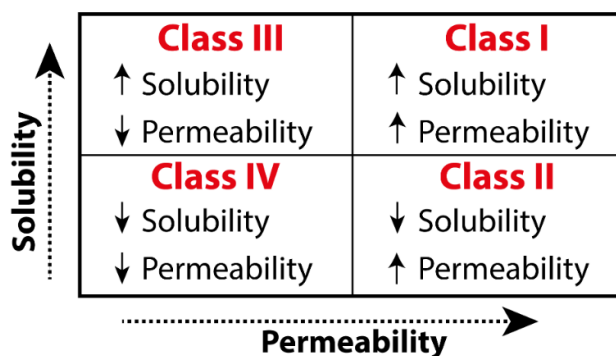


Figure 1.1. Biopharmaceutics classification system.

1.2. Solubility Improvements

As mentioned above, solubility is a major issue in the development of marketable formulations of poorly water soluble drugs.²⁰ If a drug exhibits very low solubility in water and / or if its dissolution rate at the site of administration is very low, limited amounts of drug become available for adsorption resulting in poor *in vivo*

performance. Most of the drugs are either weakly acidic or weakly basic having poor aqueous solubility, particularly class II drugs of the BCS system. Poor aqueous solubility can often be attributed to strong intermolecular forces within the crystal lattice.²¹ This will prevent molecules from escaping into solution (dissolution) and eventually lead to inadequate bioavailability. However this is not always the case when the nature of the solvent is considered. Understanding the solubility of a chemical compound in solvents is a key requirement for the development of a crystallization process. Water is able to solvate molecules and ions through dipole interactions, particularly hydrogen bonding allowing the compound to dissolve, e.g. although NaCl has strong ionic bonds within its crystal lattice it completely dissolves in water. This can be rationalized on the basis of solvent polarity and the maxim like dissolves like (a non-polar compound will be dissolved by a non-polar solvent and *vice versa*). In addition, the solubility of Ibuprofen is high in organic solvents such as ethanol, ethyl acetate and toluene and low in water and acetonitrile. Accordingly, methodologies which involve the modifications of crystal structure have been used to enhance solubility and increase dissolution rates.²²⁻²⁵

1.2.1. Salt Formation

For ionizable drugs, salt formation is the simplest and most cost-effective strategy to circumvent poor aqueous solubility and enhance bioavailability.²⁶⁻²⁹ About half of all the drug substances are administered as salts.³⁰ Just like the formation of a basic salt, a drug compound, classified as a weak acid or a weak base, can be combined with a suitable base or acid, respectively, to form a pharmaceutical salt. The aqueous solubility of an acidic or basic drug as a function of pH controls whether the compound will form suitable salts or not. By varying the pH, the pH-solubility profile of an acidic/basic drug can be illustrated by two curves (see Figure 1.2), one where the saturation or equilibrium species is the free acid/base and the other where the salt is the equilibrium species.³¹ The point where the curves

intersect is called the pH_{max} .² This is the point where maximum solubility is achieved and where both the free acid/base and salt coexist as solids. Interest in the formation of pharmaceutical salts has increased significantly over the years with this technique becoming relatively common in drug product development.³²

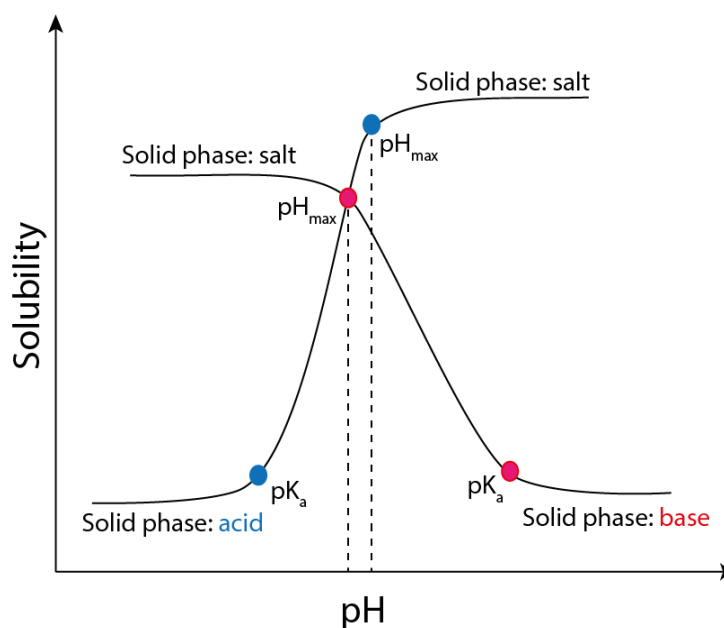


Figure 1.2. Solubility versus pH.

1.2.2. Pharmaceutical Cocrystals

Briefly, for non-ionizable drugs, an alternative method to enhance solubility is to use cocrystalization.³³⁻³⁷ A lot of drugs exist in the crystalline solid state due to better stability and ease of handling during the different stages of drug development. The term crystalline, indicates an ideal crystal in which the structural units, named unit cells, are repeated regularly and indefinitely in three dimensions in space. A simple way to describe cocrystals is that they are crystalline material comprised of at least two molecular species held together by non-covalent interactions where all components are solid under ambient conditions.^{33,38-40} Cocrystals are an important

class of pharmaceutical materials that can enhance solubility and dissolution by forming a crystal of a drug and a conformer with specific stoichiometric compositions as shown in Figure 1.3. Cocrystals have the ability to effect the strength of the crystal lattice and the solvation of cocrystal components.^{41,42} Such methodology have shown significant attention which has led to the FDA releasing guidelines regarding cocrystals in 2011.⁴³

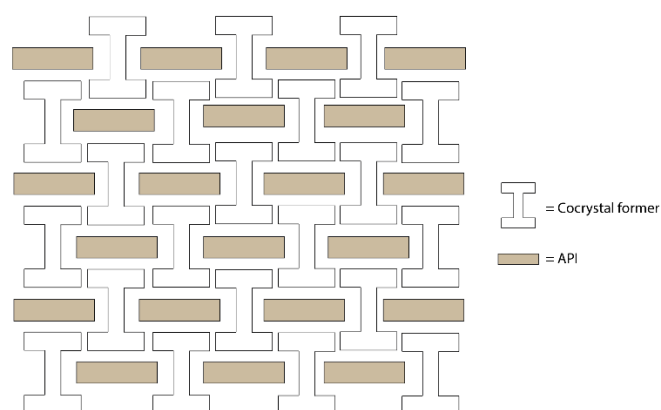


Figure 1.3. Representation of API cocrystal.

1.2.3. Nanosizing

A simpler drug delivery approach for poorly water-soluble drugs is reducing the API particle size to the submicron range.^{44,45} Commonly, a method that is referred to as micronization/nanosizing, the final particle size having a mean diameter of $< 1 \mu\text{m}$.⁴⁶ One of the earliest application of pharmaceutical nanotechnology was on danazol, an API that belong to class II drugs of BCS.⁴⁷ Danazol milled to a median particle size of 169 nm has resulted in enhanced oral bioavailability as compared to the regular drug. The essence of this approach is primarily the increase in surface area. When the particle size is reduced, the larger surface area of the API allows the increase in the surface area to volume ratio thus increasing the surface area available for solvation.

Consequently, it provides rapid dissolution without altering the chemical nature of the API. As shown by Noyes-Whitney model of dissolution (discussed *vide infra*) the surface area of the solid drug is directly proportional to its rate of dissolution. Several studies have been done and are reported to confirm this.⁴⁸⁻⁵⁰ Nanoparticles of poorly water soluble APIs can be produced by various technologies, which can be broadly categorized into bottom-up and the top down technologies.⁵¹ In bottom-up technologies controlled crystallization is achieved by dissolving the API molecule in a solvent, subsequently this solution is added to a non-solvent solution forming a supersaturated solution. Through rapid nucleation, the formation of small nuclei are obtained. Top-down technologies include high-pressure homogenization (in which the API is dispersed in solution and is forced under pressure through a nanosized aperture valve of a high pressure homogenizer) and milling methods.^{51,52} Such techniques provide more efficient size reduction.⁵³ Nanoparticle technology has become a well-established and well tested approach for poorly-soluble drugs.⁵⁴

1.2.4. Polymorphism

Another method to improve solubility is to use a particular polymorphic form of drug molecules.⁵⁵⁻⁵⁷ Crystalline polymorphs have the same chemical composition but different internal crystal structure, including unit cell dimensions and crystal packing which can affect pharmaceutical performance.^{58,59} At any given combination of temperature, pressure and humidity, one of the crystal forms will have the lowest energy and thus be the preferred form with the most stable crystal lattice arrangement (Figure 1.4 shows a cartoon illustration). Any given two polymorphs can be either monotropic or enantiotropic. If one crystal form is more stable regardless of temperature, then the system is monotropic, Figure 1.5 (i). However, a system where one form is stable at higher temperatures and another form in lower temperatures is referred to enantiotropic system. Below the melting point, the transition temperature at which the free energy between two polymorphs is equal. Thus, one form is stable

above the transition temperature, and other form is stable below the transition temperature, Figure 1.5 (ii).

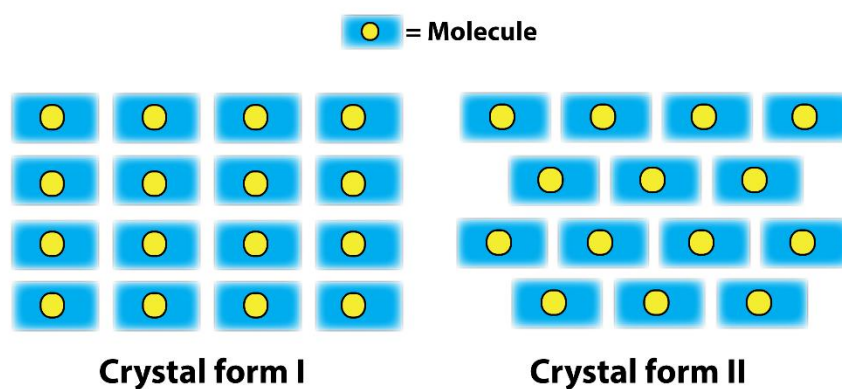


Figure 1.4. Representation of structural polymorphism.

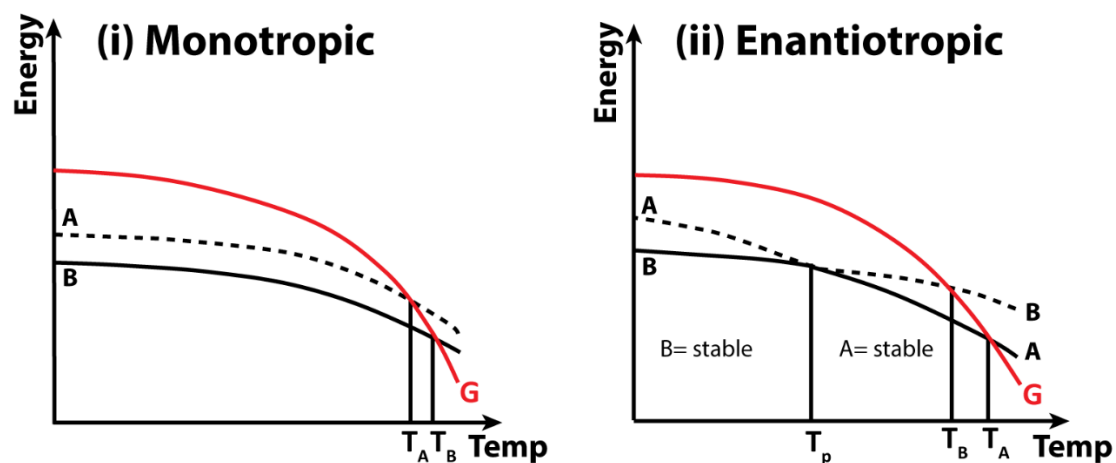


Figure 1.5. Energy versus temperature diagram of (i) monotropic system and (ii) enantiotropic where T_p is the transition temperature.

However, a system in an unstable state does not necessarily transform directly into the most thermodynamically stable state, thus indicating the presence of metastable intermediate states, as described by Ostwald in 1897.⁶⁰ According to Ostwald, in general, the least stable polymorph crystallizes first followed by the transformation to the next most stable solid state until the most stable state with the minimum energy is achieved, see Figure 1.6. Hitherto, many have highlighted that growing crystals in nanoscale containers restrict their size and alignment which can influence the final crystal structure.⁶¹⁻⁶⁶ The concept of crystallization at the nanoscale will be brought to attention in chapter 5.

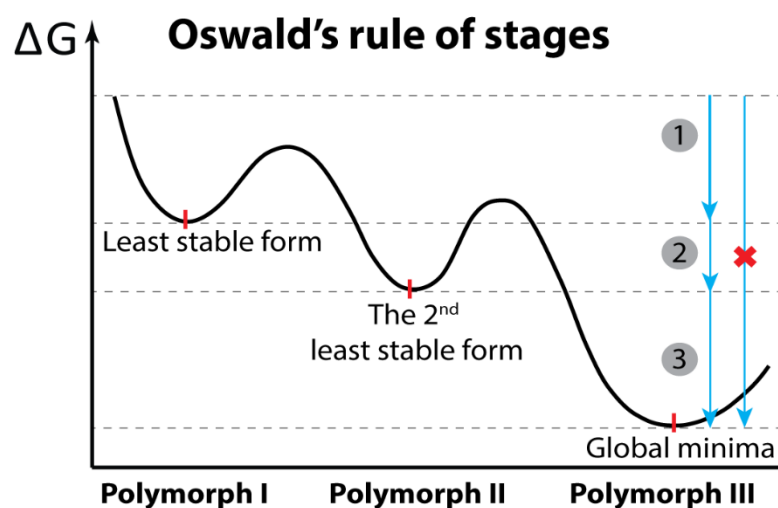


Figure 1.6. Energy states of polymorphs explaining Ostwald's rule of stages.

Many pharmaceutical drugs, despite their physical nature (i.e. being neutral, free acids, free bases or pharmaceutical salts), are capable of exhibiting polymorphism. Although some may have none, others may have multiple polymorphs. The most thermodynamically stable (highest density and melting point) polymorph, despite

having lower aqueous solubility, is most likely to be chosen for drug formulations to avoid any phase transitions. The first recognized example of polymorphism in a molecular crystal was benzamide, observed by Friedrich Wöhler and Justus von Liebig in 1832.⁶⁷ Early pioneering reports of Aguiar *et al*^{56,57} have emphasized the impact of drug polymorphism on bioavailability, which numerous studies and reviews followed.⁶⁸⁻⁷³ A notable case of polymorphism is perhaps ritonavir, an antiretroviral medication used along with other medications to treat HIV.⁷⁴ The initially developed form of ritonavir was found to convert to a more stable and less soluble polymorph resulting in a reduction in its bioavailability. The ability to control polymorphism has proved difficult, due to limited understanding of nucleation pathways (*vide infra*) and the absence of methods that can study crystallization at its earliest stages.

1.2.5. Amorphous Solid Dispersion

Following on, another approach shown to enhance bioavailability of APIs is to formulate solid dispersions.^{75,76} The term solid dispersion can be described as a group of solid products consisting of at least two different components. This brings us to the discussion of amorphous solid dispersions (ASDs) as an alternative way to use the metastable form of the API to increase the extent and rate of dissolution.^{25,77,78} It is well established that the metastable forms of drug substances enhance solubility over their thermodynamic stable counterparts.^{71,79,80} In ASD formulations, the API is in a metastable form, it being in an amorphous state. Here, the metastable amorphous API is mixed with a suitable water soluble polymer forming a molecular dispersion as shown in Figure 1.7. The polymer carrier improves the API's solid-state physical stability reducing its molecular mobility by increasing the glass transition temperature of the mixture.⁸¹ Additionally, it helps to stabilize the amorphous solid form during storage and manufacture processes. Existing in an amorphous form results in a more extensive and faster dissolution as it lacks the long-range crystalline order and has lower packing efficiency. Thus, drug molecules do not have to overcome the crystal

lattice energy for it to dissolve. To maintain the amorphous state of the solid, the polymer interacts with the molecules of the API by attractive forces of hydrogen bonding.^{77,82} This also results in an increase in surface area of the API to increase the rate of dissolution (as described by Noyes-Whitney theory, discussed in section 1.4). In addition, due to the polymer's large surface area it can inhibit crystallization, delay or prevent nucleation and growth of crystals during dissolution. Commonly used polymers such as hydroxypropyl methylcellulose (HPMC), Hydroxypropyl cellulose (HPC) and Polyvinylpyrrolidone (PVP) are biologically inert and regarded safe which is beneficial for reach purposes. As highlighted polymer carriers are crucial in the formulation of ASD, and thus the understanding of polymer-API interaction is necessary. Elucidating polymer interaction with amorphous solids in aqueous medium is a complex process which is studied by many⁸³⁻⁹⁰ and is further explored in chapter 4.

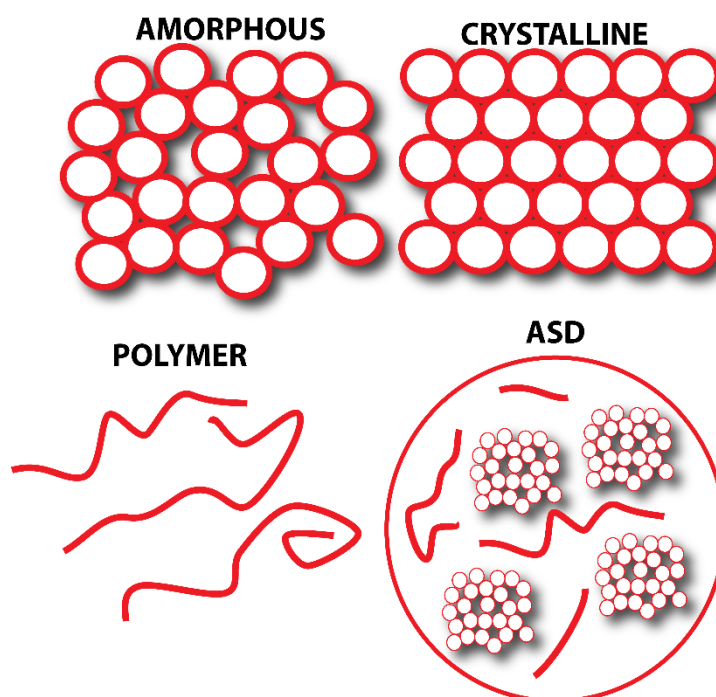


Figure 1.7. Representation of the composition of ASD.

1.3. Nucleation and Growth of Crystals

A traditional model for the early stages of crystallization is described by two processes.^{91,92} First being nucleation for the formation of stable atomic/molecular clusters and secondly the subsequent growth of the nuclei that form spontaneously out of a supersaturated solution or undercooled melt (i.e. below its freezing point).⁹³ In solution crystallization, nucleation plays a critical role in determining the crystal structure (hence polymorphism) and size distribution. Thus, fundamental understanding of nucleation is of high demand to achieve control over these properties.

Firstly, in order for nucleation and growth of a crystal to occur, the concept of supersaturation needs to be addressed. Supersaturation is the driving force required for the nucleation process to proceed and it is defined as the difference in chemical potential between a molecule in solution and that in the bulk of the crystal phase, equation 1:

$$\Delta\mu = \mu_s - \mu_c \quad (1)$$

where μ_s is the chemical potential of a molecule in solution and μ_c is the chemical potential of the molecule in the bulk crystal.

In thermodynamic terms, the driving force can be expressed as shown in equation 2:

$$\Delta\mu = k_B T \ln S \quad (2)$$

where k_B is the Boltzmann constant, T is the absolute temperature, and S is the supersaturation ratio (solution concentration / equilibrium concentration).

Nucleation can either be classed as homogeneous or heterogeneous, collectively known as primary nucleation.^{94,95} The spontaneous formation and subsequent growth of new particles in the bulk supersaturated solution in the absence of foreign particles is a homogenous process. In contrast, heterogeneous nucleation occurs in the presence of foreign materials (e.g. particle or a surface layer), due to the complexity behavior of the real world, most nucleation process are in fact heterogeneous. Nucleation consists of a series of processes in which the atoms/molecules of a reactant phase rearrange into a cluster of the product phase. This formed cluster is defined as nucleus, i.e. minimum amount of a new phase capable of independent existence that can grow to a macroscopically larger size.

Importantly, another feature of nucleation is the required passage over a free energy barrier for transformation to occur.⁹⁶ This can be easily understood when the free energy changes associated with the formation of the nucleus are considered. According to nucleation theory, the amount of energy required to form a nucleus is the difference between the free energy of the system in its final and initial states as well as a term related to the formation of an interface between nucleus and solution. Assuming a spherical nucleus (as shown in Figure 1.8 (a)) this statement can be expressed by equation 3:

$$\Delta G = \underbrace{-\frac{4}{3}\pi \cdot \frac{r^3}{V} \Delta\mu}_{\Delta G_V} + \underbrace{4\pi \cdot r^2 \gamma}_{\Delta G_S} \quad (3)$$

where V is the molecular volume, r is the radius of the cluster, and γ is the interfacial free energy between the solid and liquid phases

This thermodynamic description was developed by Gibbs at the end of the 19th century.⁹⁷ The free energy change required for cluster formation (ΔG) is the total free energy change for the phase transformation (ΔG_V) and the free energy change for the

formation of a surface (ΔG_S), represented in Figure 1.8 (b). Overall, the spontaneous growth of clusters depends on the competitive interplay between a decrease in ΔG_V (which favors growth) and an increase in ΔG_S (which favors dissolution). At small radii, the positive surface free energy (ΔG_S) is dominating, resulting in an initial increase in the total free energy of the system. Thus, the smallest clusters in solution typically dissolve. As the size of clusters increases; the total free energy goes through a maximum at an intermediate size, known as the critical size (r^*), highlighted in Figure 1.8 (b). Above the critical size the total free energy decreases continuously making the growth step energetically favorable and resulting in the formation of crystal nuclei. This phenomenon is referred to as the Gibbs-Thomson effect.⁹⁸

The significance of the critical size concept is that it determines the probability of a nucleus formation at any given timescale, i.e. determining the kinetics of the nucleation. The rate of nucleation (J), which is the number of nuclei formed per unit time per unit volume is expressed by an Arrhenius form shown in equation 4:

$$J = A \exp\left(-\frac{\Delta G_{critical}}{kT}\right) \quad (4)$$

where A is the pre-exponential factor and depends on the supersaturation, k is the Boltzmann's constant and T is the temperature.

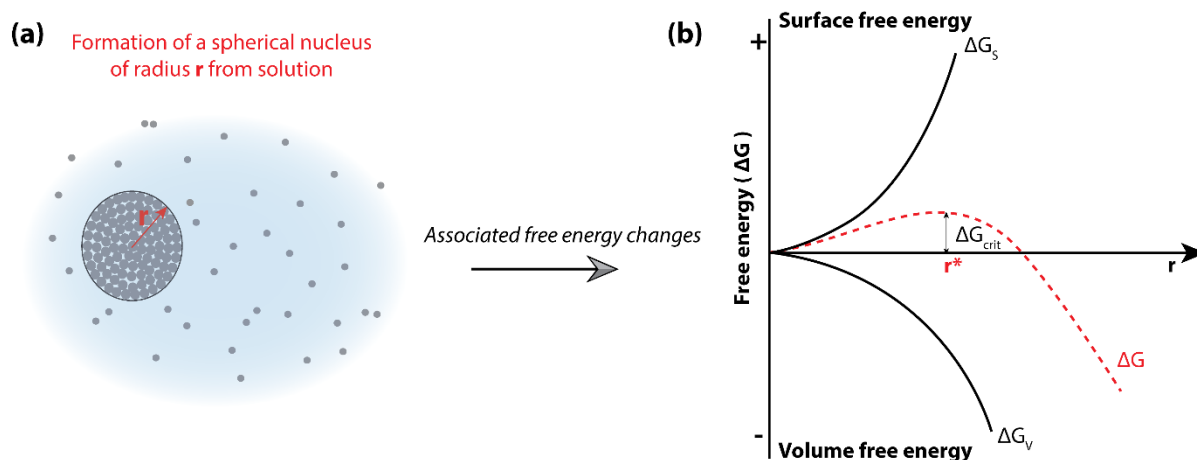


Figure 1.8. (a) Formation of a spherical nucleus of radius r . (b) Total free energy as a function of the radius r of the cluster.

If nucleation occurs quickly, many crystals will form nearly simultaneously. The growth of such amount of crystals depletes solute from medium which may lead to the termination of the nucleation process at later stages of crystallization. As a result, majority of the crystals grow to similar sizes. On the other hand, if nucleation takes place slowly (i.e. fewer crystals nucleating at a time), the overall supersaturation of the solution decreases slowly, and so, nucleation of new crystals proceed, resulting in crystals of various sizes.⁹⁹

Overall, there has been significant interest in the understanding of crystal nucleation mechanisms in solution. Accordingly many advances followed such as the two-step mechanism in protein crystallization. Briefly, as the name suggests, two energy barriers must be overcome which consist of first the formation of a dense liquid followed by the nucleation of crystals within this dense liquid. Beside proteins, two-step nucleation has shown to be applicable in other systems, including organic molecules and colloids.^{99,100}

1.4. Crystal Growth/Dissolution Reactions

Understanding the fundamental factors which influence crystal dissolution can provide an insight into the dissolution behavior of drug crystals both *in vitro* and *in vivo*. As considerably, understanding the mechanisms that take place during the initial crystallization of pharmaceutical products are vital. Accordingly, the fundamental understanding of both processes can assist in enhancement of drug development and future formulation.

Crystal dissolution is a process driven by the local undersaturation at the crystal/solution interface. The dissolution of a solid in fluid occurs in a series of steps (see Figure 1.9) which include:

1. Detachment of species from a dissolution site,
2. Surface diffusion of the detached species,
3. Desorption (and adsorption),
4. Mass transport away from the crystal i.e. movement of species into the bulk solution.

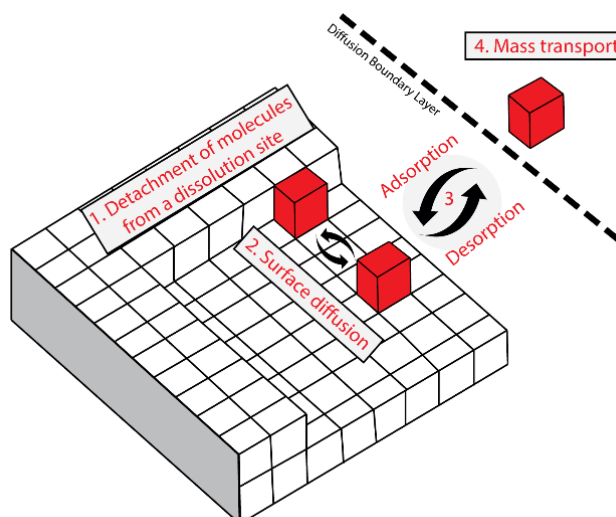


Figure 1.9. Schematic of the elementary steps involved in dissolution processes

For simplicity, these processes are often encapsulated by the two terms: (A) *surface reactions* and (B) *mass transport* in which (A) consist of steps 1-3 and (B) involves step 4. The slowest of these (A or B) control the overall dissolution reaction rate. A reaction process in which the rate of arrival of species to the bulk solution from the solid surface is slow is referred to as diffusion or mass transport limited. Hence, in this case, equilibrium solubility is rapidly achieved at the surface. Whereas, if the transport rate of species away from the crystal surface is fast, the rate becomes dependent on surface processes. This is characterized as surface or kinetic limited reaction process. Here, the drug concentration near the surface is less than its solubility concentration. A third scenario that can be observed is when both steps (A) and (B) are occurring at comparable rates. Therefore, neither the interfacial step nor diffusion are dissolution rate limiting. Figure 1.10, shows concentration profiles under different dissolution modes. The mass transport-limited dissolution model was developed from early studies done by Noyes and Whitney in 1897.^{101,102}

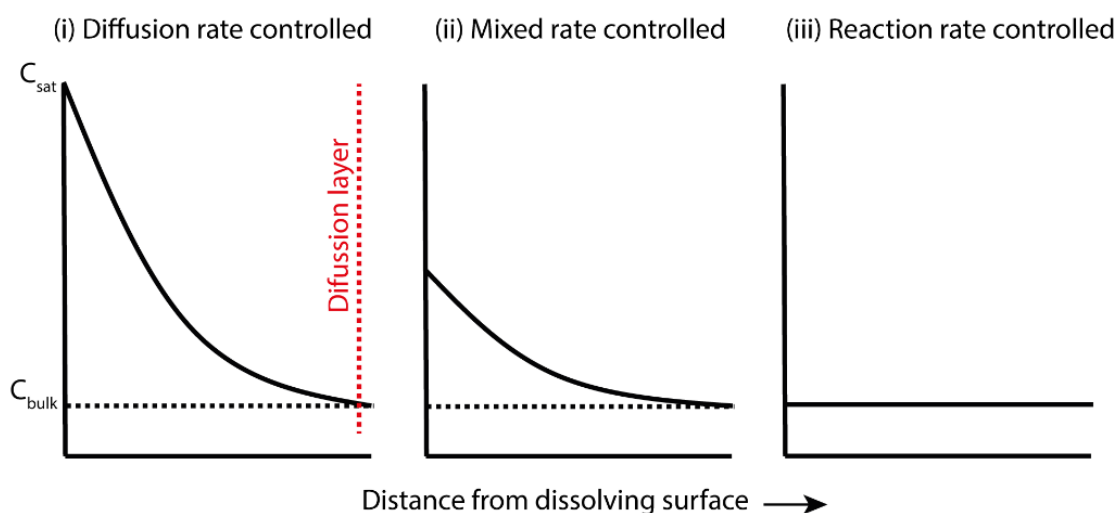


Figure 1.10. Concentration profiles under different dissolution modes: (i) diffusion rate controlled; (ii) mixed rate control and (iii) reaction rate controlled dissolution.

Noyes and Whitney conducted the first dissolution experiments and stated that the dissolution rate of a solid is a linear function of the difference between its solubility and its bulk concentration, represented in equation 5:

$$\frac{dc}{dt} = k(C_s - C_t) \quad (5)$$

where c is the amount dissolved as a function of time (t), k is a system dependent constant; C_s is the solubility of the substance and C_t is the concentration of dissolved substance in bulk solution at time t .

Although, Noyes and Whitney theory was seminal it failed to elucidate the physical meaning of the constant k . Thus, later on in 1904, Nernst and Brunner conducted further experiments to confirm the Noyes-Whitney equation and quantified the constant k .^{103,104} They introduced the concept of a stationary diffusion layer across which the solute diffuses from the solid surface to the bulk solution forming a linear concentration profile as illustrated in Figure 1.10 (i). They noted that k was proportional to the diffusion coefficient of the solid within the diffusion layer and the surface area of the dissolving body. Thus, equation 1 was rewritten and named the Nernst-Brunner equation 6:

$$\frac{dc}{dt} = \frac{SD}{\delta} (C_s - c_t) \quad (6)$$

where S is the surface area, D is the diffusion coefficient and δ represents the thickness of the diffusion layer.

Noyes and Whitney assumed that crystal growth was the reverse of dissolution, and that the rates of both processes were governed by the difference between concentration at the solid surface and in the bulk of the solution. If both growth and dissolution processes were purely diffusion controlled in nature; the rate of growth should equal

the rate of dissolution at a given temperature. In addition, all faces of a crystal would grow and dissolve at the same rate. However, these conditions are rarely achieved.¹⁰⁵

The dissolution of a solid crystal is further complicated when the nature of the crystal is considered in detail. Crystal surfaces consist of a number of features and much of the theoretical work on surface controlled reactions is based on the concept that surfaces are energetically heterogeneous.^{106,107} Kossel developed one of the earliest models in the 1930s which represented the crystal surface as cubic units containing layers of monoatomic height limited by steps/edges.^{105,108-112} Each step may comprise one or more kink along its length. Further, a terrace is referred to the area between steps and may contain vacancies or adsorbed growth units as shown in Figure 1.11. Dissolution starts, preferentially, at sites on the crystal surface which have excess free energy as it results in a reduction in the activation energy for dissolution such as dislocations, kinks, edges and ledges.^{105,108-112} Thus, one could assume that a crystal with higher dislocation density should have a higher thermodynamic activity and may result in a greater overall dissolution rate when the process is under surface control. Chapter 3 will further cover this concept as well as the necessity to determine the relative contribution of mass transport and surface reactions to understand the overall dissolution kinetics.

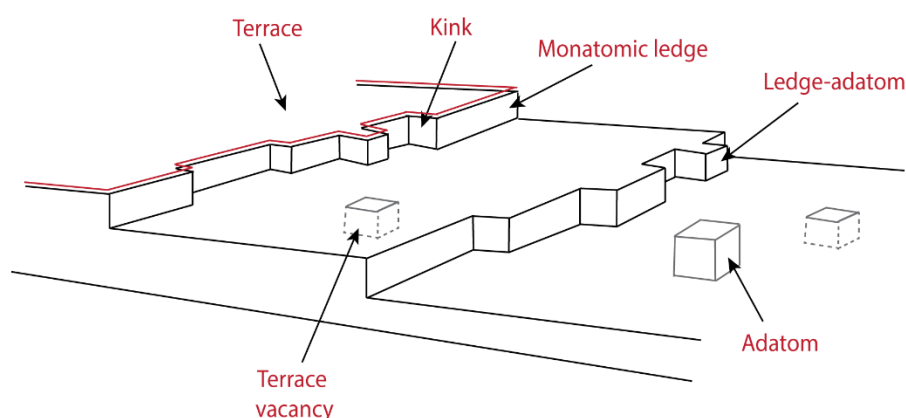


Figure 1.11. Kossel model of a crystal surface.

A transport-controlled reaction is rate limited by transport of the dissolving species through the diffusion layer. The concentration gradient across the diffusion layer can be altered by changing the mass transport rate. An innovative way to obtain fast and well defined mass transport rates is to use single isolated microcrystals.¹¹³⁻¹¹⁵ “Micro-crystal” is a term used to describe a crystal with dimensions on the micron scale and it is a concept which is derived from the field of electrochemistry and ultramicroelectrodes (UMEs) (discussed later on in section 1.6.2). If the crystal is much larger than this, the diffusion across the surface will be largely planar resulting in low and rather ill-defined diffusion rates (in stationary solution) seen in Figure 1.12 (a). For micro-crystals, diffusion of species from all direction is possible, i.e. quasi-hemispherical that allows fast and well-defined diffusion rates (Figure 1.12 (b)).

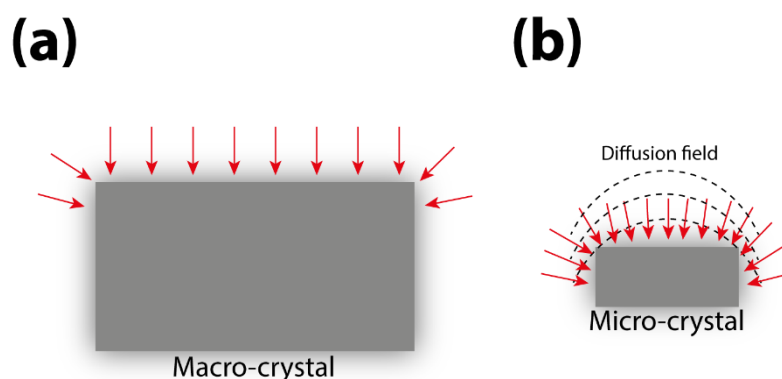


Figure 1.12. (a) Macrocrystal showing predominantly planar diffusion and (b) microcrystal showing predominantly hemispherical diffusion. Diagrams not to scale.

1.5. Traditional Dissolution Testing

In pharmaceutical drug development process, IDRs can provide key information about the API with respect to constant media pH, temperature, and surface area.¹¹⁶ According to the United States Pharmacopeia (USP) critique on dissolution, the required

apparatus includes a vessel filled with an aqueous solution that is held at 37 °C and stirred at a constant rate.¹¹⁷⁻¹¹⁹ There are seven apparatuses in the USP general chapter <711>.¹²⁰ The main two used for dissolution testing of solid oral dosage forms are Apparatus I (Basket) and Apparatus II (Paddle), shown in Figure 1.13.

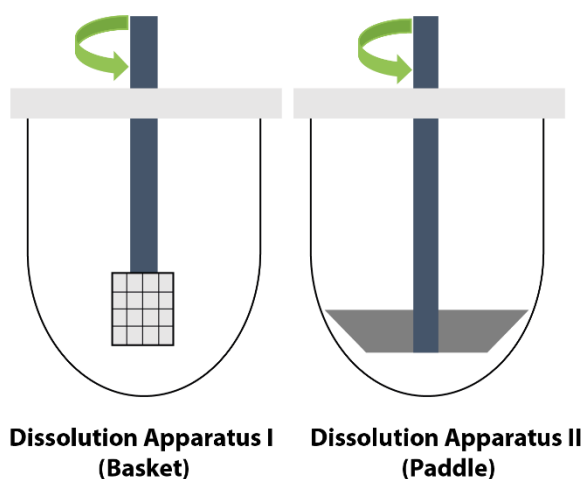


Figure 1.13. Illustration of dissolution Apparatus I (Basket) and II (Paddle).

For apparatus I, the dosage form is placed in a basket fixed to the end of a spindle. Agitation is then introduced to the system by commonly rotating the basket at 100 rpm¹²¹. Apparatus II uses a paddle typically rotated at 50-70 rpm to achieve agitation.¹²¹ For any selected apparatus a complementary analytical method is used to monitor the amount of drug released. The most common measurement methodology is UV-based, requiring minimal sample preparation.¹²² A drawback with single wavelength UV measurements is that it is difficult to gain information about the role of excipients such as the filler present within tablets. On top of that, there is the possibility of assay interference by excipients that adsorb in the same wavelength region or by undissolved excipients that could scatter light and skew the overall results.^{117,123,124} Such traditional dissolution testing are based exclusively on bulk solution concentration measurements as a function of time. Accumulation of solution concentration is needed. Thus, the lack of simultaneous real-time information about the solution concentration and the solid-state composition makes the detection of solid-

state changes during dissolution difficult. This has motivated the developments of other approaches to improve the understanding of pharmaceutical tablets including UV imaging,¹²⁵ FTIR spectroscopic imaging,¹²⁶ Raman spectroscopy and NMR.^{123,127} There is a desire for more sensitive and powerful methods to aid our understanding of drug behavior and/or drug formulations. Thus, the subsequent chapters of this thesis focus on the use of a range of scanning probe microscopy (SPM) techniques to probe dissolution and growth of pharmaceutical products.

1.6. Scanning Probe Microscopies (SPMs)

SPMs are a collective group of microscopes which branch from the scanning tunneling microscope (STM) that was first developed in 1981 by Gerd Binnig and Heinrich Rohrer.¹²⁸ Its development earned them the Nobel Prize in physics in 1986. The most common factor in all SPMs is that they rely on a fine probe tip to sense and track a sample surface proving a very high-resolution image in three dimensions, potentially to the sub-nanometer range depending on the technique and the quality of the probe tip.

1.6.1. Atomic Force Microscopy

Of the SPMs, atomic force microscopy (AFM) is the most widely used in the field of drug delivery.^{129,130} The AFM was first introduced in 1986 by Binnig and Rohrer as a new imaging methodology to obtain high resolution topographical images.¹³¹ It was created to circumvent the limitation of STM of which is the requirement of samples to be at least to some extent electrically conductive. Additionally, with AFM the ability to work under a range of environments is possible including in air and liquid over a range of temperatures.¹³²⁻¹⁴¹ This in particular is beneficial for pharmaceutical studies, an example case will be studied in chapter 3.

The fundamental understanding of the crystal morphology and surface chemistry of the crystal faces is crucial for the development of materials with specified chemical and physical characteristics. In view of that, Swift *et al.* used *in situ* AFM imaging to

study the dissolution of the (001) surface of cholesterol monohydrate single crystals in aqueous solutions.¹⁴² This has revealed different dissolution rates of the (001) and mechanisms that depend on the local surface topography. Additionally, Danesh *et al.* studied the dissolution of aspirin on the (001) and (100) faces.¹⁴³ By monitoring step velocities, dissolution rates were obtained under acidic conditions.

Tracking the early stages of crystallization is vital in understanding the overall mechanism and is strongly influenced by the crystallization conditions. Ward *et al.* carried out real time *in situ* AFM studies of the crystal growth of (melamine).(cyanuric acid) (M-CA) cocrystals in aqueous solution.¹⁴⁴ The low solubility of such system is directly associated with its formation in the kidney causing renal failure in humans and animals. Crystal growth modes on specific crystal faces were revealed in addition to an important role for hydrophobic interactions between M-CA sheets in growth.¹⁴⁴ This can lead to the design of protocols for the prevention or treatment of renal disease caused by M-CA. Another example of the influence of growth conditions is the study of the crystallization mechanism of the pharmaceutical product Irbesartan, used to treat high blood pressure.¹⁴⁵ Herein, the kinetic factors, such as temperature, supersaturation, and additives have shown to have an important role on the growth mechanism.

In AFM, a sharp tip made of silicon or silicon nitride, which is typically between 1-20 nm radius of curvature, is mounted on a 100-400 μm long flexible cantilever. The probe scans the surface in a raster motion (*x and y-plane*) and brought into and out of contact (*z-plane*) with the surface using a piezo-crystal. A laser beam is reflected from the back of the cantilever on to a segmented photodetector. There are different modes available for AFM imaging. The three principle modes will be considered here. Firstly, *contact mode* is when the tip is brought into and remains in contact with the surface at all times. It experiences a small force (of the order of nanoNewtons) as a result of interaction with the surface atoms. With contact force mode, a feedback loop is used to keep the deflection of the cantilever constant. As the cantilever is deflected, the *z*-height is altered to allow a return to the original deflection, “set point”. Due to its ease

of use, contact mode is preferably used to image hard and flat surfaces.¹⁴⁶ However, for softer surfaces, the development of so called *tapping mode* followed. Here, the tip is not always in contact with the surface, minimizing surface damage. The cantilever is chosen to oscillate at a value near its natural resonant vibration frequency (to be insensitive to vibrations and acoustic noise from surroundings). As the cantilever oscillates, the tip makes repulsive contact with the surface at the lowest point of the oscillation. Surface topography is obtained by a feedback mechanism which alters the z-height and keeps the oscillation amplitude constant. Thirdly, in *non-contact* imaging the tip is not in contact with the sample surface and is again oscillated in air but at smaller amplitude than in tapping mode. The interaction between the tip and surface are long range, van der Waals and electrostatic forces. This causes a detectable shift in frequency of the cantilever which is used in the feedback loop for the adjustment of z-position, Figure 1.14 illustrates the basics of an AFM.

Ultimately, AFM has been at the forefront of crystal studies but its relatively slow time resolution has limited this approach to systems with slow reaction kinetics, or has imposed careful selection of the solvent to further slowdown the kinetics. Nevertheless, AFM provided fundamental information about drug systems including, crystalline properties¹⁴⁷⁻¹⁵⁰, characterisation of pharmaceutical drugs¹⁵¹ and excipient¹⁵²⁻¹⁵⁴ and dissolution/growth^{139,155,156} kinetics of a range of systems.

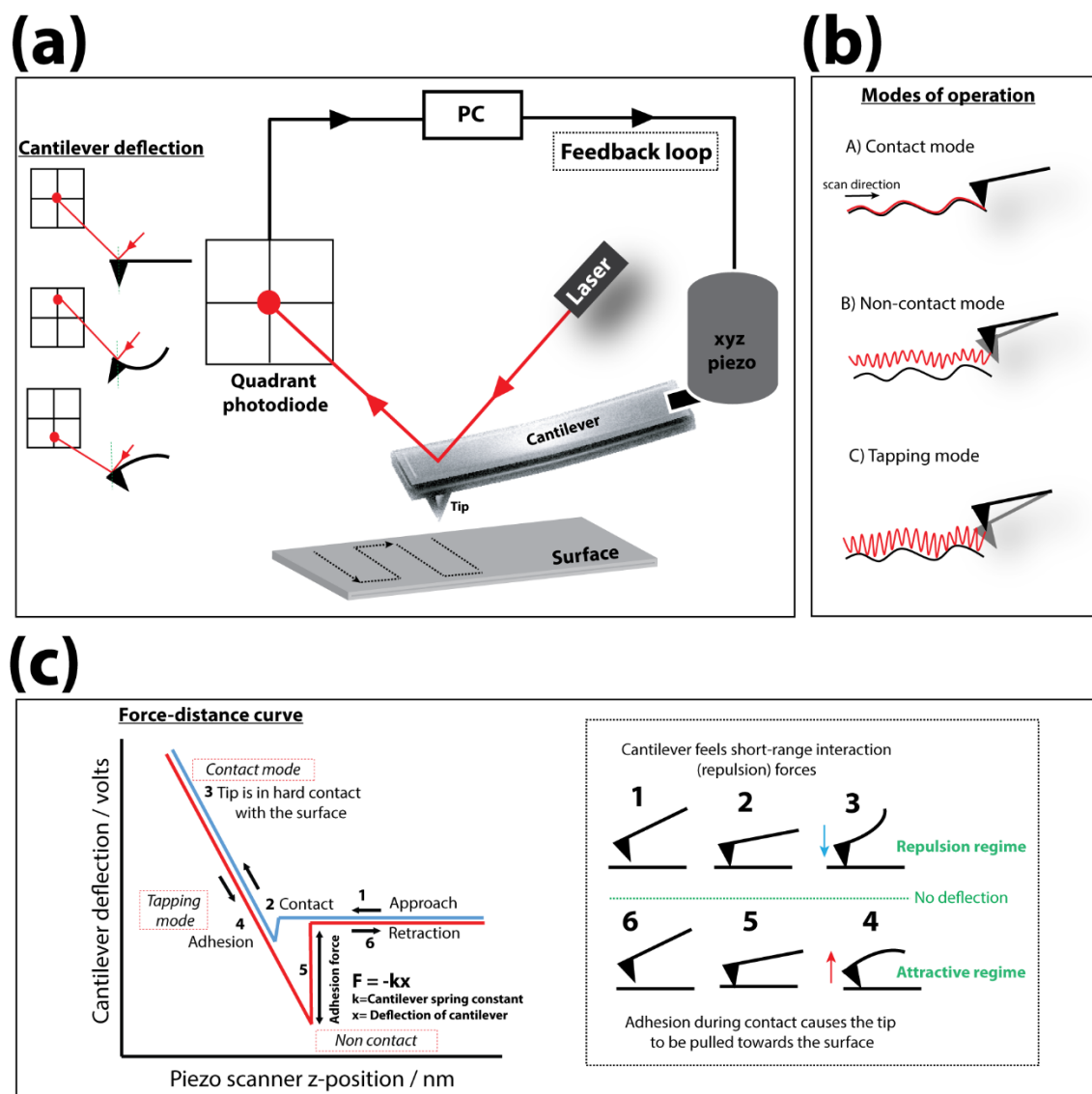


Figure 1.14. (a) Schematic of the key features of an AFM, (b) different modes of AFM and (c) shows the force-distance curve.

1.6.2. Scanning Electrochemical Microscopy

Another powerful SPM technique for quantitative investigation of processes that occur at interfaces is the scanning electrochemical microscope (SECM) in which first studies

were performed in 1989 by Bard *et al.*,¹⁵⁷ following earlier work from Engstrom in 1986.¹⁵⁸ SECM uses a UME tip to probe surface properties (such as topography and activity) by measuring the current caused from an electrochemical reaction occurring at the UME surface, as shown in Figure 1.15.¹⁵⁹ In a typical SECM experiment, both the tip and sample substrate are immersed in an electrolyte solution containing electroactive species. If a potential is applied to the UME and scans laterally across the surface, changes in the current as a function of distance between the UME tip and substrate can be recorded constructing a topographical map of the surface. SECM is typically performed in a constant-height mode where the tip is scanned across the surface at a fixed height. Though, considering surface topographical changes and any sample tilt, scanning at constant height can lead to either, the tip losing the surface or tip crash during scan. SECM can alternatively be operated in constant-current mode where the tip tracks the surface maintaining a constant tip-substrate distance throughout the scan and recording the change in tip-substrate separation. Here, a feedback loop is used to adjust the tip position and provide a constant current. A drawback of this feedback mechanism is that it is affected by substrate activity and topography.¹⁵⁹ Another mode of operation is the collective mode, which can either be: tip generation/substrate collection (TG/SC) or substrate generation/tip collection (SG/TC).¹⁵⁹ In TG/SC, the UME is positioned near the surface and is held at a certain potential to detect electroactive species produced at the substrate. Conversely, in SG/TG, a potential is instead applied to the substrate, and current is measured at the UME. The use of collection mode SECM to study the dissolution of ionic crystals has been well implemented (*vide infra*).

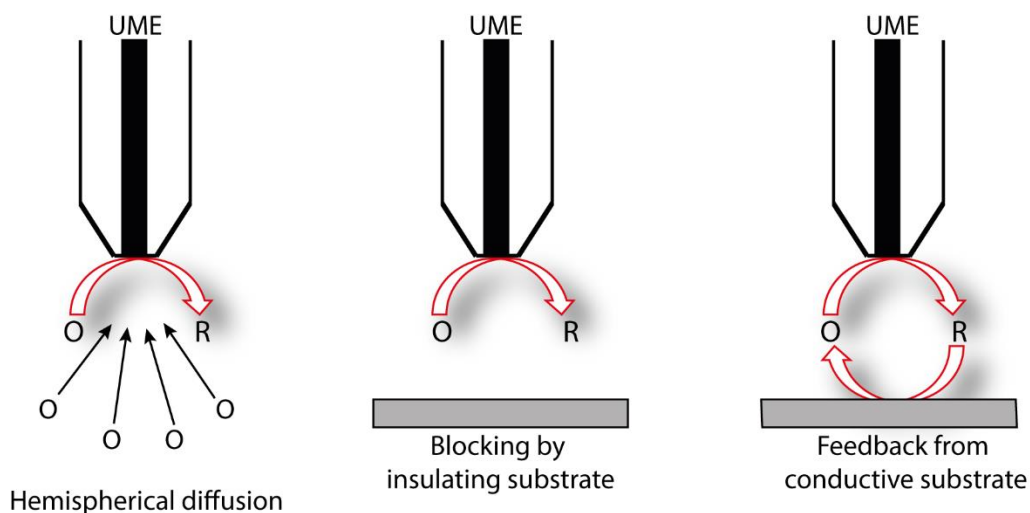


Figure 1.15. Schematic of the principles of SECM showing hemispherical diffusion of the tip far away from the substrate surface, blocking of diffusion by insulating substrate and positive feedback at a conductive substrate.

As highlighted above, with SECM, one can probe several properties of a chosen surface. One application is to probe concentration boundary layer of a crystal.¹⁶⁰ The resulting flux from the crystal surface is transduced into a faradaic current collected at the UME. Ultimately, this may provide quantitative information about the rate and nature of the reaction. Using a UME as a working electrode has benefits: it provides high diffusion rates and small overall currents which allows studies under steady-state conditions.¹⁵⁹ In addition, the achievement of small currents at the UME enables electrochemical measurements to be carried out in low conductance media such as organic solvents.^{161,162} The UME can also be used to induce and observe dissolution from a specific region of a crystal surface. This has been well-documented for the dissolution of ionic crystals.^{160,163-165} Having a saturated solution with respect to the solid crystal, by controlling the potential at the UME, the electrolysis of one or more types of the lattice ions in the solution can be initiated at a diffusion controlled rate. This results in the diffusion of dissolved ions from the crystal surface to be detected at

the UME producing a current flow. The magnitude of this observed current depends on the rate and mechanism of the dissolution reaction.

1.6.3. Scanning Ion-conductance Microscopy

The scanning ion-conductance microscope (SICM) was introduced by Hansma., around a similar time to SECM.¹⁶⁶ Mainly used for topographical imaging. SICM uses a simple single barrel micro/nanopipette for probing an interface that is bathed in a conducting electrolyte solution. In a typical set-up, the pipette is filled with an electrolyte solution and a quasi-reference counter electrode (QRCE) is inserted and a second QRCE is placed in the bulk electrolyte solution. A voltage bias is then applied between the two QRCEs to initiate and drive ionic current through the end of the pipette, as shown in Figure 1.16.

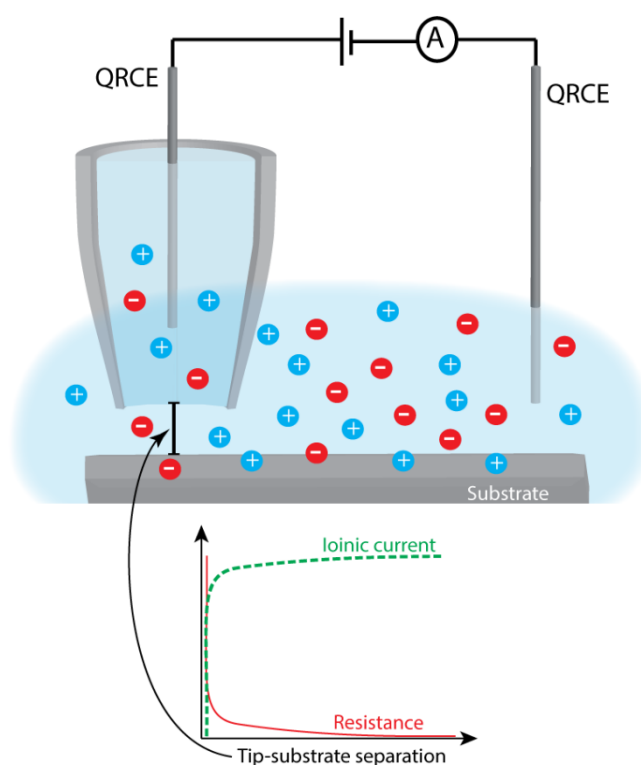


Figure 1.16. Schematic of SICM set-up.

The magnitude of the current that follows is determined by the resistance of the pipette and that of the electrolyte solution, when the tip probe is positioned far away from the substrate. Conventionally, as the tip moves towards the surface of interest, the ionic current decreases, most greatly seen when the probe-substrate distance is less than one tip diameter.¹⁶⁷ This decrease in current response can be used as a sensor to track surface topography as the tip is moved across the substrate.

SICM can be operated in different modes. In constant-distance mode, the position of the nanopipette is altered by a feedback loop mechanism in which piezo electric positioners maintain a constant current value that correspond to a constant probe-substrate distance. It is typically scanned over the surface in a raster pattern. Alternatively, hopping mode can be implemented whereby, once the set point current value is achieved, as the tip approaches the surface (*z-plane*), the tip is retracted and moved across (*x-y plane*) to a new location before repeating the same approach. This scan hopping regime is particularly beneficial for probing samples with large height gradients that constant distance mode may not be able to track.¹⁶⁷ The use of the ionic current as a means of feedback for topographical imaging is known as direct current (DC) feedback.

Modulation techniques proved particularly powerful to avoid drift effects in DC current by the generation of an alternating current (AC) signal between the QRCEs. This is typically attained by oscillating the nanopipette normal to the surface at a set frequency (100 Hz-1000 Hz range) and a lock-in amplifier is then used to collect the ionic current at the same frequency, this is labelled as distance modulated (DM)-SICM. More recently, an alternative modulation technique known as bias modulation (BM)-SICM has been developed by the Warwick group.¹⁶⁸ Here, the AC signal is generated by modulating the bias between the QRCEs with a small amplitude. This approach has several advantages over DM-SICM, as, it allows the detection of surfaces when there is no net bias applied, overcoming concerns related to the use of strong bias for topographical mapping of cells due to intense electric field at the end of the tip.

SICM has developed over the years with these modulation techniques allowing more robust imaging capabilities. Major advances of SICM have led to its application in studying crystal dissolution in combination with other microscopy techniques for a complete reaction overview.¹⁶⁹⁻¹⁷¹ Examples include crystal dissolution studies of the organic molecule Furosemide¹⁷² and kidney stones of L-cystine,¹³⁶ in which BM-SICM was used for tracking the changes in crystal height in aqueous media over time, subsequently, determining the dissolution rate of that face. Monitoring crystal height changes with BM-SICM minimizes the perturbations of the local ionic atmosphere. Additionally, it opens up the possibility of fast reaction mapping of surfaces.¹⁷³

1.6.4. Scanning Electrochemical Cell Microscopy

There have been many developments in electrochemical SPMs to further their capabilities, particularly to create so called multi-microscopy techniques that can provide complementary parallel information about surfaces processes, such as (at least) activity and topography. The earliest simultaneous topographical and electrochemical measurement was achieved by a combined SECM-AFM approach.¹⁷⁴⁻¹⁷⁶ Other combinatorial techniques include, SECM-SICM, SICM-AFM.^{169,171} The Warwick group has introduced SECCM.^{177,178} This latter technique is used for the studies in chapter 6. The probe used in SECCM is a theta pipette (double barrel) and simultaneous measurements of the topography and local functional properties of surfaces and interfaces are achieved. The basic idea is to place two QRCEs, often being silver chloride coated silver wires (Ag/AgCl), one in each barrel of the theta glass capillary and then to apply a potential bias between the two. Each barrel is filled with the electrolyte of interest. Figure 1.17 shows the basic setup. The potential difference drives the movement of ions between the two barrels, through the meniscus at the end of the pipette (direct current, DC). With the aid of a high resolution piezo-electric positioning system the electrochemical probe is positioned perpendicularly to the surface of interest. By the application of a small amplitude oscillation, typically a small

fraction of the pipette diameter, usually being 10 %, ¹⁷⁷ when the meniscus at the end of the pipette comes into contact with the surface an alternating current (AC) component of the conductance current develops. ¹⁷⁷⁻¹⁷⁹ The AC amplitude is measured and used as a feedback parameter, ensuring constant contact between the electrochemical probe and the surface as well as maintaining a fixed sample-probe separation. AC and DC are simultaneously measured along with the electrode surface current and z-piezo position. ^{177,179}

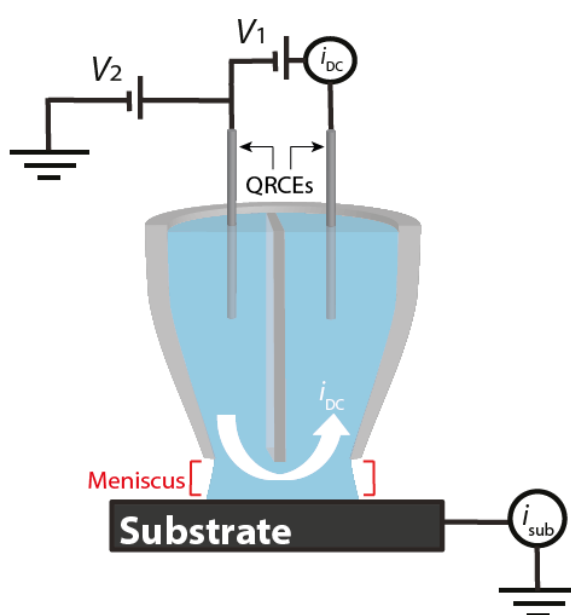


Figure 1.17. Schematic of SECCM setup. Theta pipette is used to create a tiny meniscus electrochemical cell on a substrate. The working electrode size is determined by the size of the pipette opening and meniscus wetting of the substrate.

With a similar tip probe used in SECCM (i.e. dual barrel), the dissolution kinetics of the ionic crystal (NaCl) in aqueous solution has been previously reported. ¹⁸⁰ The solution in the pipette is undersaturated with respect to the crystal, and when the meniscus at the end of the pipette makes contact with a desired region of the crystal surface, dissolution and a change in the barrel conductance current is seen and

monitored with time. Its high solubility and relatively high dissolution fluxes, makes this system particularly challenging to study with techniques that require immersion of the crystal in a bulk solution such as *in situ* AFM. With SECCM, the crystal surface is only exposed to the solution where the meniscus makes contact allowing measurements to be made with submillisecond time resolution, allowing the possibly to study many systems of various solubility.

1.7. Nanopipettes

Pipettes are proving increasingly powerful probes to investigate surface processes¹⁸¹⁻¹⁸⁵ not least because they can be prepared easily and rapidly from quartz or glass capillaries using a laser puller as illustrated in Figure 1.18 (a). Several types of nanopipette can be achieved depending on the initial capillary used that can result in a probe with a single, double or quad barrel as highlighted in Figure 1.18 (b). And by adjusting the laser puller parameters a range of orifice sizes can be obtained.^{184,186} Using nanopipettes allows the possibility of studying a wide range of processes at the early stages.^{183,187-189} This can provide unique and valuable information that can enhance the understanding of fundamental processes and help to elucidate complex reactions. Hence, chapters 4, 5 and 6 will show the use of such pipettes as an innovative approach to study the dissolution and growth of pharmaceutical drug products.

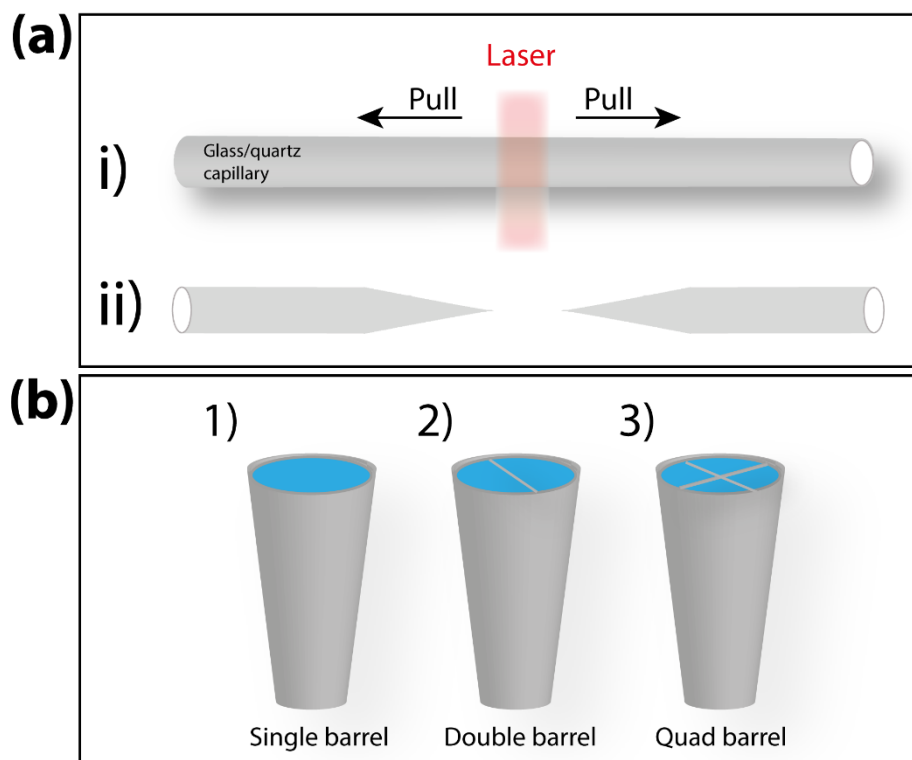


Figure 1.18. (a) Schematic mechanistic of the laser puller used to make the sharp nanopipette tips. (b) Illustration of the several types of nanopipettes that can be made with different capillaries.

1.8. Resistive Pulse Detection

Chapter 5 of this thesis will look at the use of nanopipettes as a reaction center to study crystallization of organic material at the nanoscale, though the use of Coulter counter principles. The Coulter counter, also known as a resistive-pulse counter, was first introduced in 1953 by Wallace Coulter for the analysis of micrometre-sized materials such as bacteria and cells.¹⁹⁰ Traditionally, a Coulter counter consisted of two compartments that are separated by a small opening (20 μm -2 mm). Particles in the electrolytic solution are driven through the opening by the application of a potential bias or pressure gradient. An Ag/AgCl electrode is inserted into each compartment

(either side of the opening) to continuously record ionic current changes during particle translocation. As a particle translocates through the opening, a single resistive pulse signal is generated. Analysis of the obtained pulse signal (i.e. frequency, width and height) can provide information on size, quantity and surface charge properties of the translocating particle.^{191,192} Accordingly, solid-state and biological nanopores is a field that has advanced over recent years, with pore diameters ranging to a few nanometers.¹⁹³⁻¹⁹⁹ Likewise, by applying Coulter counter principles, nanopipettes can be used as resistive pulse sensors as illustrated in Figure 1.19.

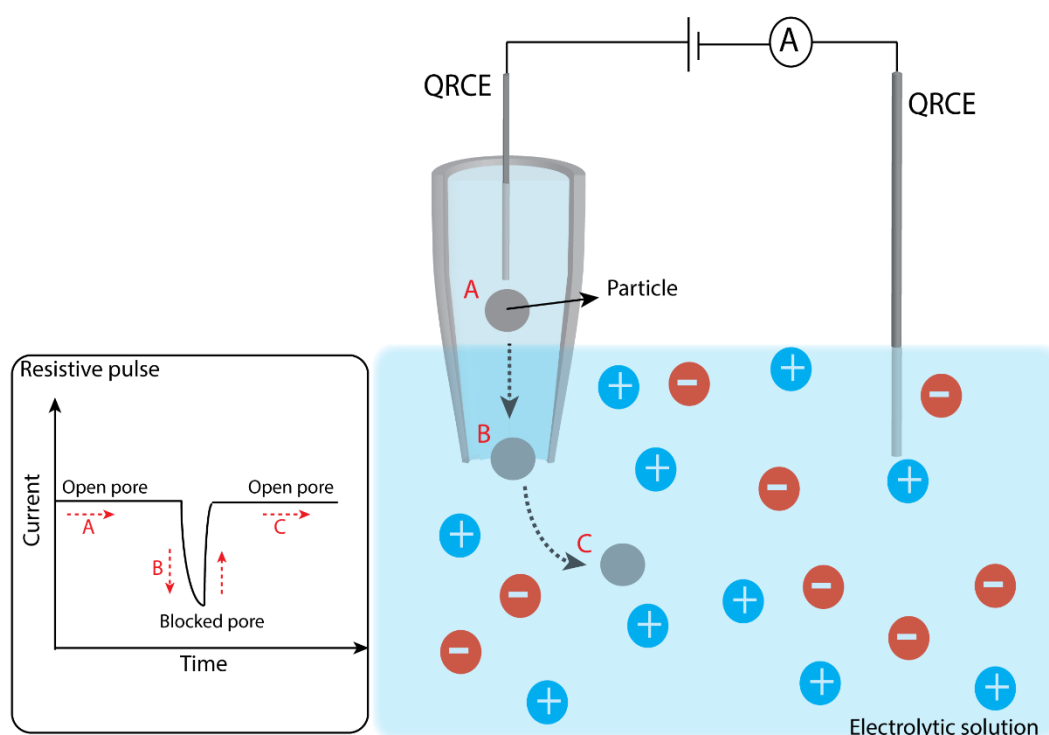


Figure 1.19. Schematic showing how nanopipettes can act as resistive pulse sensors. When a particle moves towards the pore the system feels an increase in resistance resulting in a drop in current as the particle translocates the pore.

Nanopipettes have previously been demonstrated to be powerful tools for driving the crystallization of inorganic crystals through driving the constituent ions together at the nanopipette orifice through the application of a bias.^{183,200,201} In addition, Perry *et al* reported crystallization and dissolution in real time of CaCO_3 in aqueous solution with the use of nanopipettes. By controlling the bias between a quasi-reference counter electrode in the nanopipette and one in the bulk solution the ability to mix or de-mix two different solutions by ion migration can be initiated which drive either growth or dissolution.²⁰²

1.9. Research Aims

The fundamental aims of this research are to extend the understanding of dissolution and growth processes of APIs with low aqueous solubility, with innovative approaches that use high resolution SPM techniques. Further, it is shown in the final results chapter that some of the techniques developed are applicable to other areas, as exemplified by studies of an electrode material.

Chapter 3 presents first results in this thesis. It centres on the study of the class II API bicalutamide as its low solubility/dissolution rate is a key factor limiting oral bioavailability and clinical applications. The aim here is to understand the fundamental factors which influence crystal dissolution, which could assist in enhancement of drug development and formulation. Thus, this chapter focuses on surface-selective studies under well-defined mass transport conditions. The dissolution kinetics of individual bicalutamide form-I microcrystals in aqueous solution by *in situ* AFM and finite element method (FEM) modelling is investigated. In addition, the importance of evolving high index crystal faces on the overall dissolution rates is explored. The final goal is to obtain a detailed quantitative and comprehensive view of the dissolution kinetics as well as concentration distributions of individual crystal faces.

Chapter 4 focuses on the understanding of the dissolution mechanism of ASDs in aqueous environments. The ASD of interest comprises felodipine drug in the water-soluble polymer, copovidone. Dissolution performance of felodipine/copovidone ASD is highly dependent upon drug loading and so two very different drug loadings were investigated, 15% and 50%. The aim is to highlight the importance of drug loading on the dissolution of ASDs with a combination of electrochemical probing, *in situ* AFM and Raman analysis.

Chapter 5 proposes a new method to study antisolvent crystallization at the nanoscale. As discussed above, crystallization in confined environments can have a significant impact on the properties of the emerging crystal structure. Herein, nanopipettes are used as a reaction center to study crystallization events of the API bicalutamide (class II) on the nanoscale with the aim of forming unusual polymorphs. This can be particularly exciting for pharmaceutical industries.

SECCM is described in the introductory chapter. Chapter 6, provides an example of its application in studying the electro-oxidation of reduced nicotinamide adenine dinucleotide (NADH) on highly oriented pyrolytic graphite (HOPG) and polycrystalline boron-doped diamond (pBDD). Here, an overview of the technique will be illustrated as well its capability of elucidating such complex system.

Chapter 7 finalises this thesis providing brief conclusions on the research and future perspectives.

1.10. References

- (1) Dressman, J.; Reppas, C. *Advanced Drug Delivery Reviews* **2007**, *59*, 531-532.
- (2) Wiser, L.; Gao, X.; Jasti, B.; Li, X. In *Oral Bioavailability*; John Wiley & Sons, Inc., 2011, pp 21-38.
- (3) Avdeef, A. *Absorption and drug development: solubility, permeability, and charge state*; John Wiley & Sons, 2012.
- (4) Savjani, K. T.; Gajjar, A. K.; Savjani, J. K. *ISRN Pharmaceutics* **2012**, *2012*, 195727.
- (5) Tanaka, Y.; Baba, T.; Tagawa, K.; Waki, R.; Nagata, S. *Journal of Pharmacy & Pharmaceutical Sciences* **2014**, *17*, 106-120.
- (6) Lipinski, C. A.; Lombardo, F.; Dominy, B. W.; Feeney, P. J. *Advanced Drug Delivery Reviews* **1997**, *23*, 3-25.
- (7) Lipinski, C. *American Pharmaceutical Review* **2002**, *5*, 82-85.
- (8) Siepmann, J.; Siepmann, F. *International Journal of Pharmaceutics* **2013**, *453*, 12-24.
- (9) Lipinski, C. A. *Journal of Pharmacological and Toxicological Methods* **2000**, *44*, 235-249.
- (10) Venkatesh, S.; Lipper, R. A. *Journal of Pharmaceutical Sciences*, *89*, 145-154.
- (11) Amidon, G. L.; Lennernas, H.; Shah, V. P.; Crison, J. R. *Pharmaceutical Research* **1995**, *12*, 413-420.
- (12) Alsenz, J.; Kansy, M. *Advanced Drug Delivery Reviews* **2007**, *59*, 546-567.
- (13) Amidon, G. L.; Lennernas, H.; Shah, V. P.; Crison, J. R. *Pharmaceutical Research* **1995**, *12*, 413-420.

- (14) Chavda, H.; Patel, C.; Anand, I. *Systematic Reviews in Pharmacy* **2010**, *1*, 62.
- (15) Amidon, G. E.; Higuchi, W. I.; Ho, N. F. *Journal of Pharmaceutical Sciences* **1982**, *71*, 77-84.
- (16) Yu, L. X.; Carlin, A. S.; Amidon, G. L.; Hussain, A. S. *International Journal of Pharmaceutics* **2004**, *270*, 221-227.
- (17) Dahlan, R.; McDonald, C.; Sunderland, V. B. *Journal of Pharmacy and Pharmacology* **1987**, *39*, 246-251.
- (18) Zakeri-Milani, P.; Barzegar-Jalali, M.; Azimi, M.; Valizadeh, H. *European Journal of Pharmaceutics and Biopharmaceutics* **2009**, *73*, 102-106.
- (19) Jinno, J.; Oh, D.; Crison, J. R.; Amidon, G. L. *Journal of Pharmaceutical Sciences* **2000**, *89*, 268-274.
- (20) Di, L.; Fish, P. V.; Mano, T. *Drug Discovery Today* **2012**, *17*, 486-495.
- (21) O'Donnell, K. P.; Williams, R. O. In *Formulating Poorly Water Soluble Drugs*, Williams Iii, R. O.; Watts, A. B.; Miller, D. A., Eds.; Springer New York: New York, NY, 2012, pp 27-93.
- (22) Blagden, N.; De Matas, M.; Gavan, P.; York, P. *Advanced Drug Delivery Reviews* **2007**, *59*, 617-630.
- (23) Savjani, K. T.; Gajjar, A. K.; Savjani, J. K. *ISRN Pharmaceutics* **2012**, *2012*.
- (24) Cisneros, J. A.; Robertson, M. J.; Mercado, B. Q.; Jorgensen, W. L. *ACS Medicinal Chemistry Letters* **2017**, *8*, 124-127.
- (25) Dhirendra, K.; Lewis, S.; Udupa, N.; Atin, K. *Pakistan Journal of Pharmaceutical Sciences* **2009**, *22*.
- (26) Serajuddin, A. T. M. *Advanced Drug Delivery Reviews* **2007**, *59*, 603-616.

- (27) Avdeef, A. *Advanced Drug Delivery Reviews* **2007**, *59*, 568-590.
- (28) Berge, S. M.; Bighley, L. D.; Monkhouse, D. C. *Journal of Pharmaceutical Sciences* **1977**, *66*, 1-19.
- (29) Gould, P. L. *International Journal of Pharmaceutics* **1986**, *33*, 201-217.
- (30) Stahl, P. H.; Wermuth, C. G. *Chemistry International* **2002**, *24*, 21.
- (31) Kramer, S. F.; Flynn, G. L. *Journal of Pharmaceutical Sciences* **1972**, *61*, 1896-1904.
- (32) Grifasi, F.; Chierotti, M. R.; Gaglioti, K.; Gobetto, R.; Maini, L.; Braga, D.; Dichiarante, E.; Curzi, M. *Crystal Growth & Design* **2015**, *15*, 1939-1948.
- (33) Korotkova, E. I.; Kratochvíl, B. *Procedia Chemistry* **2014**, *10*, 473-476.
- (34) Cao, F.; Amidon, G. L.; Rodriguez-Hornedo, N.; Amidon, G. E. *Molecular Pharmaceutics* **2016**, *13*, 1030-1046.
- (35) Serrano, D. R.; O'Connell, P.; Paluch, K. J.; Walsh, D.; Healy, A. M. *Journal of Pharmacy and Pharmacology* **2016**, *68*, 665-677.
- (36) Shayanfar, A.; Asadpour-Zeynali, K.; Jouyban, A. *Journal of Molecular Liquids* **2013**, *187*, 171-176.
- (37) Elder, D. P.; Holm, R.; Diego, H. L. d. *International Journal of Pharmaceutics* **2013**, *453*, 88-100.
- (38) Aakery, C. B.; Salmon, D. J. *CrystEngComm* **2005**, *7*, 439-448.
- (39) Bhogala, B. R.; Nangia, A. *New Journal of Chemistry* **2008**, *32*, 800-807.
- (40) Trask, A. V.; Motherwell, W. S.; Jones, W. *Crystal Growth & Design* **2005**, *5*, 1013-1021.

- (41) Good, D. J.; Rodríguez-Hornedo, N. *Crystal Growth & Design* **2009**, *9*, 2252-2264.
- (42) Kobayashi, Y.; Ito, S.; Itai, S.; Yamamoto, K. *International Journal of Pharmaceutics* **2000**, *193*, 137-146.
- (43) Aitipamula, S.; Banerjee, R.; Bansal, A. K.; Biradha, K.; Cheney, M. L.; Choudhury, A. R.; Desiraju, G. R.; Dikundwar, A. G.; Dubey, R.; Duggirala, N.; Ghogale, P. P.; Ghosh, S.; Goswami, P. K.; Goud, N. R.; Jetti, R. R. K. R.; Karpinski, P.; Kaushik, P.; Kumar, D.; Kumar, V.; Moulton, B.; Mukherjee, A.; Mukherjee, G.; Myerson, A. S.; Puri, V.; Ramanan, A.; Rajamannar, T.; Reddy, C. M.; Rodriguez-Hornedo, N.; Rogers, R. D.; Row, T. N. G.; Sanphui, P.; Shan, N.; Shete, G.; Singh, A.; Sun, C. C.; Swift, J. A.; Thaimattam, R.; Thakur, T. S.; Kumar Thaper, R.; Thomas, S. P.; Tothadi, S.; Vangala, V. R.; Variankaval, N.; Vishweshwar, P.; Weyna, D. R.; Zaworotko, M. J. *Crystal Growth & Design* **2012**, *12*, 2147-2152.
- (44) Kesisoglou, F.; Panmai, S.; Wu, Y. *Advanced Drug Delivery Reviews* **2007**, *59*, 631-644.
- (45) Merisko-Liversidge, E.; Liversidge, G. G.; Cooper, E. R. *European Journal of Pharmaceutical Sciences* **2003**, *18*, 113-120.
- (46) Dizaj, S. M.; Vazifehasl, Z.; Salatin, S.; Adibkia, K.; Javadzadeh, Y. *Research in Pharmaceutical Sciences* **2015**, *10*, 95-108.
- (47) Liversidge, G. G.; Cundy, K. C. *International Journal of Pharmaceutics* **1995**, *125*, 91-97.
- (48) Chu, K. R.; Lee, E.; Jeong, S. H.; Park, E.-S. *Archives of Pharmacal Research* **2012**, *35*, 1187-1195.
- (49) Wu, Y.; Loper, A.; Landis, E.; Hettrick, L.; Novak, L.; Lynn, K.; Chen, C.; Thompson, K.; Higgins, R.; Batra, U.; Shelukar, S.; Kwei, G.; Storey, D. *International Journal of Pharmaceutics* **2004**, *285*, 135-146.

- (50) Müller, R. H.; Peters, K. *International Journal of Pharmaceutics* **1998**, *160*, 229-237.
- (51) Khadka, P.; Ro, J.; Kim, H.; Kim, I.; Kim, J. T.; Kim, H.; Cho, J. M.; Yun, G.; Lee, J. *Asian Journal of Pharmaceutical Sciences* **2014**, *9*, 304-316.
- (52) Merisko-Liversidge, E. M.; Liversidge, G. G. *Toxicologic Pathology* **2008**, *36*, 43-48.
- (53) Williams, H. D.; Trevaskis, N. L.; Charman, S. A.; Shanker, R. M.; Charman, W. N.; Pouton, C. W.; Porter, C. J. H. *Pharmacological Reviews* **2013**, *65*, 315-499.
- (54) Kalepu, S.; Nekkanti, V. *Acta Pharmaceutica Sinica B* **2015**, *5*, 442-453.
- (55) Higuchi, W. I.; Bernardo, P. D.; Mehta, S. C. *Journal of Pharmaceutical Sciences*, *56*, 200-207.
- (56) Aguiar, A. J.; Krc, J., Jr.; Kinkel, A. W.; Samyn, J. C. *Journal of Pharmaceutical Sciences* **1967**, *56*, 847-853.
- (57) Aguiar, A. J.; Zelmer, J. E. *Journal of Pharmaceutical Sciences* **1969**, *58*, 983-987.
- (58) Morissette, S. L.; Almarsson, Ö.; Peterson, M. L.; Remenar, J. F.; Read, M. J.; Lemmo, A. V.; Ellis, S.; Cima, M. J.; Gardner, C. R. *Advanced Drug Delivery Reviews* **2004**, *56*, 275-300.
- (59) Raza, K.; Kumar, P.; Ratan, S.; Malik, R.; Arora, S. *Polymorphism: The Phenomenon Affecting the Performance of Drugs* **2014**.
- (60) Ostwald, W. *Zeitschrift für Physikalische Chemie* **1897**, *22*, 289-330.
- (61) Navrotsky, A. *Chemphyschem* **2011**, *12*, 2207-2215.
- (62) Navrotsky, A.; Mazeina, L.; Majzlan, J. *Science* **2008**, *319*, 1635-1638.

- (63) Jiang, Q.; Ward, M. D. *Chemical Society Reviews* **2014**, *43*, 2066-2079.
- (64) Hamilton, B. D.; Ha, J.-M.; Hillmyer, M. A.; Ward, M. D. *Accounts of Chemical Research* **2012**, *45*, 414-423.
- (65) Ha, J.-M.; Wolf, J. H.; Hillmyer, M. A.; Ward, M. D. *Journal of the American Chemical Society* **2004**, *126*, 3382-3383.
- (66) Lee, A. Y.; Lee, I. S.; Dette, S. S.; Boerner, J.; Myerson, A. S. *Journal of the American Chemical Society* **2005**, *127*, 14982-14983.
- (67) Wöhler, F. *Annalen der Physik* **1856**, *173*, 484-488.
- (68) Brittain, H. G. *Polymorphism in pharmaceutical solids*; CRC Press, 2009.
- (69) Hilfiker, R. *Polymorphism: in the pharmaceutical industry*; John Wiley & Sons, 2006.
- (70) Lee, E. H. *Asian Journal of Pharmaceutical Sciences* **2014**, *9*, 163-175.
- (71) Pudipeddi, M.; Serajuddin, A. T. M. *Journal of Pharmaceutical Sciences* **2005**, *94*, 929-939.
- (72) Snider, D. A.; Addicks, W.; Owens, W. *Advanced Drug Delivery Reviews* **2004**, *56*, 391-395.
- (73) Vippagunta, S. R.; Brittain, H. G.; Grant, D. J. W. *Advanced Drug Delivery Reviews* **2001**, *48*, 3-26.
- (74) Bauer, J.; Spanton, S.; Henry, R.; Quick, J.; Dziki, W.; Porter, W.; Morris, J. *Pharmaceutical Research* **2001**, *18*, 859-866.
- (75) Chiou, W. L.; Riegelman, S. *Journal of Pharmaceutical Sciences* **1971**, *60*, 1281-1302.
- (76) Sharma, A.; Jain, C. P. *International Journal of Drug Delivery* **2011**, *3*, 22.

- (77) Janssens, S.; Van den Mooter, G. *Journal of Pharmacy and Pharmacology* **2009**, *61*, 1571-1586.
- (78) Newman, A. *Pharmaceutical amorphous solid dispersions*; John Wiley & Sons, 2015.
- (79) Huang, L. F.; Tong, W. Q. *Advanced Drug Delivery Reviews* **2004**, *56*, 321-334.
- (80) MAO, L.; ZHENG, Q.-t.; LU, Y. *Natural Product Research and Development* **2005**, *3*, 031.
- (81) Vasconcelos, T.; Sarmiento, B.; Costa, P. *Drug Discovery Today* **2007**, *12*, 1068-1075.
- (82) Gunawan, L.; Johari, G. P.; Shanker, R. M. *Pharmaceutical Research* **2006**, *23*, 967-979.
- (83) Qian, F.; Huang, J.; Hussain, M. A. *Journal of Pharmaceutical Sciences* **2010**, *99*, 2941-2947.
- (84) Konno, H.; Handa, T.; Alonzo, D. E.; Taylor, L. S. *European Journal of Pharmaceutics and Biopharmaceutics* **2008**, *70*, 493-499.
- (85) Sun, Y.; Zhu, L.; Wu, T.; Cai, T.; Gunn, E. M.; Yu, L. *The AAPS journal* **2012**, *14*, 380-388.
- (86) Marsac, P. J.; Konno, H.; Taylor, L. S. *Pharmaceutical Research* **2006**, *23*, 2306-2316.
- (87) Marsac, P. J.; Li, T.; Taylor, L. S. *Pharmaceutical Research* **2009**, *26*, 139.
- (88) Six, K.; Verreck, G.; Peeters, J.; Brewster, M.; Mooter, G. V. d. *Journal of Pharmaceutical Sciences* **2004**, *93*, 124-131.
- (89) Rumondor, A. C.; Stanford, L. A.; Taylor, L. S. *Pharmaceutical Research* **2009**, *26*, 2599.

- (90) Yang, J.; Grey, K.; Doney, J. *International Journal of Pharmaceutics* **2010**, 384, 24-31.
- (91) Oxtoby, D. W. *Journal of Physics: Condensed Matter* **1992**, 4, 7627.
- (92) Oxtoby, D. W. *Accounts of Chemical Research* **1998**, 31, 91.
- (93) Wedekind, J.; Xu, L.; Buldyrev, S. V.; Stanley, H. E.; Reguera, D.; Franzese, G. *Scientific Reports* **2015**, 5, 11260.
- (94) Chaikin, P. M.; Lubensky, T. C. *Principles of Condensed Matter Physics*; Cambridge University Press, 2000.
- (95) Hohenberg, P. C.; Halperin, B. I. *Reviews of Modern Physics* **1977**, 49, 435-479.
- (96) Kashchiev, D. *Nucleation*; Butterworth-Heinemann, 2000.
- (97) Gibbs, J. W. *American Journal of Science* **1878**, Series 3 Vol. 16, 441-458.
- (98) De Yoreo, J. J.; Vekilov, P. G. *Reviews in Mineralogy and Geochemistry* **2003**, 54, 57-93.
- (99) Vekilov, P. G. *Crystal Growth & Design* **2010**, 10, 5007-5019.
- (100) Erdemir, D.; Lee, A. Y.; Myerson, A. S. *Accounts of Chemical Research* **2009**, 42, 621-629.
- (101) Noyes, A. A.; Whitney, W. R. *Journal of the American Chemical Society* **1897**, 19, 930-934.
- (102) Dokoumetzidis, A.; Macheras, P. *International Journal of Pharmaceutics* **2006**, 321, 1-11.
- (103) Brunner, E. *Physical Chemistry* **1904**, 47, 56.
- (104) Nernst, W. *Zeit. physikal. Chem* **1904**, 47, 52-55.

- (105) Mullin, J. W. *Crystallization*; Butterworth-Heinemann, 1993.
- (106) MacInnis, I. N.; Brantley, S. L. *Chemical Geology* **1993**, *105*, 31-49.
- (107) MacInnis, I. N.; Brantley, S. L. *Geochimica et Cosmochimica Acta* **1992**, *56*, 1113-1126.
- (108) Schott, J.; Brantley, S.; Crerar, D.; Guy, C.; Borcsik, M.; Willaime, C. *Geochimica et Cosmochimica Acta* **1989**, *53*, 373-382.
- (109) Zhang, J.; Nancollas, G. H. *Journal of Crystal Growth* **1990**, *106*, 181-190.
- (110) Zhang, J.; Nancollas, G. H. *Journal of Colloid and Interface Science* **1998**, *200*, 131-145.
- (111) Balykov, L. N.; Kitamura, M.; Maksimov, I. L.; Nishioka, K. *Journal of Crystal Growth* **1999**, *198–199, Part 1*, 32-37.
- (112) Cuppen, H. M.; Meekes, H.; van Veenendaal, E.; van Enckevort, W. J. P.; Bennema, P.; Reedijk, M. F.; Arsic, J.; Vlieg, E. *Surface Science* **2002**, *506*, 183-195.
- (113) Perry, A. R.; Peruffo, M.; Unwin, P. R. *Crystal Growth & Design* **2013**, *13*, 614-622.
- (114) Adobes-Vidal, M.; Maddar, F. M.; Momotenko, D.; Hughes, L. P.; Wren, S. A.; Poloni, L. N.; Ward, M. D.; Unwin, P. R. *Crystal Growth & Design* **2016**, *16*, 4421-4429.
- (115) Perry, A. R.; Lazenby, R. A.; Adobes-Vidal, M.; Peruffo, M.; McKelvey, K.; Snowden, M. E.; Unwin, P. R. *CrystEngComm* **2015**, *17*, 7835-7843.
- (116) O'hara, T.; Dunne, A.; Butler, J.; Devane, J.; Group, I. C. W. *Pharmaceutical Science & Technology Today* **1998**, *1*, 214-223.
- (117) Gray, V.; Kelly, G.; Xia, M.; Butler, C.; Thomas, S.; Mayock, S. *Pharmaceutical Research* **2009**, *26*, 1289-1302.

- (118) Cohen, J. L.; Hubert, B. B.; Leeson, L. J.; Rhodes, C. T.; Robinson, J. R.; Roseman, T. J.; Shefter, E. *Pharmaceutical Research* **1990**, *7*, 983-987.
- (119) Gray, V. A.; Zheng, J. Y.; Sesi, N. N. In *Formulation and Analytical Development for Low-Dose Oral Drug Products*; John Wiley & Sons, Inc., 2008, pp 265-281.
- (120) **1995**.
- (121) Long, M.; Chen, Y.
- (122) Lu, X.; Lozano, R.; Shah, P. *Dissolution Technologies* **2003**, *10*, 6-16.
- (123) Coombes, S. R.; Hughes, L. P.; Phillips, A. R.; Wren, S. A. C. *Analytical Chemistry* **2014**, *86*, 2474-2480.
- (124) Wiberg, K. H.; Hultin, U.-K. *Analytical Chemistry* **2006**, *78*, 5076-5085.
- (125) Boetker, J. P.; Savolainen, M.; Koradia, V.; Tian, F.; Rades, T.; Müllertz, A.; Cornett, C.; Rantanen, J.; Østergaard, J. *Molecular Pharmaceutics* **2011**, *8*, 1372-1380.
- (126) Kazarian, S. G.; Wray, P. S. In *Raman, Infrared, and Near-Infrared Chemical Imaging*; John Wiley & Sons, Inc., 2010, pp 185-204.
- (127) Fyfe, C. A.; Grondey, H.; Blazek-Welsh, A. I.; Chopra, S. K.; Fahie, B. J. *Journal of Controlled Release* **2000**, *68*, 73-83.
- (128) Binnig, G.; Fuchs, H.; Gerber, C.; Rohrer, H.; Stoll, E.; Tosatti, E. *EPL (Europhysics Letters)* **1986**, *1*, 31.
- (129) Sitterberg, J.; Ozcetin, A.; Ehrhardt, C.; Bakowsky, U. *European Journal of Pharmaceutics and Biopharmaceutics* **2010**, *74*, 2-13.
- (130) Turner, Y. T. A.; Roberts, C. J.; Davies, M. C. *Advanced Drug Delivery Reviews* **2007**, *59*, 1453-1473.

- (131) Binnig, G.; Quate, C. F.; Gerber, C. *Physical Review Letters* **1986**, *56*, 930-933.
- (132) Land, T.; Malkin, A.; Kuznetsov, Y. G.; McPherson, A.; De Yoreo, J. *Physical Review Letters* **1995**, *75*, 2774.
- (133) Wasylenki, L. E.; Dove, P. M.; Wilson, D. S.; De Yoreo, J. J. *Geochimica et Cosmochimica Acta* **2005**, *69*, 3017-3027.
- (134) Land, T.; De Yoreo, J.; Lee, J. *Surface Science* **1997**, *384*, 136-155.
- (135) Masterson, V. M.; Cao, X. *International Journal of Pharmaceutics* **2008**, *362*, 163-171.
- (136) Adobes-Vidal, M.; Shtukenberg, A. G.; Ward, M. D.; Unwin, P. R. *Crystal Growth & Design* **2017**, *17*, 1766-1774.
- (137) Yamamoto, S.; Sugiyama, S.; Matsuoka, O.; Kohmura, K.; Honda, T.; Banno, Y.; Nozoye, H. *The Journal of Physical Chemistry* **1996**, *100*, 18474-18482.
- (138) Bosbach, D.; Charlet, L.; Bickmore, B.; Hochella, M. F. *American Mineralogist* **2000**, *85*, 1209-1216.
- (139) Hillner, P.; Manne, S.; Gratz, A.; Hansma, P. *Ultramicroscopy* **1992**, *42*, 1387-1393.
- (140) Shiraki, R.; Rock, P. A.; Casey, W. H. *Aquatic Geochemistry* **2000**, *6*, 87-108.
- (141) Dove, P. M.; Platt, F. M. *Chemical Geology* **1996**, *127*, 331-338.
- (142) Abandan, R. S.; Swift, J. A. *Crystal Growth & Design* **2005**, *5*, 2146-2153.
- (143) Danesh, A.; Connell, S. D.; Davies, M. C.; Roberts, C. J.; Tendler, S. J. B.; Williams, P. M.; Wilkins, M. J. *Pharmaceutical Research* **2001**, *18*, 299-303.
- (144) Musumeci, D.; Ward, M. D. *CrystEngComm* **2011**, *13*, 1067-1069.

- (145) Taulelle, P.; Astier, J. P.; Hoff, C.; Pèpe, G.; Veessler, S. *Chemical Engineering & Technology* **2006**, 29, 239-246.
- (146) Magonov, S. N.; Elings, V.; Whangbo, M. H. *Surface Science* **1997**, 375, L385-L391.
- (147) Danesh, A.; Davies, M. C.; Hinder, S. J.; Roberts, C. J.; Tendler, S. J.; Williams, P. M.; Wilkins, M. J. *Analytical Chemistry* **2000**, 72, 3419-3422.
- (148) Ward, S.; Perkins, M.; Zhang, J.; Roberts, C. J.; Madden, C. E.; Luk, S. Y.; Patel, N.; Ebbens, S. J. *Pharmaceutical Research* **2005**, 22, 1195-1202.
- (149) Mahlin, D.; Berggren, J.; Alderborn, G.; Engström, S. *Journal of Pharmaceutical Sciences* **2004**, 93, 29-37.
- (150) Shi, H. G.; Farber, L.; Michaels, J. N.; Dickey, A.; Thompson, K. C.; Shelukar, S. D.; Hurter, P. N.; Reynolds, S. D.; Kaufman, M. J. *Pharmaceutical Research* **2003**, 20, 479-484.
- (151) Price, R.; Young, P. M. *Journal of Pharmaceutical Sciences* **2004**, 93, 155-164.
- (152) Zhang, J.; Ebbens, S.; Chen, X.; Jin, Z.; Luk, S.; Madden, C.; Patel, N.; Roberts, C. J. *Pharmaceutical Research* **2006**, 23, 401-407.
- (153) Louey, M. D.; Mulvaney, P.; Stewart, P. J. *Journal of Pharmaceutical and Biomedical Analysis* **2001**, 25, 559-567.
- (154) Thompson, C.; Davies, M. C.; Roberts, C. J.; Tendler, S. J.; Wilkinson, M. J. *International Journal of Pharmaceutics* **2004**, 280, 137-150.
- (155) Li, T.; Morris, K. R.; Park, K. *The Journal of Physical Chemistry B* **2000**, 104, 2019-2032.
- (156) Danesh, A.; Connell, S. D.; Davies, M. C.; Roberts, C. J.; Tendler, S. J.; Williams, P. M.; Wilkins, M. *Pharmaceutical Research* **2001**, 18, 299-303.

- (157) Bard, A. J.; Fan, F. R. F.; Kwak, J.; Lev, O. *Analytical Chemistry* **1989**, *61*, 132-138.
- (158) Engstrom, R. C.; Weber, M.; Wunder, D. J.; Burgess, R.; Winquist, S. *Analytical Chemistry* **1986**, *58*, 844-848.
- (159) Bard, A. J.; Faulkner, L. R.; Leddy, J.; Zoski, C. G. *Electrochemical methods: fundamentals and applications*; Wiley New York, 1980; Vol. 2.
- (160) Macpherson, J. V.; Unwin, P. R. *Journal of the Chemical Society, Faraday Transactions* **1993**, *89*, 1883-1884.
- (161) Shao, Y.; Mirkin, M. V. *The Journal of Physical Chemistry B* **1998**, *102*, 9915-9921.
- (162) Barker, A. L.; Gonsalves, M.; Macpherson, J. V.; Slevin, C. J.; Unwin, P. R. *Analytica Chimica Acta* **1999**, *385*, 223-240.
- (163) Macpherson, J. V.; Unwin, P. R. *The Journal of Physical Chemistry* **1996**, *100*, 19475-19483.
- (164) Macpherson, J. V.; Unwin, P. R. *The Journal of Physical Chemistry* **1995**, *99*, 3338-3351.
- (165) Macpherson, J. V.; Unwin, P. R. *The Journal of Physical Chemistry* **1995**, *99*, 14824-14831.
- (166) Hansma, P. K.; Drake, B.; Marti, O.; Gould, S.; Prater, C. *Science* **1989**, *243*, 641.
- (167) Page, A.; Perry, D.; Unwin, P. R. In *Proc. R. Soc. A*; The Royal Society, 2017, p 20160889.
- (168) McKelvey, K.; Perry, D.; Byers, J. C.; Colburn, A. W.; Unwin, P. R. *Analytical Chemistry* **2014**, *86*, 3639-3646.

- (169) Takahashi, Y.; Shevchuk, A. I.; Novak, P.; Murakami, Y.; Shiku, H.; Korchev, Y. E.; Matsue, T. *Journal of the American Chemical Society* **2010**, *132*, 10118-10126.
- (170) Morris, C. A.; Chen, C.-C.; Baker, L. A. *Analyst* **2012**, *137*, 2933-2938.
- (171) Pellegrino, M.; Orsini, P.; Pellegrini, M.; Baschieri, P.; Dinelli, F.; Petracchi, D.; Tognoni, E.; Ascoli, C. *Neuroscience Research* **2011**, *69*, 234-240.
- (172) Adobes-Vidal, M.; Maddar, F. M.; Momotenko, D.; Hughes, L. P.; Wren, S. A. C.; Poloni, L. N.; Ward, M. D.; Unwin, P. R. *Crystal Growth & Design* **2016**, *16*, 4421-4429.
- (173) Momotenko, D.; Byers, J. C.; McKelvey, K.; Kang, M.; Unwin, P. R. *ACS Nano* **2015**, *9*, 8942-8952.
- (174) Macpherson, J. V.; Unwin, P. R. *Analytical Chemistry* **2000**, *72*, 276-285.
- (175) Kranz, C. *Analyst* **2014**, *139*, 336-352.
- (176) Macpherson, J. V.; Unwin, P. R.; Hillier, A. C.; Bard, A. J. *Journal of the American Chemical Society* **1996**, *118*, 6445-6452.
- (177) Ebejer, N.; Schnippering, M.; Colburn, A. W.; Edwards, M. A.; Unwin, P. R. *Analytical Chemistry* **2010**, *82*, 9141-9145.
- (178) Snowden, M. E.; Güell, A. G.; Lai, S. C. S.; McKelvey, K.; Ebejer, N.; O'Connell, M. A.; Colburn, A. W.; Unwin, P. R. *Analytical Chemistry* **2012**, *84*, 2483-2491.
- (179) Patel, A. N.; Collignon, M. G.; O'Connell, M. A.; Hung, W. O. Y.; McKelvey, K.; Macpherson, J. V.; Unwin, P. R. *Journal of the American Chemical Society* **2012**, *134*, 20117-20130.
- (180) Kinnear, S. L.; McKelvey, K.; Snowden, M. E.; Peruffo, M.; Colburn, A. W.; Unwin, P. R. *Langmuir* **2013**, *29*, 15565-15572.

- (181) Page, A.; Perry, D.; Young, P.; Mitchell, D.; Frenguelli, B. G.; Unwin, P. R. *Analytical Chemistry* **2016**, 88, 10854-10859.
- (182) Sa, N.; Fu, Y.; Baker, L. A. *Analytical Chemistry* **2010**, 82, 9963-9966.
- (183) Vilozy, B.; Actis, P.; Seger, R. A.; Pourmand, N. *ACS Nano* **2011**, 5, 3191-3197.
- (184) Morris, C. A.; Friedman, A. K.; Baker, L. A. *Analyst* **2010**, 135, 2190-2202.
- (185) Wang, Y.; Wang, D.; Mirkin, M. V. In *Proc. R. Soc. A*; The Royal Society, 2017, p 20160931.
- (186) Takahashi, Y.; Murakami, Y.; Nagamine, K.; Shiku, H.; Aoyagi, S.; Yasukawa, T.; Kanzaki, M.; Matsue, T. *Physical Chemistry Chemical Physics* **2010**, 12, 10012-10017.
- (187) Nadappuram, B. P.; McKelvey, K. M.; Byers, J. C.; Güell, A. G.; Colburn, A. W.; Lazenby, R. A.; Unwin, P. R. *Analytical Chemistry* **2015**, 87, 3566-3573.
- (188) Murray, R. W. *Chemical Reviews* **2008**, 108, 2688-2720.
- (189) Lan, W.-J.; Holden, D. A.; Zhang, B.; White, H. S. *Analytical Chemistry* **2011**, 83, 3840-3847.
- (190) Coulter, W.; Google Patents, 1953.
- (191) Bayley, H.; Martin, C. R. *Chemical Reviews* **2000**, 100, 2575-2594.
- (192) Luo, L.; German, S. R.; Lan, W.-J.; Holden, D. A.; Mega, T. L.; White, H. S. *Annual Review of Analytical Chemistry* **2014**, 7, 513-535.
- (193) Li, J.; Stein, D.; McMullan, C.; Branton, D. *Nature* **2001**, 412, 166.
- (194) Martin, C. R. *Science* **1994**, 1961-1966.

- (195) Ito, T.; Sun, L.; Henriquez, R. R.; Crooks, R. M. *Accounts of Chemical Research* **2004**, *37*, 937-945.
- (196) Liu, S.; Yuzvinsky, T. D.; Schmidt, H. *ACS nano* **2013**, *7*, 5621-5627.
- (197) Gao, C.; Ding, S.; Tan, Q.; Gu, L.-Q. *Analytical Chemistry* **2008**, *81*, 80-86.
- (198) Bezrukov, S. M.; Vodyanoy, I.; Parsegian, V. A. *Nature* **1994**, *370*, 279-281.
- (199) Kasianowicz, J. J.; Brandin, E.; Branton, D.; Deamer, D. W. *Proceedings of the National Academy of Sciences* **1996**, *93*, 13770-13773.
- (200) Innes, L.; Powell, M. R.; Vlassiouk, I.; Martens, C.; Siwy, Z. S. *The Journal of Physical Chemistry C* **2010**, *114*, 8126-8134.
- (201) Siwy, Z. S.; Powell, M. R.; Petrov, A.; Kalman, E.; Trautmann, C.; Eisenberg, R. S. *Nano Letters* **2006**, *6*, 1729-1734.
- (202) Perry, D.; Parker, A. S.; Page, A.; Unwin, P. R. *ChemElectroChem* **2016**, *3*, 2212-2220.

Chapter 2

Experimental

This Chapter provides a brief summary of the materials and chemicals used, experimental setup and instrumentation. More detailed additional information is provided in each chapter, specific to the work in that chapter.

2.1. Chemicals

All chemicals were used as received and all solutions were prepared with high purity water (Purite, Select HP) with a resistivity of *ca.* 18.2 MΩ cm at 25°C. Chemicals were weighed using a four decimal place analytical balance (Sartorius A2008). Table 2.1 lists all the chemicals used in this thesis.

Table 2.1. List of chemicals used in this thesis.

Chemicals	Commercial source
Potassium chloride (> 99.99%)	Sigma- Aldrich
Sodium chloride (> 99.99%)	Sigma- Aldrich
Phosphate buffer solution pH 7	Sigma- Aldrich
β-Nicotinamide adenine dinucleotide, reduced disodium salt hydrate (≥ 97%)	Sigma- Aldrich
Felodipine amorphous solid dispersion	AstraZeneca
Ethanol (≥ 99.5%)	Sigma-Aldrich
Bicalutamide	AstraZeneca
Tetrabutylammonium chloride (≥ 97.0%)	Sigma- Aldrich
Dimethyl sulfoxide (≥ 99.5%)	Fisher
Silver loaded epoxy adhesive	RS components
Alumina slurry (0.005 micron suspension)	Buehler

2.2. Carbon Electrodes

2.2.1. Highly Oriented Pyrolytic Graphite (HOPG)

Highly oriented pyrolytic graphite (HOPG), consists of stacked graphene layers of well-defined structures (basal plane and step edges), as shown in Figure 2.1.

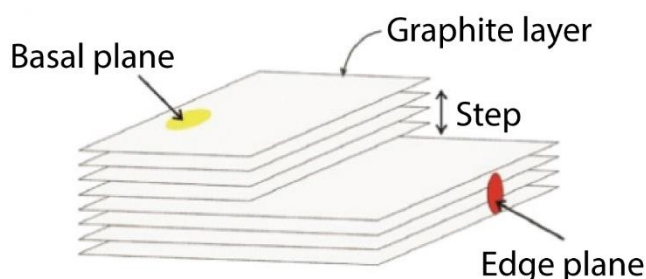


Figure 2.1. Structural illustration of HOPG.

The step edge density depends on sample preparation and treatment. Commercially available HOPG samples vary in step edge density and are graded according to their x-ray diffraction properties. In chapter 6, two different grades of commercially available HOPG were used: ZYB (NT-MDT) and SPI-3 (SPI supplies). A third HOPG sample was used which is not graded referred to AM. This originated from Arthur Moore and was kindly provided by Prof. R. L. McCreery (University of Alberta, Canada).

The HOPG samples were cleaved using Scotch tape to achieve a freshly clean surface by peeling back the top layers. The direction of cleaving was maintained the same to avoid distortion of the surface. To establish an electrical connection, the HOPG sample was mounted and adhered onto a gold sputtered silicon wafer using silver paint (RS Components). Then an external electrical contact was made by connecting a conductive wire to the wafer by the use of adhesive Glue (RS Components) and silver paint.

2.2.2. Polycrystalline Boron-Doped Diamond (pBDD)

Element six Ltd provided the pBDD samples used in chapter 6, were prepared using a commercial microwave plasma chemical vapor deposition process.¹ Before they could be used as electrodes, a few preparation steps were followed. Firstly, to establish an electrical contact the diamond samples were back sputtered with a ~20 nm layer of Ti followed by a ~400 nm layer of Au using an Edwards E306 sputter/evaporator. The samples were then left to anneal at 500 °C for 4 hours, during which titanium carbide is formed, critical for obtaining an ohmic contact. Next, the insulation of the pBDD samples was followed by sealing the diamond sample in glass capillaries (o.d. 2 mm, i.d. 1.16 mm, Harvard Apparatus Ltd, Kent, UK), using a heated filament capillary puller under vacuum. The pBDD sample was then pushed down to the sealed tip, holding a flat orientation allowing the exposure of the Ti/Au contact. Electrical contact was made to the BDD/Au surface using silver epoxy and connected to a conductive wire acting as an external electrical contact. The entire inner area of the capillary was filled with epoxy. Finally, the pBDD surface was exposed by polishing away the glass. This was done using grit paper disk grade and alumina (0.05 µm) paste (Buehler, Düsseldorf, Germany). Figure 2.2 shows a schematic diagram of a pBDD 1 mm diameter disk macro-electrode.

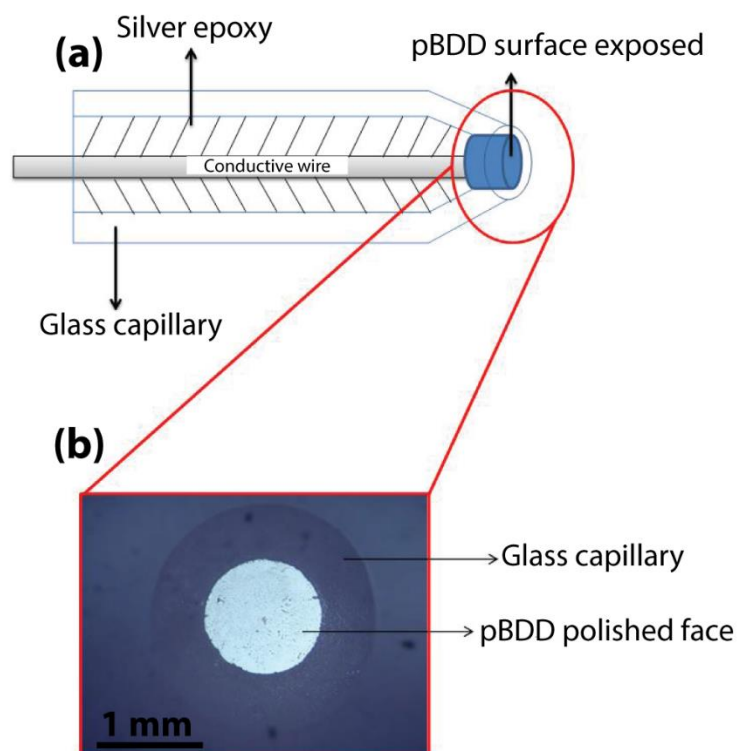


Figure 2.2. (a) Schematic diagram of the in-house fabricated pBDD electrode. (b) An optical microscope image of pBDD electrode face with a diameter of 1 mm.

2.3. Macroscale Electrochemistry

For the macroscopic voltammograms carried out on HOPG in chapter 6, all samples were mounted on gold coated (100 nm) silicon wafers by using Acheson Electrodag (Agar Scientific, 1415M). An electrical contact was made between the HOPG and silicon wafer by attaching a metal wire to the gold surface. A 3 mm in diameter Teflon cell was used to give a well-defined working area. Using piezon grease carefully applied to the cylinder end in a small amount, the cell was placed on the surface of the HOPG and filled with the solution of interest, as shown in Figure 2.3.

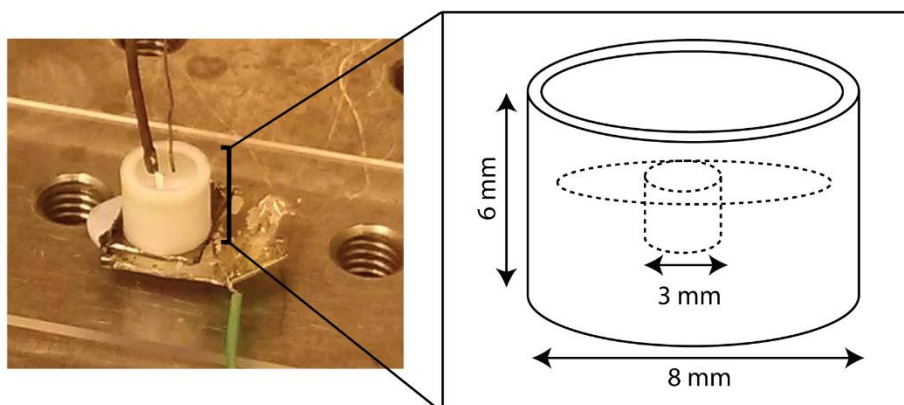


Figure 2.3. Schematic of the Teflon cell used to hold solution on HOPG with a defined contact area.

2.4. Quad-Probe Fabrication

The carbon based quad probes used in chapter 4 were fabricated from quartz quadruple-barrelled capillaries (MBT-015-062- 4Q, Friedrich and Dimmock, Inc.).² As discussed in the introduction, the capillaries were pulled to sharp point pipettes using a laser puller (p-2000, Sutter Instruments). In order to form a double barrel carbon probe for localized chemical detection and distance feedback control the following procedure was undertaken:

Two of the barrels were internally coated with carbon by making sure the remaining two barrels were closed using Blu-Tack (Bostik, UK). Carbon was deposited inside the sharp end of the pipette by the pyrolytic decomposition of butane under argon atmosphere using a gas blow torch (RS Components), as demonstrated in Figure 2.4. After carbon deposition, electrical contact was made by inserting a platinum wire through the top end of the pipette barrel to contact the carbon layer. The other two barrels were left unmodified, filled with electrolyte and were used for distance control.³⁻⁵

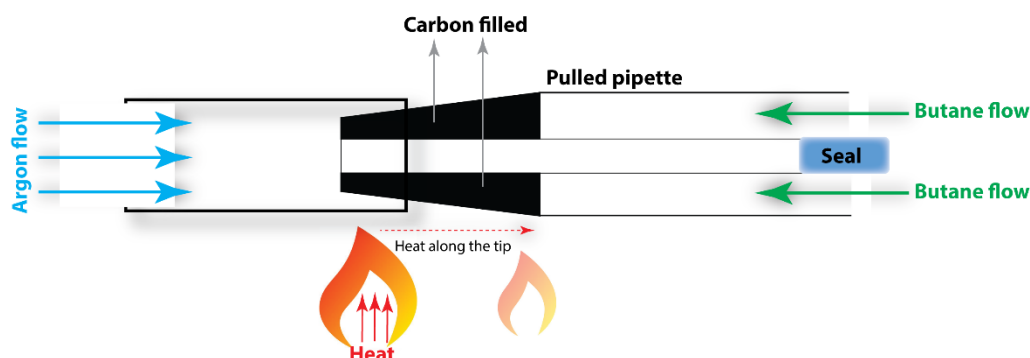


Figure 2.4. Schematic of the carbon deposition process for the fabrication of a quad-probe. Butane is passed through the pulled pipet barrels and pyrolyzed using a hand held butane torch under an argon atmosphere.

2.5. Preparation of Bicalutamide Microcrystals

For the investigation of the aqueous dissolution kinetics of bicalutamide (BIC) represented in chapter 3, optically clear crystals were used, grown following the solvent-antisolvent crystallization method.⁶ In the typical experiment, 10 mM BIC solution was made using a mixture of ethanol and dimethyl sulfoxide, DMSO in 5:1 ratio. BIC is fairly soluble in ethanol (7 mg/ml at 25 °C) and highly soluble in DMSO (86 mg/ml at 25 °C). This organic solution containing BIC was labelled as the “solvent” and the aqueous solution as the “antisolvent”. 200 µl of BIC was added to 400 µl H₂O and the growth of crystals was initiated on the plastic surface of a petri dish under closed environment. After leaving it stationary in the fluid mixture for 15 min, the surface was rinsed with water and dried using nitrogen. This method produced crystals with a largest dimension of 10-40 µm, holding a coffin like morphology as shown in Figure 2.5. Prior to any crystal analysis, the crystals were carefully inspected optically for cracks and rinsed with ultra-pure water then dried with nitrogen gas.

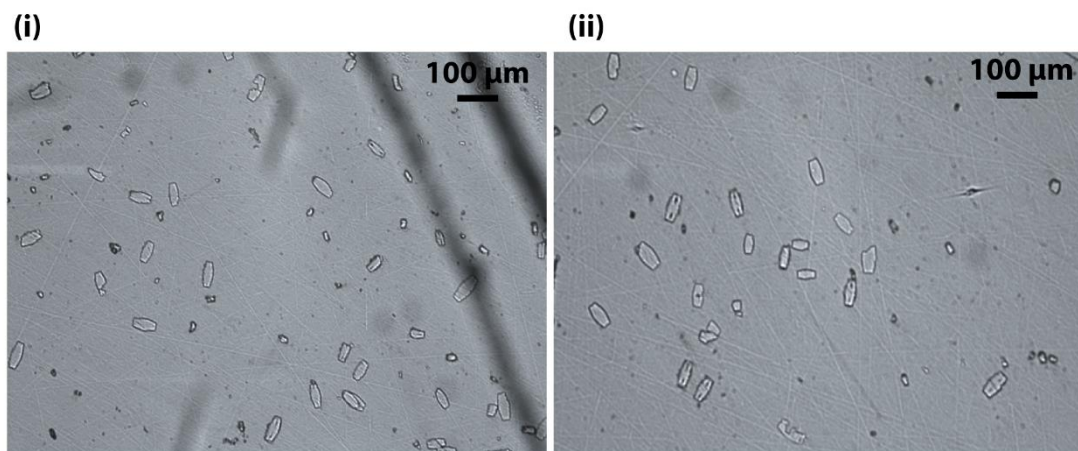


Figure 2.5. Optical images of BIC crystals

2.6. Peak Force Tapping Atomic Force Microscopy

AFM images recorded in chapter 3 were carried out using a BioScope Catalyst™ BioAFM in ScanAsyst mode.⁷ ScanAsyst uses Peak Force Tapping (PFT) mechanism, which works similarly to the standard tapping mode, except that it operates in a non-resonant mode. This provides low tapping frequency range that is well below the cantilever resonance thus, decoupling cantilever response from resonance dynamics. This oscillating system allows direct force control of damaging lateral forces, which is very useful for the topographical imaging of soft samples.

In PFT, the tip is oscillated in the z-position with small amplitude of 100–300 nm (depending on the environment and surface characteristics) and at a specific frequency of 0.25–2.0 kHz.^{7, 8} The z-position is modulated with a sinusoidal wave rather than a triangular one used in conventional force-distance curves resulting in very fast force–distance curves for each image pixel. The maximum probe–sample interaction force (peak force) of each curve is used to control vertical forces. Illustrated in Figure 2.6 (i), as the tip approaches the sample surface (A), it experiences attractive forces (long-range van der Waals) and moves towards the surface (represented by the negative force). As the attractive forces become greater than the cantilever stiffness, the tip gets pulled and comes into contact with the surface (B). The force between the tip and

surface increases until the Z position of the modulation reaches its lowest peak point. This is where the maximum force between the tip and the sample occurs (C) and is maintained constant by a system feedback mechanism. Then as the tip withdraws from the surface, the force decreases until it reaches a minimum point (D). Once, the tip is completely off the surface, it only experiences long range forces. When the tip-sample separation is maximum, the force is very small or zero (E).

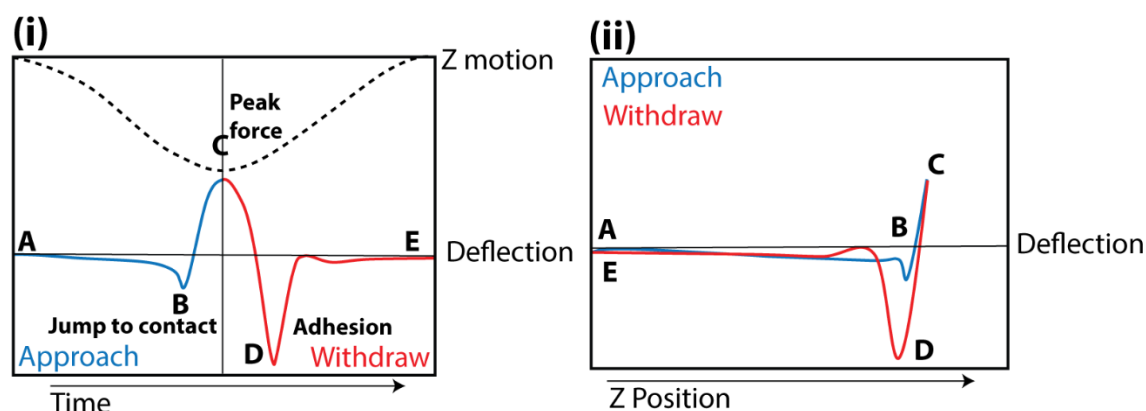


Figure 2.6. (i) Plot of fore and z position as a function of time. (ii) Force versus Z position, typical force curve performed at every pixel position on the sample surface.

2.7. References

- (1) Macpherson, J. V. *Physical Chemistry Chemical Physics* **2015**, 17, 2935-2949.
- (2) Paulose Nadappuram, B.; McKelvey, K.; Byers, J. C.; Güell, A. G.; Colburn, A. W.; Lazenby, R. A.; Unwin, P. R. *Analytical Chemistry* **2015**, 87, 3566-3573.
- (3) Takahashi, Y.; Shevchuk, A. I.; Novak, P.; Zhang, Y.; Ebejer, N.; Macpherson, J. V.; Unwin, P. R.; Pollard, A. J.; Roy, D.; Clifford, C. A.; Shiku, H.; Matsue, T.; Klenerman, D.; Korchev, Y. E. *Angewandte Chemie International Edition* **2011**, 50, 9638-9642.
- (4) McKelvey, K.; Nadappuram, B. P.; Actis, P.; Takahashi, Y.; Korchev, Y. E.; Matsue, T.; Robinson, C.; Unwin, P. R. *Analytical Chemistry* **2013**, 85, 7519-7526.

- (5) Nadappuram, B. P.; McKelvey, K. M.; Byers, J. C.; Güell, A. G.; Colburn, A. W.; Lazenby, R. A.; Unwin, P. R. *Analytical Chemistry* **2015**, 87, 3566-3573.
- (6) Li, C.; Li, C.; Le, Y.; Chen, J.-F. *International Journal of Pharmaceutics* **2011**, 404, 257-263.
- (7) Kaemmer, S. B. *Bruker application note. Bruker Nano Inc., Santa Barbara, CA* **2011**.
- (8) Pittenger, B.; Erina, N.; Su, C. *Application Note Veeco Instruments Inc* **2010**, 1-12.

Chapter 3

Dissolution of Bicalutamide Single Crystals in Aqueous Solution: Significance of Evolving Topography in Accelerating Face-Specific Kinetics

The dissolution kinetics of individual microscale bicalutamide (BIC) form-I crystals are tracked over time using in situ atomic force microscopy (AFM), with the evolution of crystal morphology used to obtain quantitative data on dissolution kinetics via finite element method (FEM) modeling of the dissolution reaction-diffusion problem. Dissolution is found to involve pit formation, and roughening on all dissolving surfaces of the BIC crystal and this has a strong influence on the overall dissolution process and kinetics. While all of the exposed faces (100), {051} and $\bar{1}02$ show dissolution kinetics that are largely surface-kinetic controlled, each face has an intrinsic dissolution characteristic that depends on the degree of hydrogen bonding with aqueous solution, with hydrogen bonding promoting faster dissolution. Moreover, as dissolution proceeds with pitting and roughening, the rate accelerates considerably, so that there is an increasing diffusion contribution. Such insight is important in understanding the oral administration of poorly soluble active pharmaceutical ingredients (APIs) in crystal form. Evidently, surface roughening and defects greatly enhance dissolution kinetics, but the evolving crystal topography during dissolution leads to complex time-dependent kinetics that are important for modeling and understanding API release rates. This work is published in Crystal Growth & Design.

3.1. Introduction

Many active pharmaceutical ingredients (APIs) are administered as solid oral formulations,¹ and the resulting *in vivo* bioavailability is governed by properties such as solubility, permeability, and formulation components, as well as physiological variables. As formulations often include APIs in microcrystalline format, strong dependency of API bioavailability on the dissolution rates of the API crystals has been recognized²⁻⁴ and, consequently, dissolution measurements are a key procedure in drug testing and quality control of pharmaceutical products.^{5,6} Interestingly, there is an increasing trend towards the use of poorly water soluble compounds as candidates for the development of new drugs,⁷ and a comprehensive understanding of the dissolution process of these crystalline APIs is thus of fundamental importance.

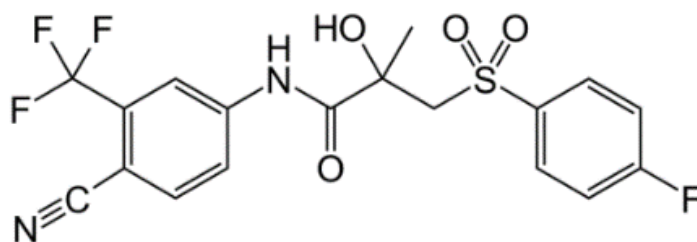
The dissolution of a crystal is a complex physicochemical process driven by local undersaturation at the crystal/solution interface, and consisting of a series of elementary steps involving various surface reactions and mass transport.⁸ The slowest step(s) governs the overall rate and at the simplest level dissolution kinetics can be classified as either surface-controlled (surface processes limit the rate), mass transport-controlled (surface processes are faster compared to diffusion of API molecules from the crystal to bulk solution) or under a mixed regime system, where surface processes and mass transport contributions to the kinetics are comparable. The dissolution process is further complicated when the nature of a molecular crystal surface is considered in more detail. The different arrangement of molecules at different exposed crystal faces and the surface microstructure of those faces (steps, terraces and kinks) make crystal surfaces energetically heterogeneous.^{9,10} The dissolution rate will depend on the energetics associated with each type of site on each surface,¹¹⁻¹⁴ and their contributions and interactions greatly complicate the understanding of the dissolution processes (kinetics and mechanism).^{13,15} Experimental studies need to provide an holistic view¹⁶ of the impact of surface morphology, surface reactivity, driving force and mass transport on dissolution kinetics.

Traditional dissolution testing methodologies for APIs are based solely on measuring bulk solution concentration of a dissolving suspension of a particulates as a function of time.^{17,18} These approaches give average dissolution rates of a population of crystals but do not provide any information about the contribution of the individual crystal faces or the micromorphology changes during the dissolution process.¹⁹⁻²¹ Furthermore, difficulties in the quantification of mass transport in such systems impedes the elucidation of the driving force for dissolution (undersaturation at the crystal/solution interface).

The use of scanning probe microscopy methods such as atomic force microscopy (AFM),^{8,22-24} or scanning ion conductance microscopy (SICM),²⁵ among others,^{26,27,28} has provided detailed kinetic and structural information of dissolution processes. The study of microcrystals by these techniques is particularly advantageous, as this configuration offers high diffusional mass transport rates between the crystal and bulk solution and the possibility of mapping the behavior of entire crystals and the different faces exposed.²⁵ Furthermore, this approach allows the ready combination of experimental data with numerical simulations of mass transport and surface kinetics, making it possible to determine concentration gradients and interfacial concentrations, so as to quantify the dissolution kinetic regime.

The microcrystal approach is adopted herein, using a combination of *in situ* AFM imaging data and finite element method (FEM) simulations, to probe face-specific dissolution of bicalutamide (BIC) (Scheme 3.1) crystals as a function of time. BIC is the API in AstraZeneca's product CASODEX^{®29} and belongs to class II of the biopharmaceutics classification system (BCS) (low solubility and high permeability). It is used to prevent the growth of prostate cancer by blocking the action of androgens on cancer cells.²⁹⁻³¹ The low solubility/dissolution rate of BIC is a major limiting factor for its bioavailability and clinical applications. Accordingly, an in-depth understanding of the microscopic dissolution process in aqueous solution at the single crystal level is expected to be important in leading to new formulation strategies that would enhance

its bioavailability. The approach outlined herein could be generally powerful for revealing the dissolution kinetics of class II API crystals.



Scheme 3.1. Molecular structure of bicalutamide

3.2. Experimental Section

3.2.1. Solutions and Sample Preparation

All chemicals were used as received. Aqueous solutions were prepared using high purity water (Purite, Select HP) with a resistivity of 18.2 MΩ cm at 25 °C. BIC was supplied by AstraZeneca. BIC crystals were grown by mixing 200 μL of a 10 mM solution of BIC dissolved in a mixture of ethanol (≥ 99.5%) and dimethyl sulfoxide (≥ 99.9 %) in 5:1 v/v ratio (solvent) with 400 μL of water (antisolvent) in a plastic petri dish (Willco Well) to create a supersaturated solution. The solution was allowed to stand under a closed environment for 15 min. The supernatant was then removed to reveal plate-like crystals, with the largest dimension in the range 10-60 μm, attached to the petri dish base. The crystals were then rinsed briefly with ultra-pure water and dried using nitrogen (BOC).

3.2.2. X-ray Characterization

Single crystal X-ray analysis was used to determine the unit cell of the grown crystals. A large crystal (100 μm in length, grown for ~1 hour) was mounted on a Mitegen loop

with silicone oil and placed on an Oxford Diffraction Xcalibur Gemini diffractometer fitted with a Ruby CCD area detector. The crystal was kept at 293(2) K during data collection. Using Olex2,³² the structure was solved with the ShelXS-2013³³ structure solution program using Direct Methods and refined with the ShelXL³⁴ refinement package using least squares minimization. The face indexing was performed using CrysAlis PRO (Agilent Technologies UK Ltd.). Powder X-ray diffraction analysis was executed at room temperature using Panalytical X'Pert Pro MPD with hybrid monochromator to give pure CuK α_1 radiation (1.541 Å). The bottom of the petri dish containing the crystals was cut and placed on the sample holder. A Pixcel detector was used in scanning mode over the range $5^\circ < 2\theta < 30^\circ$, stepping 0.02° over a period of 45 min.

3.2.3. *In Situ* Atomic Force Microscopy

Dissolution investigations were performed in 2 mL of unstirred pure water (sink conditions) directly in the petri dish containing the crystals, as grown, using a Bioscope Catalyst microscope with a Nanoscope V controller (Veeco). AFM images of selected diffusionally isolated crystals ($\sim 35\ \mu\text{m}$ in length; separated from neighboring crystals by >20 times this distance) were acquired in *ScanAsyst* mode using silicon-tips on a silicon nitride lever with a spring constant of $0.35\ \text{Nm}^{-1}$ according to manufacturer (SNL-10, Bruker). The images were obtained at a scan rate of 0.45 Hz and the temperature was *ca.* 20 °C. Dissolution rates were measured from consecutive frames acquired at ~ 10 min per frame with a resolution of 256 lines and 512 samples per line. Images acquired were analyzed using SPIP 6.0.14 software, where a first order plane correction was applied making sure the crystal was masked out to correct any background tilt. ISO 11562 Gaussian profile filter was implemented to separate the long and short wave content of a surface profile (roughness and waviness).

3.2.4. Finite Element Method Simulations

Numerical simulations were performed on a Dell Intel core 7i Quad 2.93 GHz computer, equipped with 16 GB of RAM running Windows 7 Professional x64 bit edition using the commercial FEM modelling package Comsol Multiphysics 4.2a (COMSOL AB, Sweden). The “mass transport of diluted species” module was used in the 3D domain illustrated in Figure 3.1 to simulate the mass transport of BIC dissolution during the *in situ* AFM experiments. The models were defined using experimental data that included changes in both the crystal size and morphology and dissolution rates at specific dissolution times. Calculations employed >12000 tetrahedral mesh elements and resolution was defined to be finest near the surface of the crystal. Solution of the partial differential equations for each model was achieved using the direct solver MUMPS in the COMSOL environment with a relative error tolerance of 10^{-6} .

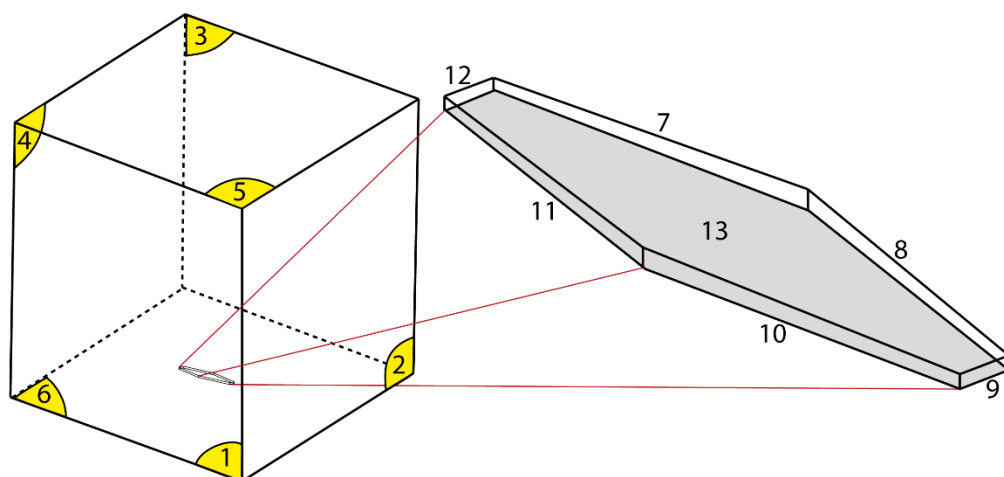


Figure 3.1. Three-dimensional domain (not to scale) used for FEM simulations of BIC dissolution. The numbers correspond to the boundaries described in Table 3.1.

For the experimental length scale, mass transport is predominantly by diffusion. The diffusion time can be estimated using a semi-infinite diffusion model according to equation 1, where t_{diff} is the steady-state diffusion time, d is crystal largest dimension length and D denotes diffusion coefficient.

$$t_{diff} \approx d^2 / D \quad (1)$$

The diffusion coefficient of BIC molecules in aqueous solution ($D = 4.5 \times 10^{-6} \text{ cm}^2 \text{ s}^{-1}$) was calculated using the Wilke-Chang equation (equation 2), where D is the diffusion coefficient, ϕ is the association parameter for the solvent, M_B is the molecular weight of the solvent, μ is the viscosity of the solvent, V_A is the molecular volume of the molecule and T is temperature. It provides diffusivities with an absolute error no bigger than 11%,³⁴ a level that did not have a major impact on our final results.

$$D = \frac{7.4 \times 10^{-8} \times (\phi \times M_B)^{0.5} \times T}{\mu \times V_A^{0.6}} \quad (2)$$

FEM simulations taking into account the upper and lower limit of the diffusion coefficient calculated from the Wilke-Chang correlation showed that the absolute error in the calculation of the solute concentration near the crystal/solution interface and the flux of solute from each individual crystal face was $< 11 \%$, a precision that was sufficient not to affect our conclusions about the kinetic regime. For the dilute solutions during dissolution, D was assumed constant over the entire domain. The characteristic diffusion time for a dissolving crystal ($\sim 35 \text{ } \mu\text{m}$ in length) is about 3 s, which is about 4 orders of magnitude faster than the duration of a typical dissolution experiment (6 h). Mass transport by diffusion was therefore assumed to be at a steady-state, for particular AFM snapshots, and the flux conservation equation (equation 3) was solved, where J is the flux and c is the concentration of the BIC solute.

$$\nabla J = -D \nabla^2 c = 0 \quad (3)$$

Four different geometric models were developed that mimicked the main crystal morphologies found during dissolution. For each model, the experimental data of face

displacement velocity allowed the flux (per unit area) for each crystal face, $J_{\{hkl\}}$,¹³ to be defined. These form the boundary conditions on the crystal surface which, together with the remaining boundary conditions (Table 3.1), allowed equation (3) to be solved to obtain the concentration of BIC in the solution around the dissolving crystal. These simulation data allowed evaluation of the dissolution regime, i.e., mass transport vs. kinetic control, as a function of time. In order to deduce the relative importance of mass transport and surface kinetics, two additional sets of models with the same geometry but different boundary conditions were employed (Table 3.1), such that dissolution of all the crystal faces was controlled by diffusion (crystal/solution interface saturated with soluble BIC), denoted MT1 models, or where only the small and fast dissolving crystal faces $\{051\}$ and $\{\bar{1}02\}$ were controlled by diffusion, denoted MT2 models.

Table 3.1. Boundary conditions applied to the numerical models as defined in Figure 3.1, where \mathbf{n} denotes the outward vector normal to the boundary, c_{bulk} is the bulk concentration (0 μM) and c_{sat} is the saturation solubility of 11.6 μM .

Boundary	Experimental conditions	Mass transport control conditions
1-5	$c = c_{bulk}$	$c = c_{bulk}$
6	$\mathbf{n} \cdot (D\nabla c) = 0$	$\mathbf{n} \cdot (D\nabla c) = 0$
7, 8, 10, 11	$\mathbf{n} \cdot (D\nabla c) = -J_{\{051\},t}$	$c = c_{sat}$
9, 12	$\mathbf{n} \cdot (D\nabla c) = -J_{\{\bar{1}02\},t}$	$c = c_{sat}$
13	$\mathbf{n} \cdot (D\nabla c) = -J_{\{100\},t}$	$c = c_{sat}$

3.3. Results and Discussion

3.3.1. Bicalutamide Crystals

The solid form of BIC presents polymorphism, which has been thoroughly characterized by Vega *et al.*²⁹ Two crystalline forms (I and II) and an amorphous phase of solid BIC have been reported. Single crystal CCD X-ray diffraction determined that the crystallization method described herein produced polymorph I, which is the most stable form, characterized by the monoclinic $P2_1/c$ space group as shown in table 3.2. Optical microscopy revealed the crystals had a plate-like crystal habit, as shown in Figure 3.2 (a). The orientation of the crystals grown in the plastic petri dish was determined by powder X-ray diffraction. Only peaks corresponding to the $(h00)$ reflections ($h=1-4$) were observed, indicating that the crystals were oriented with the (100) faces parallel to the surface, as shown in Figure 3.3. The remaining faces were determined by single crystal X-ray diffraction taking into account the specific angles of the crystal faces. The (hkl) indexes assigned to each crystal face are presented in Figure 3.2 (b).

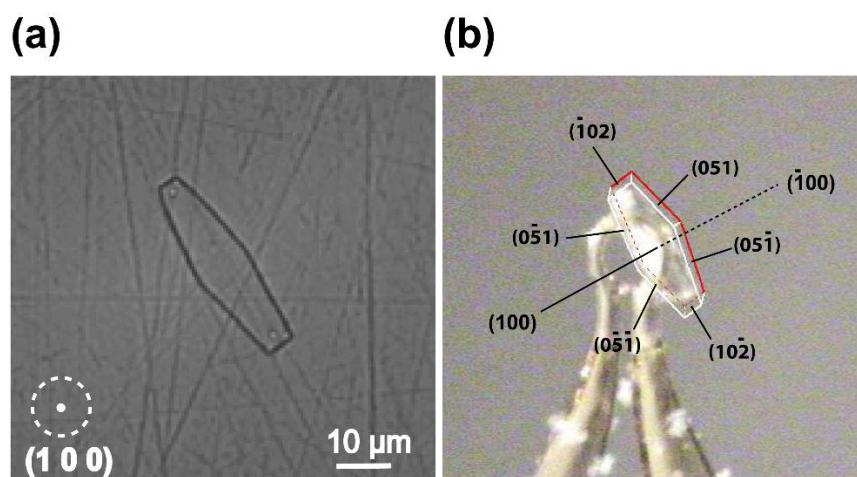


Figure 3.2. Crystal morphology of BIC (Form I). (a) Bright field microscopy image of a typical grown crystal acquired normal to the (100) face. (b) Representation of the single crystal X-ray diffraction of BIC with crystal faces assigned. Red line represents the 2D crystal outline.

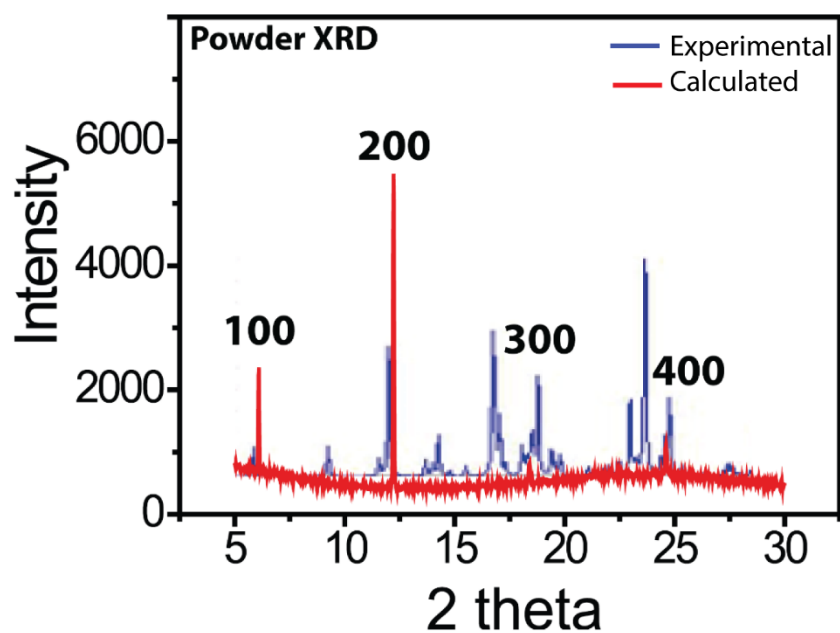


Figure 3.3. Comparison of calculated and experimental PXRD patterns of BIC polymorph I

Table 3.2. Crystal data and structure refinement for BIC

Identification code	BIC
Empirical formula	C ₁₈ H ₁₄ F ₄ N ₂ O ₄ S
Formula weight	430.37
Temperature/K	296(2)
Crystal system	Monoclinic
Space group	P2 ₁ /c

a/Å	14.9237(5)
b/Å	12.2149(3)
c/Å	10.4612(3)
α/°	90
β/°	104.668(3)
γ/°	90
Volume/Å³	1844.84(10)
Z	4
ρ_{calc}/mg/mm³	1.550
m/mm⁻¹	2.201
F(000)	880.0
Crystal size/mm³	0.4 × 0.18 × 0.05
Radiation	CuK α (λ = 1.54184)
2θ range for data collection	6.122 to 155.976°
Index ranges	-18 ≤ h ≤ 15, -7 ≤ k ≤ 15, -11 ≤ l ≤ 12
Reflections collected	7177
Independent reflections	3820 [R_{int} = 0.0233, R_{sigma} = 0.0310]

Data/restraints/parameters	3820/11/282
Goodness-of-fit on F^2	1.038
Final R indexes [$I \geq 2\sigma(I)$]	$R_1 = 0.0478$, $wR_2 = 0.1344$
Final R indexes [all data]	$R_1 = 0.0547$, $wR_2 = 0.1418$
Largest diff. peak/hole / $e \text{ \AA}^{-3}$	0.52/-0.33

3.3.2. Dissolution Rates and Surface Dynamics

Herein, the aqueous dissolution kinetics of microscopic BIC single crystals has been studied by AFM imaging in quiescent conditions. As discussed in the introduction, visualization of the morphology changes of an entire single crystal during dissolution allows the assessment of the dissolution rates of individual crystal faces, providing information on the evolution of surface structure and dissolution activity.³⁵ Additionally, the use of microcrystals generates fast and well-defined mass transport that can be modeled, enabling the quantification of the relative contributions of mass transport and surface kinetics to observed dissolution rates. ScanAsyst mode³⁶ was chosen to operate at very low forces, which minimized tip/sample interactions while enabling high resolution images to be obtained. Additionally, in order to determine if the AFM probe had an effect on dissolution kinetics, dissolution studies of diffusionally isolated BIC single crystals of similar size were performed by optical microscopy. The total dissolution time measured by optical microscopy was broadly comparable to that determined by AFM such that it was possible to discard AFM tip effects promoting the dissolution of the crystals. Other possible effects of the AFM probe on the mass transport of species diffusing from the crystal surface to bulk solution were also considered. As shown in previous work,³⁷⁻³⁹ the AFM tip can block the diffusion of solute and affect the elucidation of the kinetic regime, especially when

the crystal dissolves under a mixed kinetic regime and a very small area of the crystal surface is imaged. However, in the case reported in this work, FEM results show that the dissolution of BIC crystals, in particular the (100) face, is strongly controlled by surface kinetics and small changes in the mass transport of BIC due to the AFM probe can be neglected. Moreover, the whole crystal is imaged by the AFM probe, allowing the natural mass transport behavior of the system to be quickly recovered when the tip moves laterally a few microns, as shown in other works that studied the influence of AFM probe position and geometry on diffusion to ultramicroelectrodes in an *in situ* AFM environment.⁴⁰

Measurements were made on different crystals, and although there were some differences between them, the phenomena observed and the time course of dissolution was broadly similar. The data in detail for one crystal are provided below and further examples will be provided later on in this chapter. Figure 3.4 (a) presents time-dependent 3D AFM images of a dissolving BIC microcrystal in aqueous solution. In the early stages, AFM measurements show the formation of pits on the top surfaces, as well as roughening of the side faces. The dissolution velocity of the (100) faces was followed by tracking the changes in the average crystal height over the entire crystal area as a function of time, whereas the dissolution velocities of the {051} and {102} faces were determined from the perpendicular retreat of the faces as referenced in Figure 3.4 (b). The mean of the 2 cross-sectional lines, forming right angles between parallel {051} faces, as shown in Figure 3.4 (b), was used as the average width. The mean of 9 cross-sectional lines along the direction labeled as length in Figure 3.4 (b) was used to extract the average length of the crystal at each frame. Measurements were extracted for all dimensions until the dissolution time reached 240 mins. Within this time range, measurements could be made with good certainty, since the crystal showed a well-defined morphology. Figure 3.4 (c) plots the displacement behavior in the length and width dimensions. The displacement slope of the {102} faces (length) is steeper than the {051} faces (width), indicating faster dissolution rate. The increase in rate with time can be understood from visual analysis of the AFM images, showing

that the initiation and propagation of pits, and face roughening, over time have a great impact on the rate at which the BIC crystal faces dissolve.

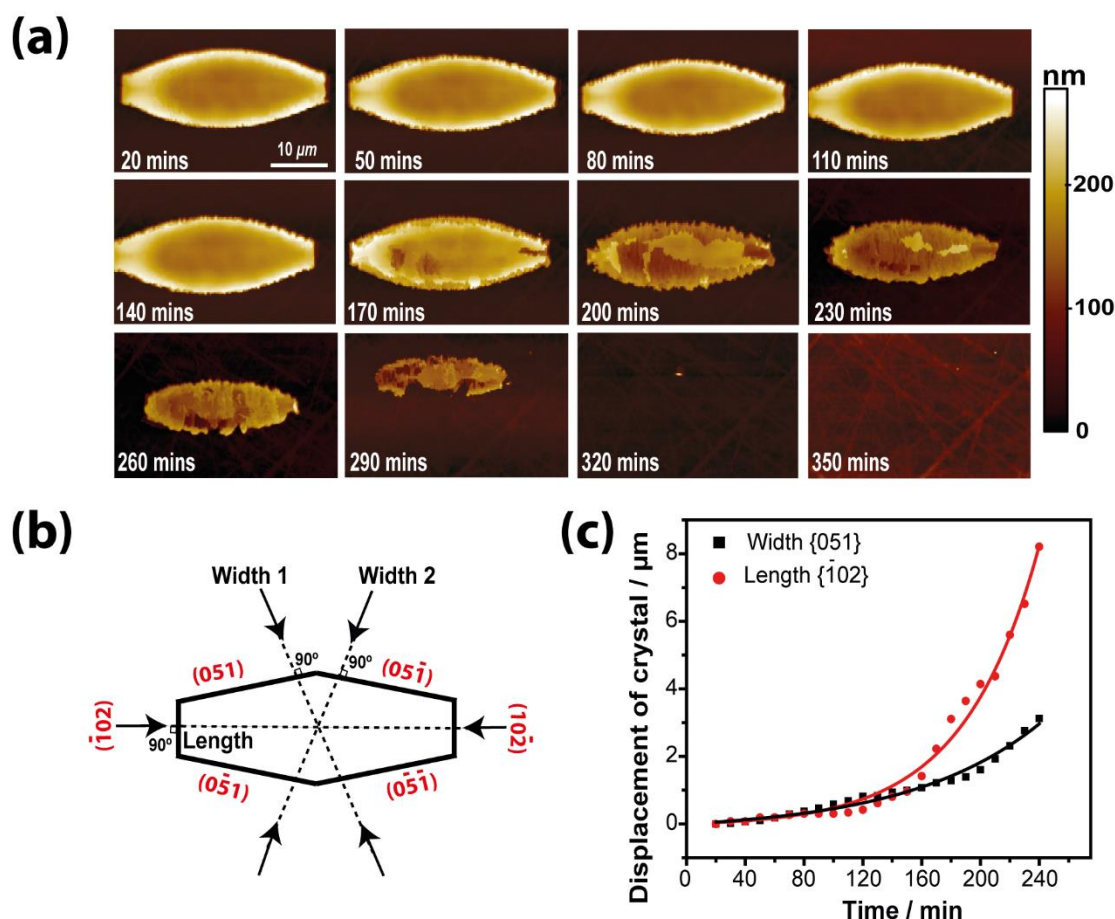


Figure 3.4. (a) AFM images of a single BIC microcrystal (initially 36 μm in length and 10.5 μm in width) during dissolution in aqueous solution. (b) 2D BIC crystal morphology indicating how displacement data were extracted. (c) Plot showing the changes in width and length over time of the dissolving BIC crystal shown in (a).

The overall displacement of the (100) , $\{051\}$ and $\{\bar{1}02\}$ faces with time fit well to an exponential function (Figure 3.4 (a)). Data were fitted empirically to such a function (equation 4) to yield the best R^2 value included in the software OriginPro 9.1.0.

$$y = A(1 - \exp^{-Bx}) \quad (4)$$

The best linear fits in the early and late time period are shown by the blue dotted lines. Molar dissolution rates of the individual crystal faces were determined directly from the data in Figure 3.4 (a) using equation 5, where $v_{(hkl)}$ is the dissolution velocity of the $\{hkl\}$ face (gradient / 2 of the plots in Figure 3.5 (a) (only for the width and length)) and $V_{m(BIC)}$ is the molar volume of BIC calculated from the density of the BIC polymorph (1.55 g cm^{-3}).

$$\text{molar flux} = v_{(hkl)} \times V_{m(BIC)} \quad (5)$$

The slowest dissolution rate was found to be for the (100) face. The dissolution rates of the $\{051\}$ and $\{\bar{1}02\}$ faces were faster, but both increased markedly with time (Figure 3.5 (b) (ii-iii)). As alluded to above, these changes are mainly associated with changes of the crystal surface energy, due to the evolving face topography.

Further insight into the dissolution process was obtained by conducting an analysis of the relationship between dissolution rate and surface roughness, as determined by AFM, normalized by the changes in geometric surface area as a function of time (Figure 3.5 (c)). This procedure is most accurate for the top (100) face because full images of the surface are obtained in detail. It can be seen that surface area-normalized roughness increases by less than a factor of two, yet the rate of reaction over this time period increases by a factor of six. Although AFM may not provide a view of atomic-scale defects, it appears that the rate is not simply proportional to surface roughness. Rather as dissolution proceeds, sites of higher reactivity, including high-index nanofacets, are produced which accelerate the reaction.

The roughness of the $\{051\}$ and $\{\bar{1}02\}$ faces is more difficult to quantify, but it can be seen from Figure 3.5 (a) (ii) and (iii) and (b) (ii) and (iii) that the dramatic increase in rate is far more extensive than could be explained from the roughening of the crystal side faces (Figure 3.4 (a)). Indeed, these images highlight the formation of high index faces (manifested as indents) around the crystal perimeter.

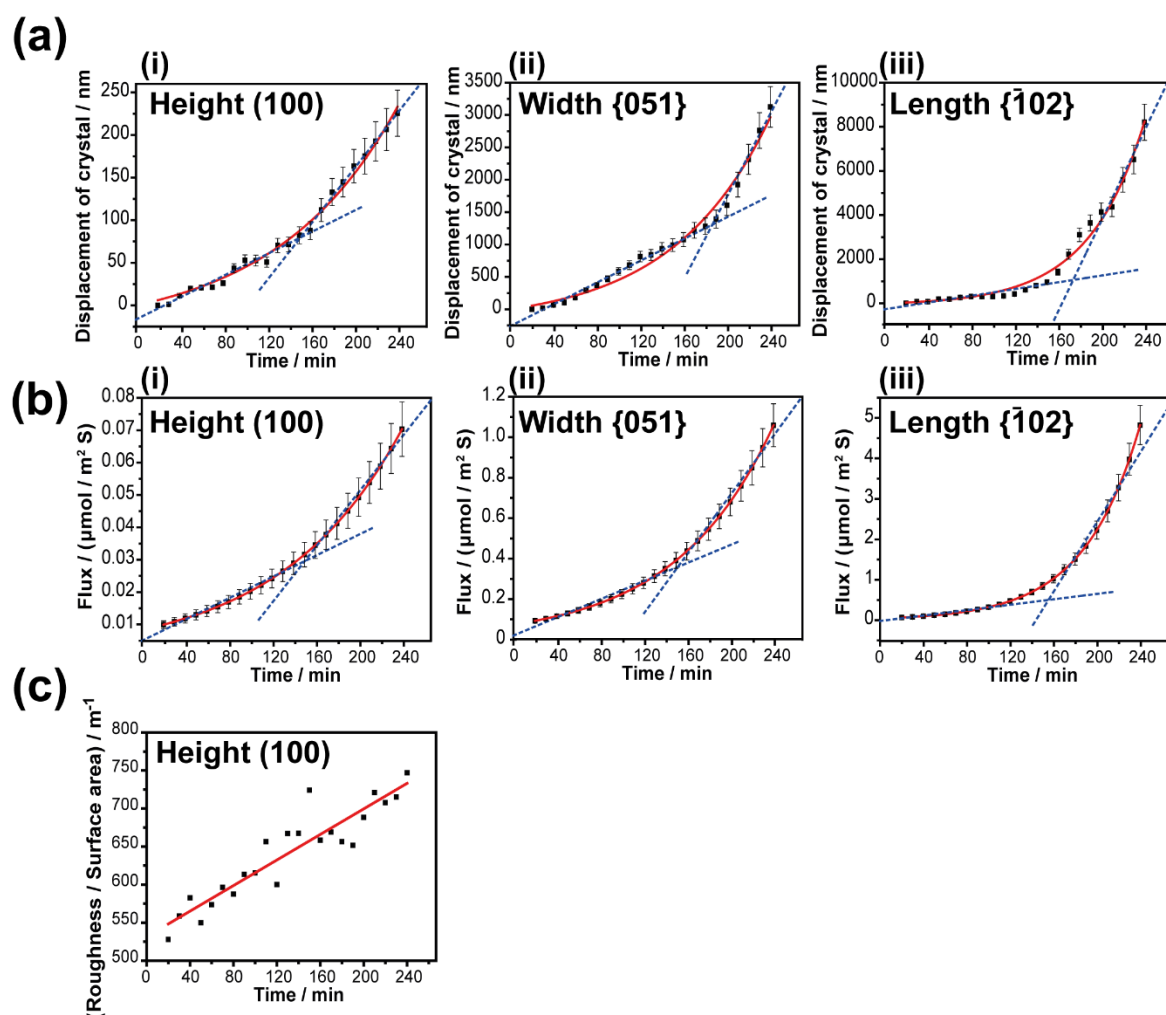


Figure 3.5. (a) Plots showing changes in crystal dimensions over time: (i) Height (100), (ii) Width {051} and (iii) Length {102}. (b) Corresponding dissolution rates (flux) over time: (i) Height (100), (ii) Width {051} and (iii) Length {102}. Data are fitted to an exponential function (solid red curves) and the blue linear portions highlight the change in the rate for the basal surface and roughened surfaces at early and advanced dissolution times. (c) Plot showing the change in surface roughness of (100) face normalized by the geometric surface area as a function of time.

Initially, the crystal faces are relatively flat (low step edge and kink density), so the overall activation energy for dissolution tends to be larger.⁴¹ The data presented indicate that as dissolution proceeds, the crystal surface roughens, the edges become rounded and new crystal faces of higher crystallographic indexes are exposed to the solvent as shown in Figure 3.6.

Etch-pits produced on the (100) face, imaged directly by AFM (Figure 3.4 (a)), show that the distribution is non-uniform and etch-pits do not present a particular crystallographic orientation. All the crystal faces present high-degree of surface etch-pitting at long dissolution times, which explains the slope difference in the two linear regions of all plotted dissolution rates versus time, in Figure 3.5 (b), and the newly exposed reactive sites cause the increase in the dissolution rate.^{42,43} The dissolution of additional crystals were analyzed to confirm this observations, as shown below in Figures 3.7-9).

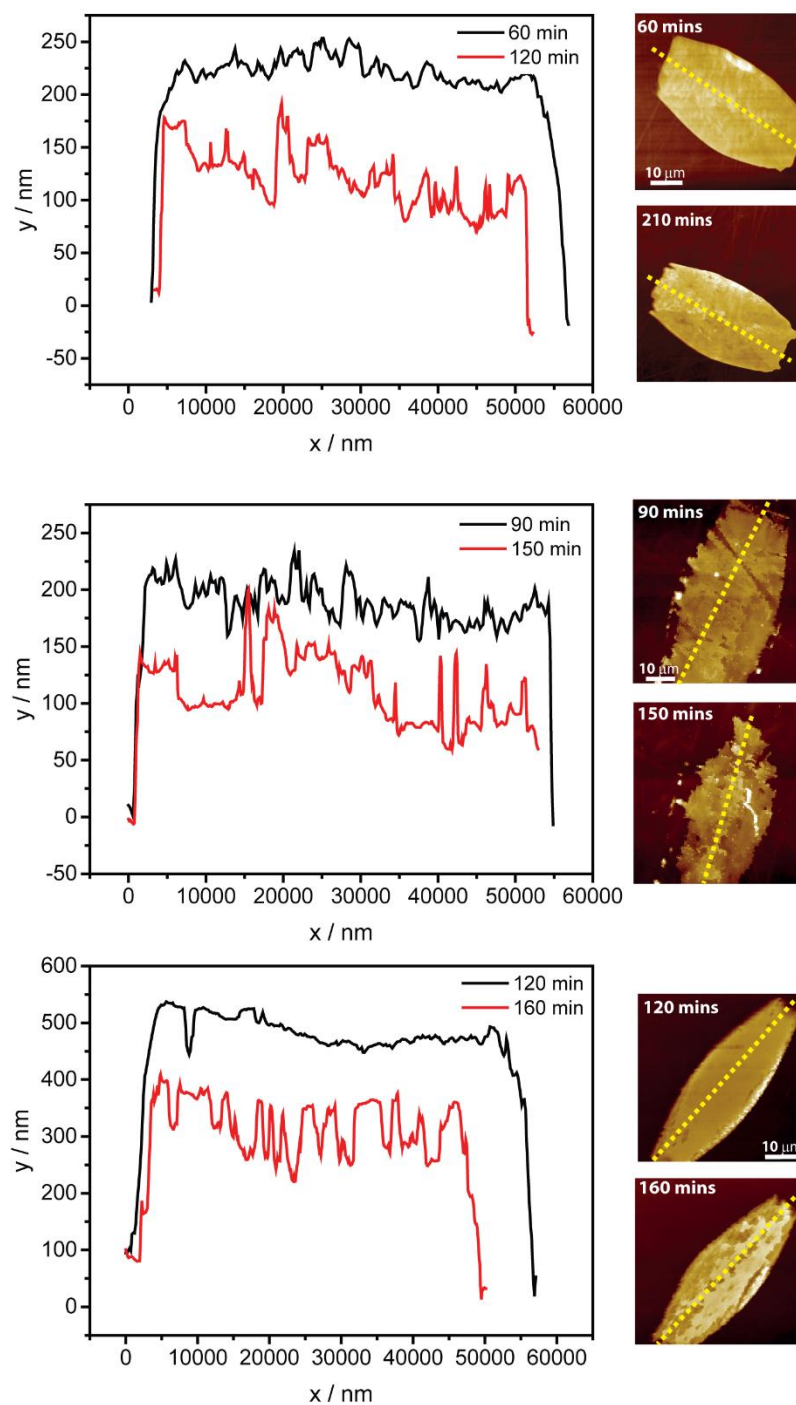


Figure 3.6. Graphs showing cross-sections of dissolved BIC crystals at various time points.

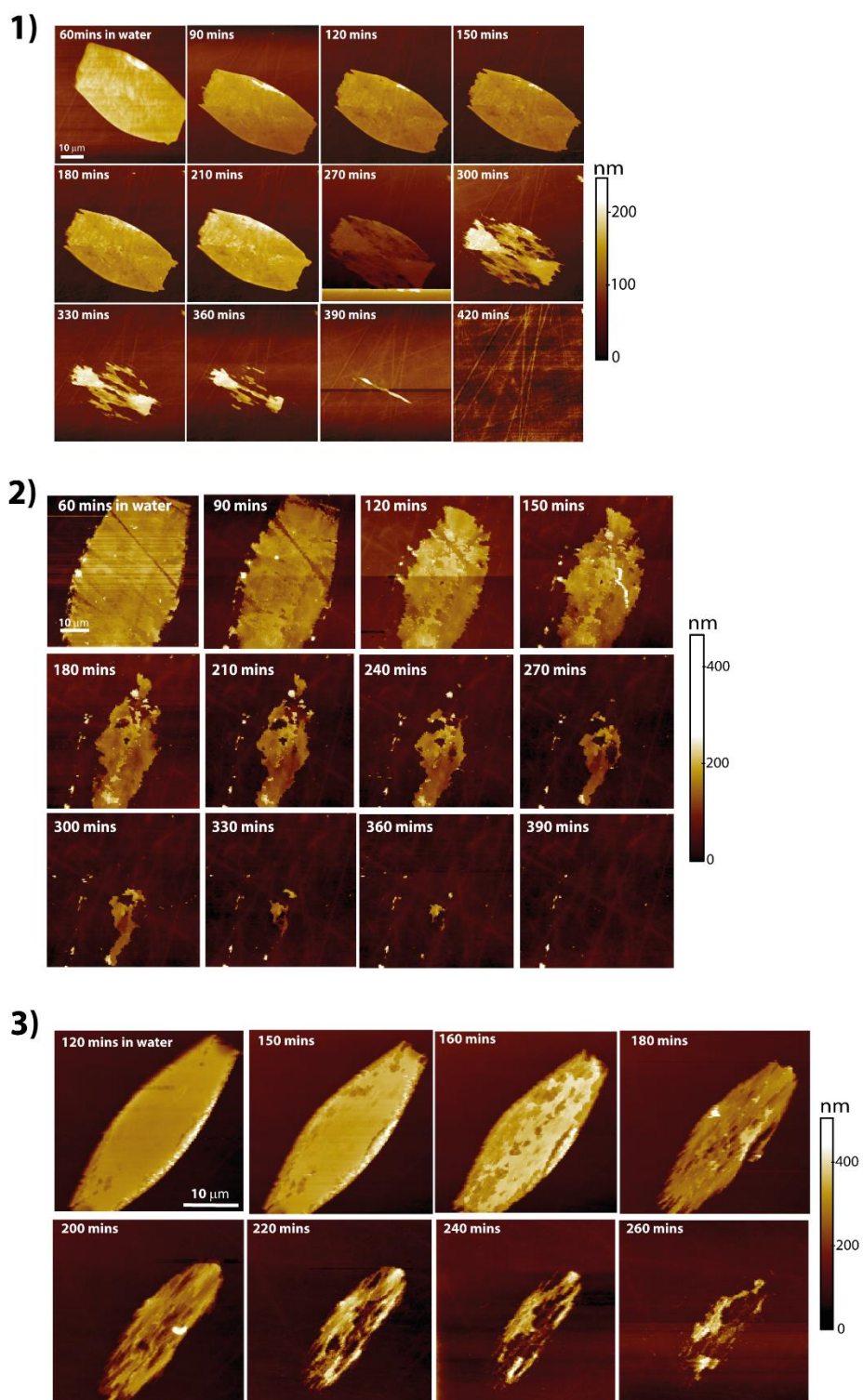


Figure 3.7. AFM topography images of aqueous dissolution sequence of 3 different single BIC crystals.

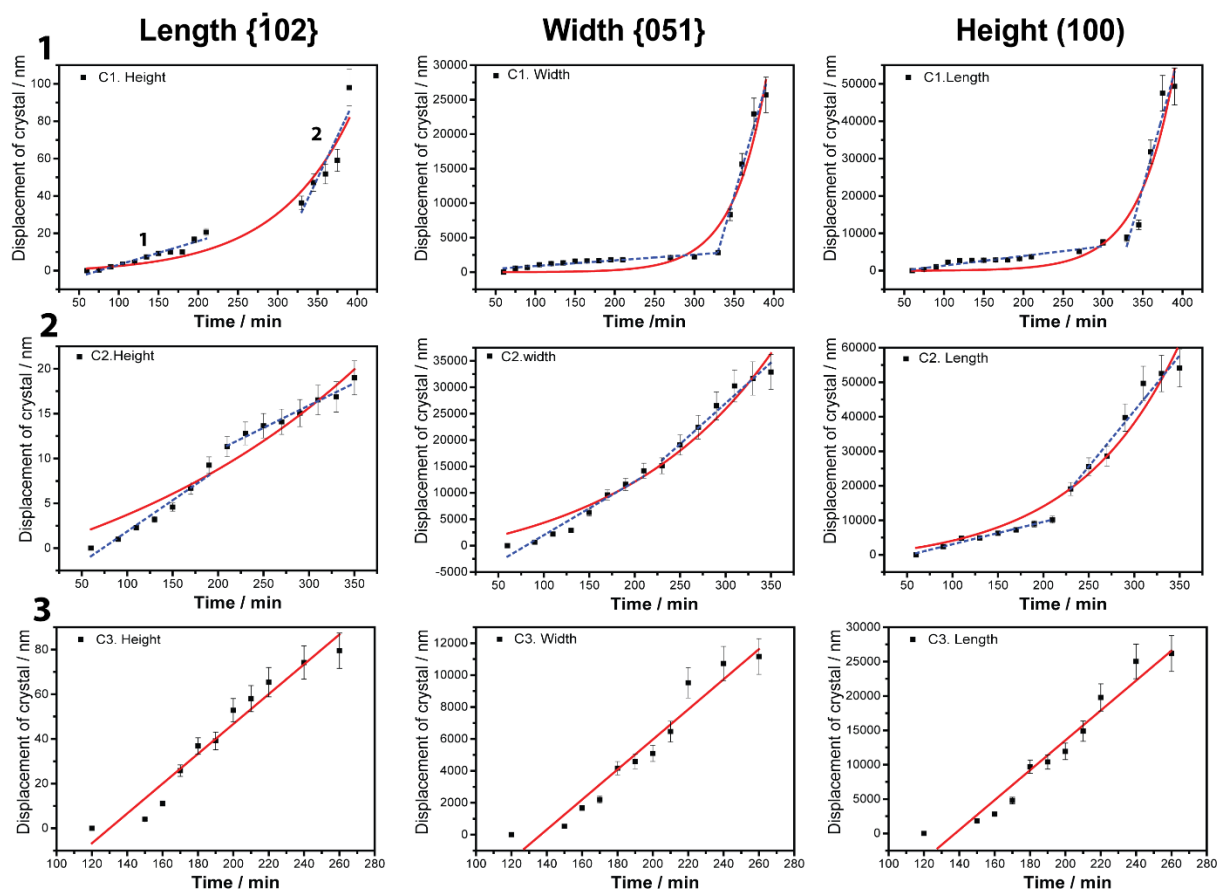


Figure 3.8. Plots showing changes in crystal dimensions over time of the crystals shown in Figure 3.7.

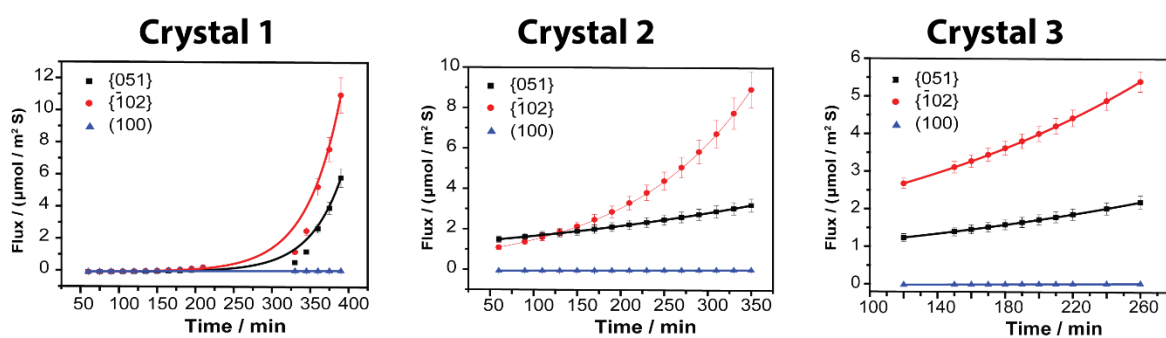


Figure 3.9. Corresponding dissolution rates (flux per unit area) over time of the crystals shown in Figure 3.7.

Plots in Figure 3.9 illustrate that as the crystal starts to roughen the dissolution rate increases significantly. The order of the measured dissolution rates for all three crystals was found to be: $(100) < \{051\} < \bar{1}02$.

Although all examined BIC crystals showed broadly similar behavior, they dissolved at different rates despite their similarity in size (~ 50 - $60\ \mu\text{m}$ in length). This is attributed to the different crystal surface characteristics, such as the number and type of defects in each crystal, which with time increasingly lead to the emergence of high index faces that impact on dissolution kinetics at longer times. The creation of reactive dissolution sites is considered to be an indicator of surface-controlled dissolution,^{9,10,13} but to confirm the kinetic regime, the determination of the solute concentration near the crystal/solution interface and the quantification of the surface reactivity and diffusion contributions to the dissolution process is necessary (*vide infra*). These observations build on our recent dissolution kinetics measurements of salicylic acid in aqueous solution using hopping intermittent contact scanning electrochemical microscopy²⁷ and the aqueous dissolution of the organic crystal, furosemide, using the combination of scanning ion conductance microscopy and optical microscopy.²⁵ Both studies highlight the strong influence of evolving surface roughness on the overall dissolution kinetics time-course.

The face-specific dissolution rates at the beginning of the dissolution process corresponds to the dissolution of the (100) , $\{051\}$ and $\bar{1}02$ faces presented in the initial crystal habit. As highlighted above, crystal surface energy has a huge impact on the overall dissolution rate, and this was examined, as shown in Figure 3.10 (generated using the unit cell parameters of the crystal structure JAYCES available in the CCDC²⁹ and using the commercial package Mercury 3.8, CCDC Cambridge⁴⁴). Considering the (100) face presented in Figure 3.10 (a), the hydrogen bonding network is contained within the (100) plane with the exposure of fluorobenzene rings at the surface. This is the characteristic of a face with a low surface energy and slow growth.⁴⁵ In contrast, the $\bar{1}02$ face structure (Figure 3.10, (b)), exposes a sulphonyl group at the surface

and results in a hydrogen bonding network perpendicular to the $(\bar{1}02)$ plane, making the $(\bar{1}02)$ face a high energy surface. This behavior is also seen in the (051) face, although to a smaller extent compared to the $(\bar{1}02)$ face, highlighted by the exposure of trifluoromethyl benzonitrile group at the surface and the zig zag arrangement of the hydrogen bonds along the structure shown in Figure 3.10 (c). The order of the measured dissolution rates (Figure 3.5 (b)) of the different faces: $(100) < \{051\} < \{\bar{1}02\}$, agrees with the hydrogen bonding model, i.e. the greater the degree of hydrogen bonding between the surfaces and adjacent solution, the faster the dissolution kinetics. It is reasonable to assume that the relative dissolution rates of the different faces for this period of time would mirror the order of the attachment energies of BIC molecules to the surface, as would occur during crystal growth, and as found in our previous work on furosemide.²⁵

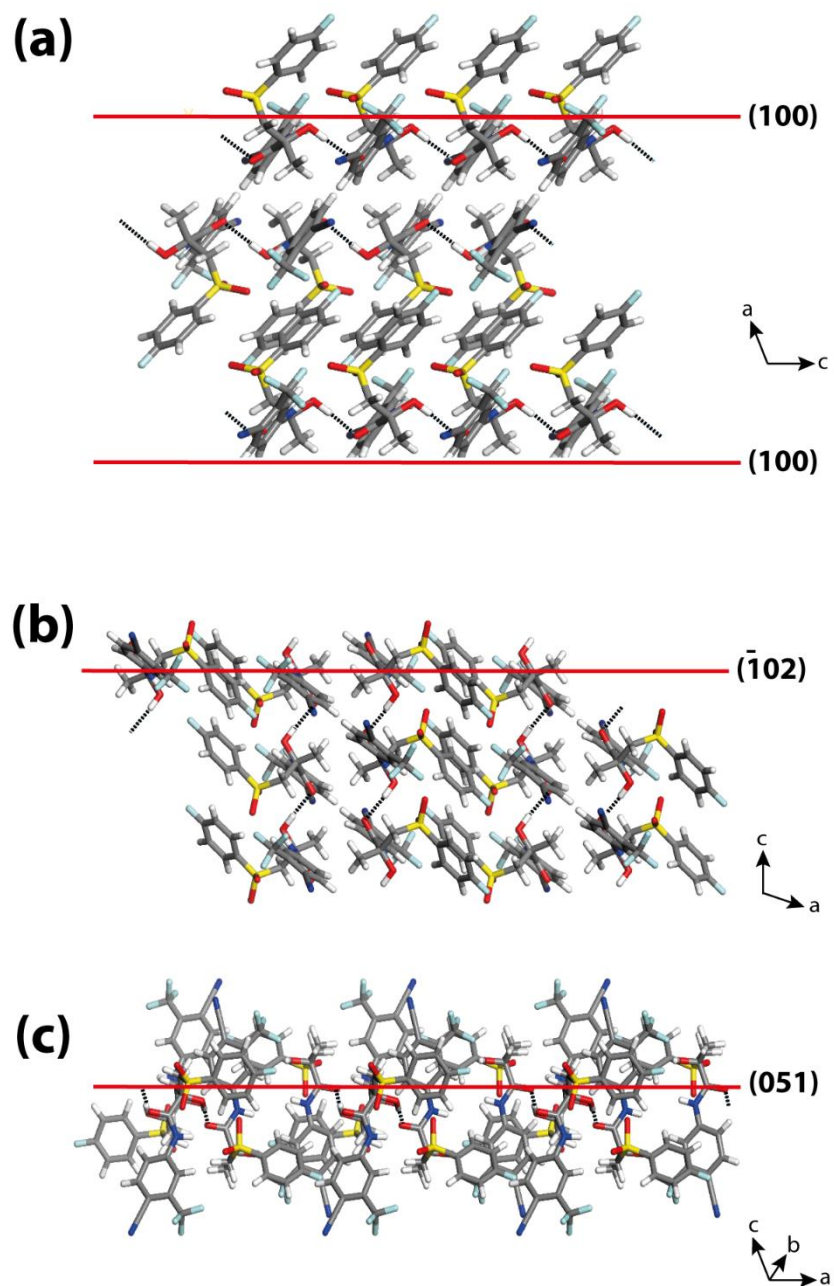


Figure 3.10. Structure of BIC crystal faces: (a) (100), (b) $(\bar{1}02)$ and (c) (051). Black dotted lines highlight hydrogen bonds. Acquired using Mercury 3.8, CCDC Cambridge using the structure JAYCES.

3.3.3. Determination of Interfacial Concentrations and Kinetic Regime

In the case of a mixed surface kinetic-diffusion regime, the concentration of solute molecules near the crystal surface has an intermediate value between close to bulk concentration (pure kinetic control) and equilibrium (saturated) value (diffusion control). The actual value depends on the relative contributions of mass transport and surface kinetics.³⁹ To elucidate how the kinetic regime during the dissolution of BIC crystals evolves with time, the concentration of BIC solute near the crystal/solution interface during dissolution was calculated by FEM simulations formulated directly from AFM experimental data.

Because the crystal size, morphology and dissolution rates of the individual crystal faces are time-dependent, four different steady-state FEM models at different dissolution times were formulated to evaluate the evolution of the kinetic regime with time. The computations used the experimental dissolution rates determined for each crystal face and the crystal size and morphology determined from AFM images at each dissolution time (20 min, 80 min, 170 min and 230 min). The crystal morphology was approximated to smooth surfaces, i.e. to the underlying basal surface, considering the difficulty of constructing and assigning overall dissolution rates to rough surfaces in the FEM modelling package. The results of the FEM calculations (Figure 3.11 (a)) revealed that $c_{surf\{102\}} > c_{surf\{051\}} > c_{surf\{100\}}$ during the whole dissolution process, and that all the $c_{surf\{hkl\}}$ values increase with time consistent with the kinetic coefficient for dissolution increasing as dissolution proceeds. At the beginning, $c_{surf\{hkl\}}$ is very similar to the bulk concentration. This is consistent with a dissolution process controlled by surface kinetics in which the rate of the surface reaction is much slower than the rate of surface to bulk diffusion. As dissolution proceeds, AFM imaging indicates that more reactive sites are formed and surface dissolution kinetics increase, leading to higher $c_{surf\{hkl\}}$. Consequently, concentration gradients from the crystal to bulk solution become steeper, indicating an increasing contribution from diffusion. However, surface kinetics still dominate, since $c_{surf\{hkl\}}$ is well below the equilibrium

concentration value ($11.62 \mu\text{M}$, at 20°C)⁴⁶ during the entire dissolution process (see supporting information, section 3.5.1).

To evaluate the relative contributions of mass transport and surface kinetics on dissolution, these results were compared to those obtained from FEM calculations parameterized for the same crystal size and geometry at each dissolution time, but where a pure diffusion controlled dissolution regime was imposed at specific crystal faces, $c_{surf\{hkl\}}=c_{sat}$, (Figure 3.11 (b-c)). It can be seen that the surface concentration is much larger when dissolution is diffusion-controlled. A first comparison of Figure 3.11 (a) and (b) indicates how the experimental system evolves towards increasing diffusion control with time. This is also highlighted in Figure 3.12, which shows plots of the ratio of diffusion to experimental fluxes (J_{MT}/J_{obs}) for the different faces versus time. J_{MT1} is the predicted flux for a process where the dissolution of all the crystal faces is purely diffusion-limited and J_{obs} is the measured flux. During the early stages, the dissolution rates of the BIC crystal would be at least two orders of magnitude higher if dissolution of all the crystal faces was limited by diffusion (MT1 model). Whereas at later stages, the magnitude of the experimentally obtained fluxes tend towards those calculated for a pure diffusion-limited system (see supporting information, section 3.5.1), particularly for the $\{\bar{1}02\}$ faces, which are those that dissolve the fastest. It is important to note, that the flux magnitude is strongly influenced by the crystal morphology and size, and under mixed kinetic control, the crystal geometry and the BIC concentration at adjacent crystal faces. In the MT1 model, the concentration of BIC near all the crystal faces is c_{sat} , an extreme situation that does not take into account the acute anisotropic kinetic character for dissolution of the different (hkl) crystal faces observed experimentally (different balance between mass transport and surface kinetics for each family of faces, *vide supra*). Under mixed kinetic control, the flux of solute molecules arising from the most morphologically important face, the (100) face, affect the apparent behavior of the very small adjacent faces. To illustrate this point, a third set of models where only the dissolution of the $\{051\}$ and $\{\bar{1}02\}$ faces was forced to be diffusion-limited and the slow dissolving large

basal (100) face behaved as observed experimentally, were formulated (MT2). In this situation, the calculated molar flux of BIC, J_{MT2} at the {051} and $\bar{1}02$ faces is much higher than that calculated by MT1 for each dissolution time (Figure 3.12). The kinetic regime of these smaller faces is then in good agreement when comparing either concentrations near the crystal/solution interface or flux of material (J_{MT2}/J_{obs}). Further, through this model, one can even appreciate the effect of the influence of the concentration near the {051} and $\bar{1}02$ faces on the calculation of $c_{surf, (100)}$. This is observed to be enhanced compared to that calculated in the experimental model, despite the fact that the flux applied was the same in each case, $J_{obs, (100)} = J_{MT2, (100)}$ as shown in the supporting information, section 3.5.1.

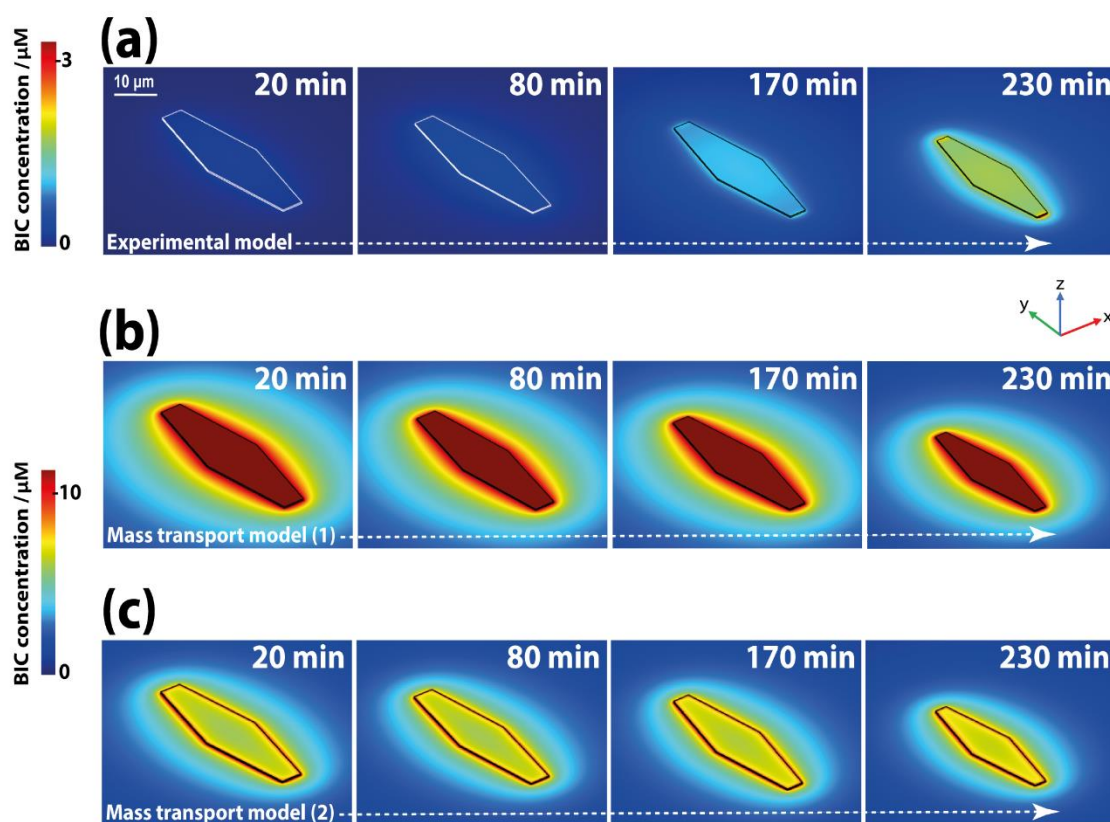


Figure 3.11. FEM simulation for the dissolution of a BIC crystal in bulk aqueous solution at different time points: (a) model formulated from experimental data. (b) a MT1 model where the dissolution of all faces is purely diffusion-controlled; and (c)

MT2 model where only the $\{051\}$ and $\{\bar{1}02\}$ faces are diffusion-controlled and the $\{100\}$ face dissolves as observed experimentally. Note the difference in the concentration ranges for (a) and (b)-(c)

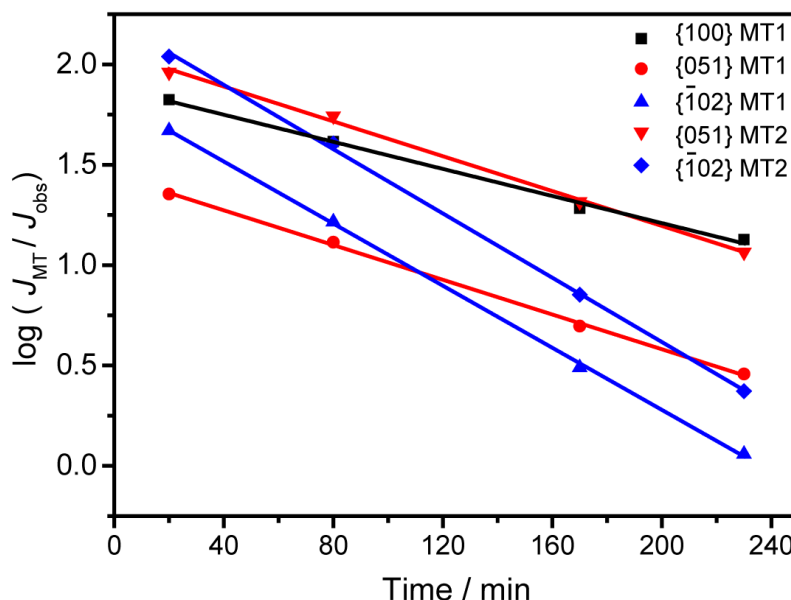


Figure 3.12. Comparative plots of J_{MT}/J_{obs} versus time for the $\{100\}$ faces (black), $\{051\}$ faces (red) and $\{\bar{1}02\}$ faces (blue), showing the extent to which each face evolves towards increasing mass transport contribution during dissolution in the case where all the crystal faces are diffusion-limited (MT1) and where only the $\{051\}$ and $\{\bar{1}02\}$ faces are diffusion-limited (MT2).

3.4. Conclusions

In this study, the combined use of *in situ* AFM measurements and FEM modeling has allowed the surface processes that accompany dissolution to be monitored quantitatively in real-time to obtain dissolution kinetics for individual faces of a single BIC microcrystal. Morphological changes and the formation of pits associated with surface-controlled dissolution were observed. At longer dissolution times, the

roughening of individual crystal faces and the exposure of high index faces result in greatly increased dissolution kinetics. Incorporating AFM experimental data into a FEM model of a dissolving BIC microcrystal has provided direct concentration distributions at individual crystal faces. As a result, the importance of surface kinetics compared to mass transport for each crystal face was determined. All BIC crystal faces showed significant surface kinetic-controlled dissolution behavior, being far from the mass transport limited regime, but with increasing mass transport (diffusion) contribution to the kinetics as the reaction proceeded.

The study of single microcrystals provides considerable understanding of API crystal dissolution kinetics and could provide strategic insight for the future engineering of drug crystals with appropriate dissolution characteristics whilst maintaining suitable physical and chemical stability. For example, these studies have shown that roughened and defect-rich surfaces have greatly enhanced dissolution kinetics. Further, the significant time-dependence of the dissolution kinetics is important for improved pharmacokinetic modeling.

3.5. Supporting Information

3.5.1. Interfacial Concentration Values

Table 3.3. Concentration near the crystal/solution interface and normal total fluxes at various times for the different crystal faces calculated from FEM simulations.

Time (min)	Faces $\{hkl\}$	C_{surf} Experimental (mol m ⁻³)	C_{surf} MT1 (mol m ⁻³)	C_{surf} MT2 (mol m ⁻³)	J_{obs} (mol m ⁻² s ⁻¹)	J_{MT1} (mol m ⁻² s ⁻¹)	J_{MT2} (mol m ⁻² s ⁻¹)
20	100	2.38×10^{-4}	1.16×10^{-2}	7.02×10^{-3}	9.94×10^{-9}	6.63×10^{-7}	9.94×10^{-9}
20	051	2.68×10^{-4}	1.16×10^{-2}	1.16×10^{-2}	9.27×10^{-8}	2.09×10^{-6}	7.52×10^{-6}
20	$\bar{1}02$	2.04×10^{-4}	1.16×10^{-2}	1.16×10^{-2}	6.87×10^{-8}	3.21×10^{-6}	8.47×10^{-6}
80	100	3.93×10^{-4}	1.16×10^{-2}	7.03×10^{-3}	1.69×10^{-8}	6.98×10^{-7}	1.69×10^{-8}
80	051	4.45×10^{-4}	1.16×10^{-2}	1.16×10^{-2}	1.80×10^{-7}	2.34×10^{-6}	8.84×10^{-6}
80	$\bar{1}02$	4.01×10^{-4}	1.16×10^{-2}	1.16×10^{-2}	2.19×10^{-7}	3.60×10^{-6}	9.95×10^{-6}
170	100	9.45×10^{-4}	1.16×10^{-2}	7.21×10^{-3}	3.77×10^{-8}	7.24×10^{-7}	3.77×10^{-8}
170	051	1.11×10^{-3}	1.16×10^{-2}	1.16×10^{-2}	4.88×10^{-7}	2.42×10^{-6}	8.88×10^{-6}
170	$\bar{1}02$	1.45×10^{-3}	1.16×10^{-2}	1.16×10^{-2}	1.25×10^{-6}	3.85×10^{-6}	1.01×10^{-5}
230	100	1.55×10^{-3}	1.16×10^{-2}	7.46×10^{-3}	6.43×10^{-8}	8.62×10^{-7}	6.43×10^{-8}
230	051	1.90×10^{-3}	1.16×10^{-2}	1.16×10^{-2}	9.48×10^{-7}	2.72×10^{-6}	9.35×10^{-6}
230	$\bar{1}02$	3.42×10^{-3}	1.16×10^{-2}	1.16×10^{-2}	3.97×10^{-6}	4.55×10^{-6}	1.10×10^{-5}

J_{MT1} = Theoretical flux obtained for when all crystal faces are purely diffusion controlled, J_{MT2} = Flux obtained when only the {051} and $\{\bar{1}02\}$ faces are purely diffusion controlled and the (100) face as observed experimentally and J_{obs} = Experimental flux.

3.6. References

- (1) Chen, J.; Sarma, B.; Evans, J. M. B.; Myerson, A. S. *Crystal Growth & Design* **2011**, *11*, 887-895.
- (2) Stegemann, S.; Leveiller, F.; Franchi, D.; de Jong, H.; Lindén, H. *European Journal of Pharmaceutical Sciences* **2007**, *31*, 249-261.
- (3) Brouwers, J.; Brewster, M. E.; Augustijns, P. *Journal of Pharmaceutical Sciences* **2009**, *98*, 2549-2572.
- (4) Blagden, N.; de Matas, M.; Gavan, P. T.; York, P. *Advanced Drug Delivery Reviews* **2007**, *59*, 617-630.
- (5) Dokoumetzidis, A.; Macheras, P. *International Journal of Pharmaceutics* **2006**, *321*, 1-11.
- (6) Guidance for Industry: Dissolution Testing of Immediate Release Solid Oral Dosage Forms. U.S. Department of Health and Human Services Food and Drug Administration Center for Drug Evaluation and Research (CDER): Rockville **1997**.
- (7) Ku, M. S. *The AAPS Journal* **2008**, *10*, 208-212.
- (8) Unwin, P. R.; Macpherson, J. V. *Chemical Society Reviews* **1995**, *24*, 109-119.
- (9) MacInnis, I. N.; Brantley, S. L. *Chemical Geology* **1993**, *105*, 31-49.
- (10) MacInnis, I. N.; Brantley, S. L. *Geochimica et Cosmochimica Acta* **1992**, *56*, 1113-1126.

- (11) Mullin, J. W. *Crystallization*; Butterworth-Heinemann: Oxford; Boston, 2001.
- (12) Lasaga, A. C.; Luttge, A. *Science* **2001**, *291*, 2400-2404.
- (13) Blum, A. E.; Yund, R. A.; Lasaga, A. C. *Geochimica et Cosmochimica Acta* **1990**, *54*, 283-297.
- (14) den Brok, S. W. J.; Morel, J. *Geophysical Research Letters* **2001**, *28*, 603-606.
- (15) Ritchie, G. S. P. In *Advances in Agronomy*, Donald, L. S., Ed.; Academic Press, 1994, pp 47-83.
- (16) Peruffo, M.; Mbogoro, M. M.; Edwards, M. A.; Unwin, P. R. *Physical Chemistry Chemical Physics* **2013**, *15*, 1956-1965.
- (17) Gray, V.; Kelly, G.; Xia, M.; Butler, C.; Thomas, S.; Mayock, S. *Pharmaceutical Research* **2009**, *26*, 1289-1302.
- (18) Coombes, S. R.; Hughes, L. P.; Phillips, A. R.; Wren, S. A. C. *Analytical Chemistry* **2014**, *86*, 2474-2480.
- (19) Nguyen, T. T. H.; Hammond, R. B.; Roberts, K. J.; Marziano, I.; Nichols, G. *CrystEngComm* **2014**, *16*, 4568-4586.
- (20) Missel, P. J.; Stevens, L. E.; Mauger, J. W. *Pharmaceutical Development and Technology* **2005**, *9*, 453-459.
- (21) Qiu, Y.; Rasmuson, Å. C. *AIChE Journal* **1990**, *36*, 665-676.
- (22) Danesh, A.; Connell, S. D.; Davies, M. C.; Roberts, C. J.; Tendler, S. J.; Williams, P. M.; Wilkins, M. J. *Pharmaceutical Research* **2001**, *18*, 299-303.
- (23) Abandan, R. S.; Swift, J. A. *Crystal Growth & Design* **2005**, *5*, 2146-2153.
- (24) Gasharova, B.; Göttlicher, J.; Becker, U. *Chemical Geology* **2005**, *215*, 499-516.

- (25) Adobes-Vidal, M.; Maddar, F. M.; Momotenko, D.; Hughes, L. P.; Wren, S. A. C.; Poloni, L. N.; Ward, M. D.; Unwin, P. R. *Crystal Growth & Design* **2016**.
- (26) Macpherson, J. V.; Unwin, P. R. *The Journal of Physical Chemistry* **1994**, *98*, 1704-1713.
- (27) Perry, A. R.; Lazenby, R. A.; Adobes-Vidal, M.; Peruffo, M.; McKelvey, K.; Snowden, M. E.; Unwin, P. R. *CrystEngComm* **2015**, *17*, 7835-7843.
- (28) Kinnear, S. L.; McKelvey, K.; Snowden, M. E.; Peruffo, M.; Colburn, A. W.; Unwin, P. R. *Langmuir* **2013**, *29*, 15565-15572.
- (29) Vega, D. R.; Polla, G.; Martinez, A.; Mendioroz, E.; Reinoso, M. *International Journal of Pharmaceutics* **2007**, *328*, 112-118.
- (30) Abu-Diak, O. A.; Jones, D. S.; Andrews, G. P. *Journal of Pharmaceutical Sciences* **2012**, *101*, 200-213.
- (31) Andrews, G. P.; AbuDiak, O. A.; Jones, D. S. *Journal of Pharmaceutical Sciences* **2010**, *99*, 1322-1335.
- (32) Dolomanov, O. V.; Bourhis, L. J.; Gildea, R. J.; Howard, J. A. K.; Puschmann, H. *Journal of Applied Crystallography* **2009**, *42*, 339-341.
- (33) Sheldrick, G. *Acta Crystallographica Section A* **2008**, *64*, 112-122.
- (34) Sheldrick, G. *Acta Crystallographica Section C* **2015**, *71*, 3-8.
- (35) Prasad, K. V. R.; Ristic, R. I.; Sheen, D. B.; Sherwood, J. N. *International Journal of Pharmaceutics* **2002**, *238*, 29-41.
- (36) Kaemmer, S. B. *Bruker application note. Bruker Nano Inc., Santa Barbara, CA* **2011**.
- (37) Gasperino, D.; Yeckel, A.; Olmsted, B. K.; Ward, M. D.; Derby, J. J. *Langmuir* **2006**, *22*, 6578-6586.

- (38) Peruffo, M.; Mbogoro, M. M.; Adobes-Vidal, M.; Unwin, P. R. *The Journal of Physical Chemistry C* **2016**, *120*, 12100-12112.
- (39) Adobes-Vidal, M.; Shtukenberg, A. G.; Ward, M. D.; Unwin, P. R. *Crystal Growth & Design* **2017**, *17*, 1766-1774.
- (40) Burt, D. P.; Wilson, N. R.; Janus, U.; Macpherson, J. V.; Unwin, P. R. *Langmuir* **2008**, *24*, 12867-12876.
- (41) Christoffersen, J.; Christoffersen, M. R. *Journal of Crystal Growth* **1988**, *87*, 41-50.
- (42) Jiang, H. B.; Cuan, Q.; Wen, C. Z.; Xing, J.; Wu, D.; Gong, X.-Q.; Li, C.; Yang, H. G. *Angewandte Chemie International Edition* **2011**, *50*, 3764-3768.
- (43) Burt, H. M.; Mitchell, A. G. *International Journal of Pharmaceutics* **1981**, *9*, 137-152.
- (44) Macrae, C. F.; Edgington, P. R.; McCabe, P.; Pidcock, E.; Shields, G. P.; Taylor, R.; Towler, M.; Streek, J. v. d. *Journal of Applied Crystallography* **2006**, *39*, 453-457.
- (45) Ward, M. D. *Chemical Reviews* **2001**, *101*, 1697-1726.
- (46) Ren, F.; Jing, Q.; Tang, Y.; Shen, Y.; Chen, J.; Gao, F.; Cui, J. *Drug development and industrial pharmacy* **2006**, *32*, 967-972.

Chapter 4

Functional Multimicroscopy Approach to Assess the Dissolution Performance of Amorphous Solid Dispersions (ASDs)

Innovative drug formulations are needed to enhance the solubility and bioavailability of poorly soluble active pharmaceutical ingredients (APIs), among which amorphous solid dispersions (ASDs) are of increasing interest. However, rapid dissolution from the amorphous state poses the risk of competing crystallization from the resulting supersaturated solution state. This study considers the physicochemical processes that take place during the dissolution of ASDs containing the poorly water-soluble API felodipine and the water-soluble polymer, copovidone using a range of techniques, some of which have not been applied to this type of problem previously. We have compared two different loadings, 15 % and 50 % felodipine by weight. A novel electrochemical cell approach is described to induce and monitor API release just after immediate contact with water. These studies indicate rapid dissolution fluxes for both loadings, but with higher fluxes for the higher loading. These observations are complemented with simple optical microscopy, in situ atomic force microscopy and Raman spectroscopy to monitor changes in the solid over much larger times. This has revealed important phase transformation (crystallization) processes that could compete with API release and limit the effectiveness of ASDs.

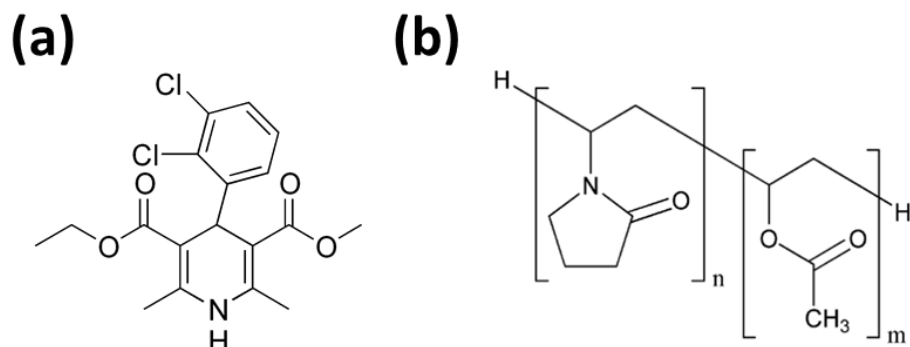
4.1. Introduction

Many newly developed drugs with pharmacological activity are characterised by poor aqueous solubility and dissolution profiles.^{1,2} There is thus increasing interest in innovative formulations to enhance solubility and bioavailability, including the use of nanocrystals, nanoemulsions, polymer micelles and solid dispersions.³⁻⁸ This contribution concerns solid dispersion formulations,^{7,9,10} whereby a poorly water soluble drug is mixed with a water-soluble polymer carrier, commonly via spray drying or hot melt extrusion.^{11,12} The drug within the dispersion is in the amorphous form, giving enhanced solubility and dissolution rates than the corresponding crystalline form. Polymer carriers are expected to provide significant stability of the amorphous state of the drug (with respect to crystalline forms) in both the solid state and in the resulting supersaturated solution generated by dissolution.^{13,14} However, the high free energy of the amorphous form means that reversion to the most stable form via recrystallization may occur and has to be assessed.

Despite their usefulness in improving dissolution rates, marketed products based on this strategy are few. The state of the drug in a solid dispersion (i.e. balance between the amorphous/crystalline states) is often difficult to characterize due to limited available techniques.^{15,16} In addition, there is a lack of clear understanding of the *in vivo* and *in vitro* behaviour of ASDs during dissolution. It has been highlighted that the mechanism of drug release can be either polymer controlled or drug controlled,¹⁷ and the extent of either pathway is influenced by the physicochemical properties of both the active pharmaceutical ingredient (API) and the polymer, as well as the ratio between the two. Previously, it has been shown that crystallization of the drug in either the solid state or from a supersaturated state in solution (with respect to a crystalline form) is critical in understanding the overall dissolution performance.^{18,19} Additionally, the formation of nano- and micro- particles in the solid state or during dissolution has been shown to contribute to the dissolution mechanism.²⁰

The addition of water to ASDs has many phenomenological effects, particularly when the API (drug) is poorly water-soluble and the polymer is hydrophilic, as is usually the case.²¹⁻²³ Water addition may drive the system towards polymer-drug phase separation creating two domains; one rich in polymer and the other rich in drug.²⁴⁻²⁶ The resulting low polymer content in the drug rich domain can lead to phase transformation causing crystallization to occur, which would hinder the overall dissolution performance. This known phenomenon of amorphous-amorphous phase separation is not fully understood as is affected by many variables including drug-polymer interaction strength, drug and polymer properties, as well as the drug-polymer ratio.^{13,25,27,28}

Conventional methods for studying API release do not readily probe phase transitions that might occur during dissolution and so the development of more incisive techniques could be valuable in enhancing mechanistic information. In this study, the ASD of interest comprises felodipine drug in a water-soluble polymer, copovidone VA64 (Scheme 1). Felodipine is a calcium-channel blocking agent, widely used for treatment of hypertension.²⁹ In previous studies, the dissolution performance of ASDs containing felodipine has been shown to be highly dependent upon drug loading^{13,30-34} and so in this study two different drug loadings were investigated, 15 % and 50 %. With a combination of *in situ* atomic force microscopy (AFM), Raman spectroscopy analysis and an electrochemical cell probing technique, it was possible to observe key features in the mechanism and kinetics of drug dissolution in aqueous solution, with results that highlight the importance of drug loading on the dissolution of ASDs. An advantage of this approach is that we are able to follow crystallization at a much smaller length scale, and in some cases shorter timescale, than has been possible previously.



Scheme 4.1. Molecular structures of (a) felodipine and (b) copovidone.

4.2. Experimental Section

4.2.1. Solutions and Sample Preparation

All chemicals were used as received. Aqueous solutions were prepared using high purity water (Purite, Select HP) with a resistivity of 18.2 MΩ cm at 25 °C. Polymeric dispersions of felodipine were supplied by AstraZeneca.

4.2.2. Optical Microscopy

Optical observations utilized a 20X objective lens on a Leica DM4000 M compound microscope.

4.2.3. *In situ* Atomic Force Microscopy

Dissolution studies were performed in unstirred solution directly in a petri dish (Willco Well) containing the polymeric dispersions of interest fixed to the surface by double sided tape, using a Bioscope Catalyst microscope with a Nanoscope V controller (Veeco). AFM images were acquired in *ScanAsyst* mode using silicon-tips on a silicon nitride lever with a spring constant of 0.35 Nm⁻¹ according to the manufacturer (SNL-10, Bruker).

4.2.4. Raman Spectroscopy

In situ Raman investigations were performed on a Renishaw inVia Reflex Raman Microscope fitted with a Charge Coupled Device (CCD) detector with a near-IR (633 nm) laser. A 20X objective lens was used for images presented herein.

4.2.5. Quad-Probe Fabrication

Quad-probes (pipettes containing 4 channels) were fabricated from quartz quadruple-barrelled capillaries (MBT-015-062-4Q, Friedrich & Dimmock, Inc.) pulled to a sharp point by a laser puller (P-2000, Sutter Instruments) as described in chapter 2 and in detail elsewhere.³⁵ After pulling, the end of each channel was ca. 400 nm across. Two of the channels were filled with carbon by pyrolysis of butane gas passed through these channels simultaneously as described previously.³⁵ The probes were then further optimized by focused ion beam (FIB) polishing to achieve a final probe size of *ca.* 2 μm diameter across. FIB-SEM (JEOL 4500, JEOL) at an accelerating voltage of 5 kV with gallium ions was used. The empty channels were each filled with 100 mM KCl solution together with a AgCl-Ag wire to act as a quasi-reference counter electrode (QRCE). A home built scanning electrochemical cell microscope with home built current follower was used as described elsewhere.³⁵

4.2.6. Electrochemistry

Some control electrochemical measurements were made to determine whether felodipine could be detected electrochemically. Measurements utilised 5 mm glassy carbon (GC) electrode. Gamry Instruments rotating electrode equipped with motor controller was used that enabled a precise mass transport rate to be applied. A 3 electrode set-up was employed with a Pt counter electrode and Ag/AgCl wire reference electrode. Measurements used a CHI Instruments potentiostat controlled by a PC.

4.3. Results and Discussion

4.3.1. Optical Microscopy

The behaviour of polymeric matrices of copovidone containing different loadings of felodipine 15 and 50 % w/w, were first monitored immediately after adding ultrapure water (2 mL) using optical microscopy. Figure 4.1, shows images of the two ASD formulations, as solids, before and after contact with water. Figure 4.1 (a) (i) shows an optical image taken before the addition of water to the formulation containing 15 % felodipine and Figure 4.1 (a) (ii) is taken after water contact. Here, we observe the formation of a gel-like swollen layer, as a consequence of the plasticization of the polymer by the water.³⁶ This is due to the relatively high content of polymer in the formulation, such that the characteristics are dominated by the hydration of the polymer to form a gel. In stark contrast, the formulation containing 50 % felodipine, illustrated in Figure 4.1 (b) (i) and (b) (ii) showed little change upon water contact (on the resolution of optical microscopy). These brief observations highlight distinct differences in the behaviour of these formulations, which we now investigate with different type of advanced microscopy.

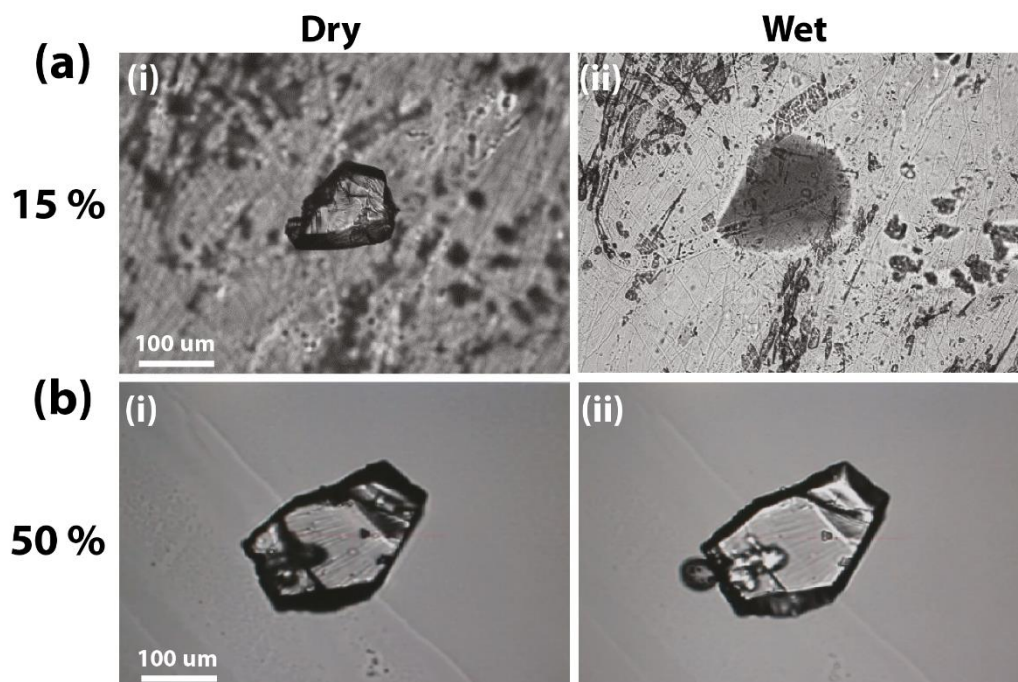


Figure 4.1. Optical microscope images taken before and after the addition of water to the two formulations of amorphous solid dispersions. (a) 15 % felodipine ASD and (b) 50 % felodipine ASD (i) represents dry sample and (ii) when in contact with water.

4.3.2. Topographical Changes: *In situ* Atomic Force Microscopy Analysis

For further insight into the phase transformations taking place upon water contact with the ASDs, we turned to *in situ* AFM. Due to the polymer plasticization effect seen with the 15 % felodipine ASD, AFM measurements proved difficult. However, it was possible to monitor the aqueous dissolution of the 50 % felodipine ASD over time, shown in Figure 4.2. Examining Figure 4.2, as the dissolution process proceeded, AFM images show the formation of nanoparticles, a few 10s nm in size, on the surface of the solid ASD on a fairly long timescale of several hours. As discussed in the next section, this behaviour in the solid state correlates with the crystallization of the felodipine in the solid state on this time scale.

4.3.3. Raman Spectroscopy

In situ Raman studies were carried out on the two ASDs (15 and 50 % w/w). Figure 4.3 (i) shows the evolution of the Raman spectra for the two ASDs after contact with water. For comparison, the Raman spectrum of crystalline felodipine was acquired in air and is represented by the red trace. It is characterized by sharp peaks at 1206 cm^{-1} , 1484 cm^{-1} and at 1650 cm^{-1} . Comparison with the dry ASD shows that there is a characteristic copovidone peak at 1431 cm^{-1} . Figure 4.3 (a) (i) shows the Raman spectra of the 15 % felodipine ASD as a function of time. Over time, there is a reduction in intensity of the copovidone peak at 1431 cm^{-1} , as well as the felodipine peaks at 1650 cm^{-1} and 1484 cm^{-1} as shown in Figure 4.3 (a) (ii) and (iii). This agrees with the Raman studies of Tres *et al.* for a 5 % felodipine extrudate,³⁷ suggesting that felodipine and copovidone dissolve at a similar rate, as a single entity rather than as two separate components. However, the spectrum recoded after 24 hours shows a decrease in intensity of the felodipine peak at 1484 cm^{-1} relative to the copovidone peak at 1431 cm^{-1} signifying some recrystallization of the amorphous felodipine. In addition, characteristic felodipine peaks at 1650 cm^{-1} and 1206 cm^{-1} intensify at this time point.³⁷

For comparison, Figure 4.3 (b) (i) shows the Raman spectra of the 50 % ASD during dissolution. After four hours, the intensity of the copovidone peak at 1431 cm^{-1} decreases as the felodipine peak at 1484 cm^{-1} increases slightly, as represented in Figure 4.3 (b) (ii). This effect is seen even more after long times (42 hours), in which felodipine peak at 1650 cm^{-1} also increases in intensity (Figure 4.3 (b) (iii)). As a consequence, amorphous felodipine material in the solid state recrystallize due to the dissolution of copovidone. After 42 hours, the Raman spectrum of the dispersion resembles the crystalline felodipine spectrum, confirming the recrystallization of the initial amorphous felodipine.

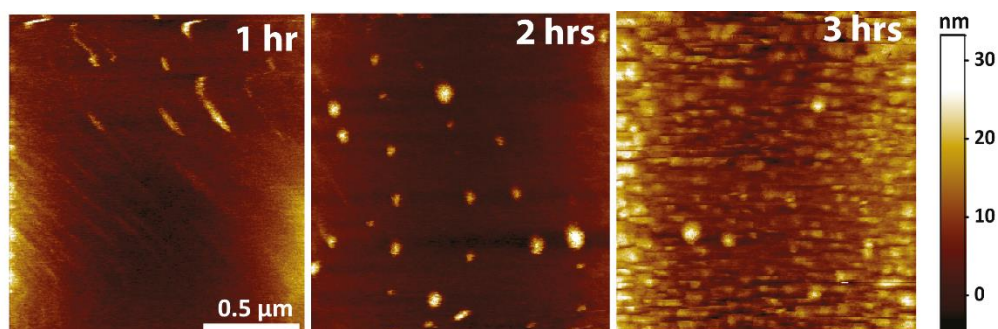


Figure 4.2. Series of *in situ* AFM images over time showing the recrystallization of felodipine during the aqueous dissolution of 50% felodipine ASD.

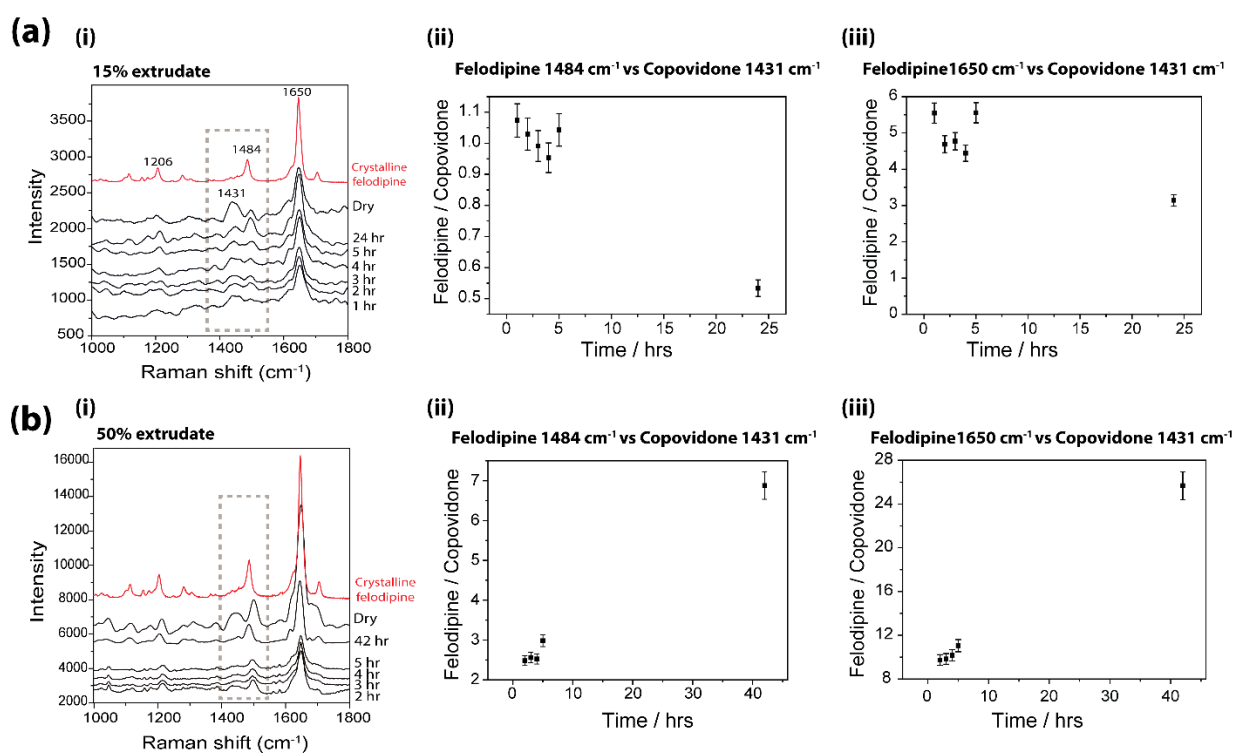


Figure 4.3. Raman spectra relative to the aqueous dissolution of: (a) (i) 15% felodipine and (b) (i) 50% felodipine ASD over time. Spectrum in red highlights Raman signal of crystalline felodipine for comparison. (b) (ii) (iii) show the peak height intensity of amorphous felodipine and copovidone as a function of time.

4.3.4. *In situ* Electrochemical Monitoring of Initial Dissolution

Hitherto, we have focused on the analysis of the solid ASDs during dissolution, but we are ultimately interested in the release of the soluble drug. We now present electrochemical techniques to monitor initial dissolution from the ASD phase. Firstly, to examine the electroactivity of felodipine, bulk electrochemical measurements were performed. Rotating disk electrode voltammetry was recorded on glassy carbon in solution containing known concentration of felodipine (3 μM) in 100 mM KCl with representative cyclic voltammogram (CV) shown in Figure 4.4. A diffusion-limited current response was obtained using glassy carbon at electrode rotation speed of 2000 rpm showing the clear electro-oxidation of felodipine. We then moved onto the use of the carbon quad probes. To test the electrode ($\sim 10\ \mu\text{m}$ diameter), the one-electron electro-oxidation of 1 mM (ferrocenylmethyl) trimethyl ammonium (FcTMA^+) was performed. Figure 4.4 (b) shows the acquired CV resulting in a steady-state current response resembling the behaviour of ultramicroelectrodes (UMEs)^{38,39} and signifying the good functionality of this electrode. Thus, the carbon quad probe was used to detect the electro-oxidation of felodipine. Figure 4.4 (c) show a CV run at $100\ \text{mVs}^{-1}$ in saturated solution of felodipine ($\sim 49\ \mu\text{M}$)⁴⁰. A clear limiting current is observed. In order to confirm that this is the correct electrode response, we compared our results to the theoretical current ($\sim 0.045\ \text{nA}$) where the diffusion coefficient of felodipine molecules in aqueous solution ($D = 4.15 \times 10^{-6}\ \text{cm}^2\ \text{s}^{-1}$) was calculated using the Wilke-Chang equation.⁴¹ This provides diffusivities with an absolute error no bigger than 11%. Accordingly, the current magnitude achieved herein ($\sim 0.06\ \text{nA}$) is within good proximity.

Theoretical current was calculated from the acquired data shown in Figure 4.4. Firstly the Levich equation was used to calculate the number of electrons transferred during the oxidation of felodipine using RDE. Here, i_{lim} is the limiting current, n is the number of electrons transferred, F is the Faraday constant ($96485\ \text{Cmol}^{-1}$), A is the electrode area (cm^2), D is the diffusion coefficient ($\text{cm}^2\ \text{s}^{-1}$), ω is the angular rotation

rate of the electrode (rads^{-1}), ν is the kinematic viscosity (cm^2s^{-1}), C is the concentration (molcm^{-3}).

$$i_{lim} = 1.554nFAD^{\frac{2}{3}}\omega^{\frac{1}{2}}\nu^{-\frac{1}{6}}[C] \quad (1)$$

Using the limiting current achieved of the oxidation of 3 μM felodipine on 5 mm glassy carbon (Figure 4.4 (i)), n was calculated:

$$n = \frac{1.8 \times 10^{-7}}{1.554 \times 96485 \times 0.196 \times (2.58 \times 10^{-4}) \times 5.77 \times 2.15 \times (3 \times 10^{-9})}$$

$$n = 0.64 \sim 1 \text{ electron}$$

Following on, the oxidation of 1 mM FcTMA^+ was carried out on carbon quad barrel (Figure 4.4 (ii)). Using equation (2) the radius, a of the carbon quad electrode was calculated:

$$i = 4nFDaC \quad (2)$$

$$a = \frac{1.4 \times 10^{-9}}{4 \times 1 \times 96485 \times (6.3 \times 10^{-6}) \times (1 \times 10^{-6})}$$

$$a = 5.76 \times 10^{-4} \text{ cm} \sim 5.76 \mu\text{m}$$

The rate constant, k was calculated using equation (3) and the theoretical current was achieved using equation (4):

$$4a = k \quad (3)$$

$$i = knFDc \quad (4)$$

$$(2.3 \times 10^{-3}) \times 1 \times 96485 \times (4.149 \times 10^{-6}) \times (4.9 \times 10^{-8}) = 0.045 \text{ nA}$$

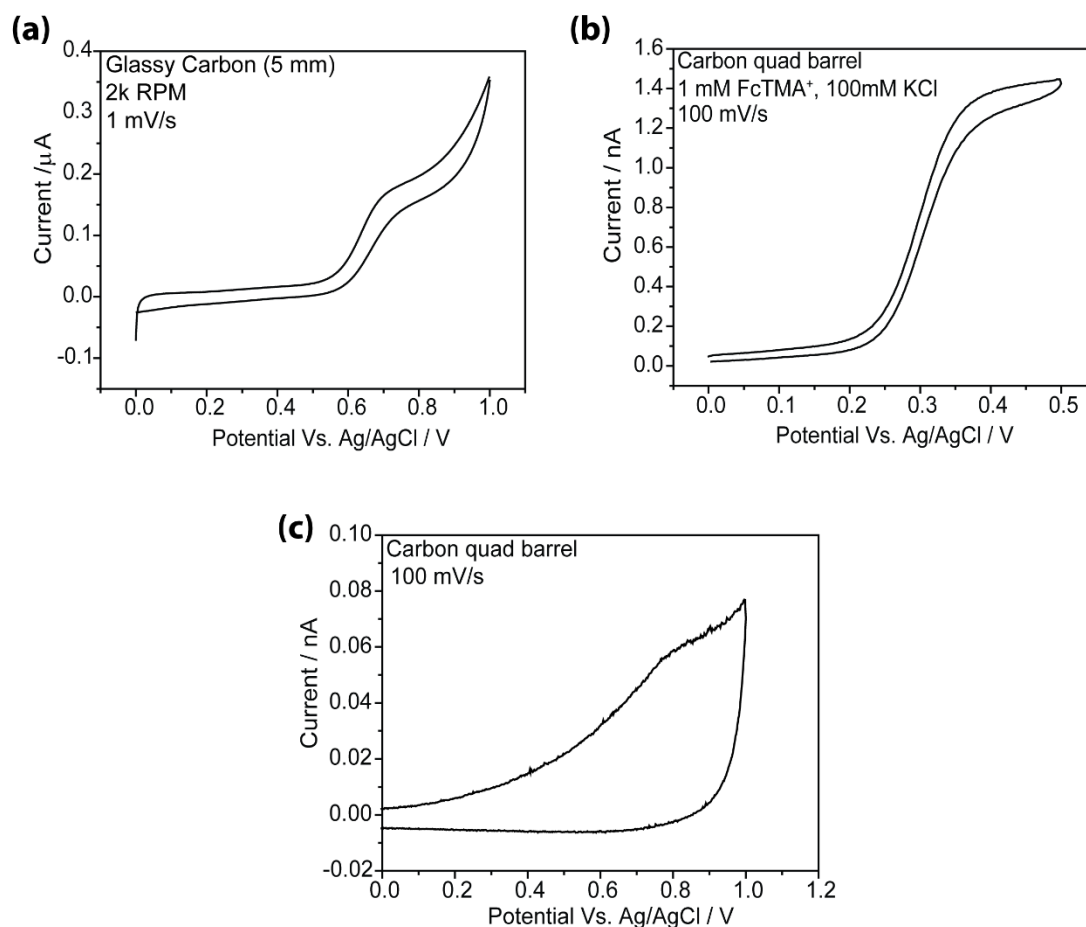


Figure 4.4. (a) Rotating disk electrode voltammogram run on glassy carbon electrode of 3 μM felodipine solution containing 100 mM KCl. (b) Shows the current response of a carbon quad probe ($\sim 10 \mu\text{m}$ diameter) in 1 mM FcTMA⁺ containing 100 mM KCl. (c) CV of saturated felodipine solution containing 100 mM KCl at 100 mVs⁻¹.

The application of UMEs to study dissolution is established.⁴²⁻⁴⁴ By positioning a UME close to the surface of interest crystal dissolution can be induced and monitored. Here, similarly, we present the use of a droplet-based electrochemical technique that uses a liquid droplet formed at the end of quad probe pipette with open fluid channels and integrated carbon electrodes, to create an electrochemical meniscus cell on the sample surface.⁴⁵⁻⁴⁷ At a potential for the diffusion-limited detection of felodipine, the

current recorded at the carbon electrodes (sink conditions) is proportional to the dissolution flux which can be used to measure the rate of release of material from a surface.

As mentioned in the experimental section, the two open barrels are filled with electrolyte (100 mM KCl) and equipped with QRCEs (Ag/AgCl wires) and the other two were carbon working electrodes.³⁵ The basic approach to the use of a quad probe to locally measure dissolution of the polymeric dispersions is shown in the cartoon illustration in Figure 4.5 (a). The probe was brought vertically towards the substrate to make meniscus contact with a fresh solid surface to form a thin layer electrochemical cell between the probe and surface (typically 1 μm thickness or less).³⁵ Figure 4.5 (b) (i) shows, a scanning electron micrograph of the end of a typical probe used to give an idea of scale, and an optical side view of the probe positioned close to the sample surface is shown in Figure 4.5 (b) (ii).

Figure 4.5 (c) (i) and (ii) show typical voltammograms for the detection of felodipine from the two ASDs. The lower drug loading ASD (15 % felodipine) resulted in a lower currents compared to the higher drug loading (50 % felodipine), as much more felodipine is detected due to induced dissolution. Note that, the current values achieved herein are much higher than would be expected for the aqueous solubility concentration of felodipine ($\sim 49 \mu\text{M}$) in a bulk solution. By sweeping the potential of the carbon very close to the surface (i.e. under very strong sink conditions) we induce dissolution resulting in high current values. These observations indicate that ASD formulations indeed provide a technology for rapid drug release.

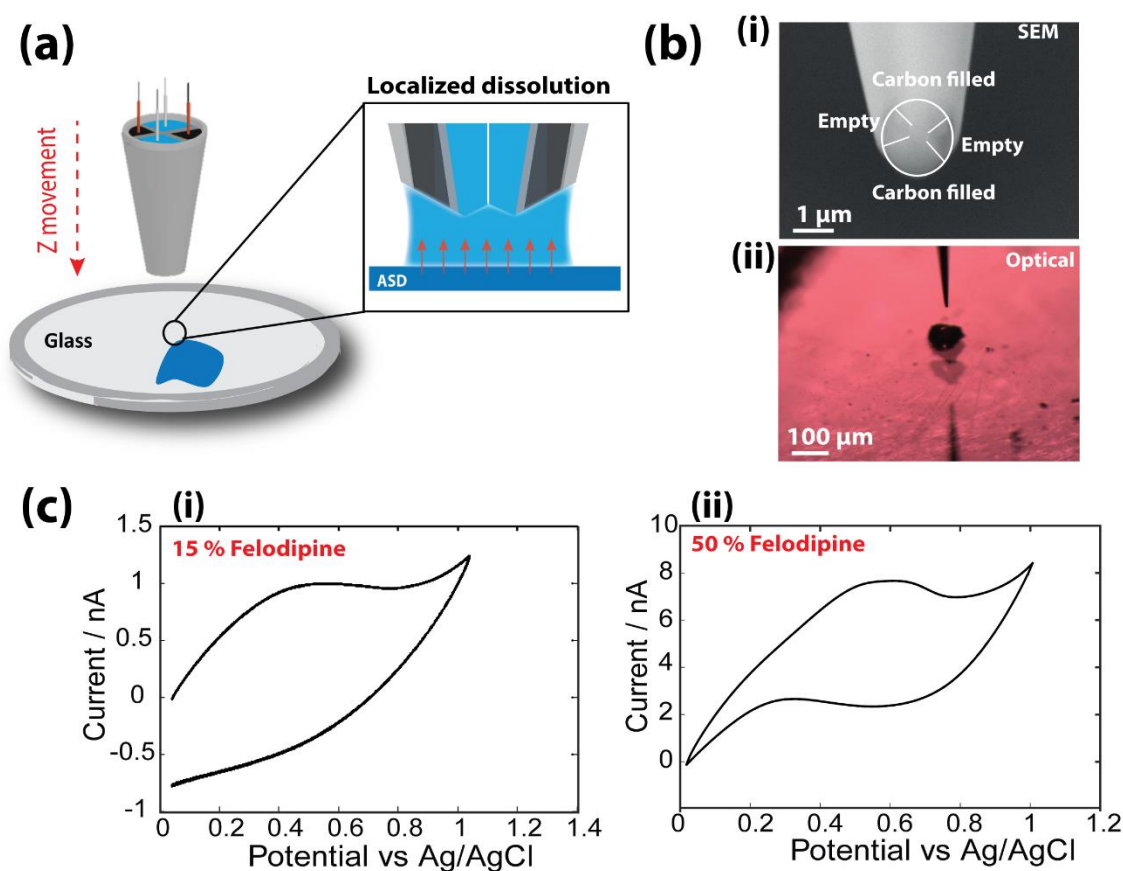


Figure 4.5. (a) Schematic of the electrochemical quad-probe. The probe moves down so that the meniscus is in contact with the amorphous solid surface. Carbon electrodes detect the release of felodipine upon water contact and the QRCEs in the open barrels in the probe act as the reference/counter electrodes. (b) (i) SEM micrograph of the end of a typical quad-probe showing carbon electrodes (top and bottom) and open barrels (left and right). (ii) Optical microscope image of the probe tip positioned above a single solid before landing. (c) (i) Current-potential response recorded at the quad-probe during approach and after the meniscus came into contact with the surface of the ASD containing (a) 15 % felodipine and (b) 50 % felodipine.

4.4. Conclusions

We have demonstrated the use of a multi-microscopy approach to locally probe the dissolution process of amorphous solid dispersion in real time. With Raman spectroscopy of the ASD, we were able to track the dissolution of both the API and polymer simultaneously. For both ASDs, recrystallization of felodipine was observed but it was much more noticeable for the 50 % ASD where the Raman signal at longer times showed strong crystalline felodipine characteristics. This was further shown by *in situ* AFM studies, where changes in topography were tracked over time and formation of particles on the surface was observed. In addition, at much shorter timescales, carbon quad probes were used to induce the dissolution of ASDs, proving that rapid release of felodipine occurs under steady sink condition.

These brief studies demonstrate the importance of drug/polymer ratio in controlling the dissolution behaviour in ASD formulations. We have also shown the value of microscopy approaches, some of which are not widely used in pharmaceutical science, but offer considerable potential to improve understanding of complex dissolution processes.

4.5. References

- (1) Ku, M. S. *The AAPS journal* **2008**, *10*, 208-212.
- (2) Di, L.; Fish, P. V.; Mano, T. *Drug Discovery Today* **2012**, *17*, 486-495.
- (3) Pouton, C. W. *European Journal of Pharmaceutical Sciences* **2006**, *29*, 278-287.
- (4) Lu, Y.; Park, K. *International Journal of Pharmaceutics* **2013**, *453*, 198-214.
- (5) Kesisoglou, F.; Panmai, S.; Wu, Y. *Advanced Drug Delivery Reviews* **2007**, *59*, 631-644.
- (6) Chen, H.; Khemtong, C.; Yang, X.; Chang, X.; Gao, J. *Drug discovery today* **2011**, *16*, 354-360.

- (7) Leuner, C.; Dressman, J. *European Journal of Pharmaceutics and Biopharmaceutics* **2000**, *50*, 47-60.
- (8) Babu, N. J.; Nangia, A. *Crystal Growth & Design* **2011**, *11*, 2662-2679.
- (9) Goldberg, A. H.; Gibaldi, M.; Kanig, J. L. *Journal of pharmaceutical sciences* **1966**, *55*, 482-487.
- (10) Vasconcelos, T.; Sarmiento, B.; Costa, P. *Drug Discovery Today* **2007**, *12*, 1068-1075.
- (11) Hülsmann, S.; Backensfeld, T.; Keitel, S.; Bodmeier, R. *European Journal of Pharmaceutics and Biopharmaceutics* **2000**, *49*, 237-242.
- (12) Breitenbach, J. *European Journal of Pharmaceutics and Biopharmaceutics* **2002**, *54*, 107-117.
- (13) Konno, H.; Handa, T.; Alonzo, D. E.; Taylor, L. S. *European Journal of Pharmaceutics and Biopharmaceutics* **2008**, *70*, 493-499.
- (14) Liu, H.; Taylor, L. S.; Edgar, K. J. *Polymer* **2015**, *77*, 399-415.
- (15) Yu, L. *Advanced Drug Delivery Reviews* **2001**, *48*, 27-42.
- (16) Chow, K.; Tong, H. H. Y.; Lum, S.; Chow, A. H. L. *Journal of Pharmaceutical Sciences*, *97*, 2855-2877.
- (17) Craig, D. Q. M. *International Journal of Pharmaceutics* **2002**, *231*, 131-144.
- (18) Alonzo, D. E.; Zhang, G. G.; Zhou, D.; Gao, Y.; Taylor, L. S. *Pharmaceutical Research* **2010**, *27*, 608-618.
- (19) Langham, Z. A.; Booth, J.; Hughes, L. P.; Reynolds, G. K.; Wren, S. A. C. *Journal of Pharmaceutical Sciences*, *101*, 2798-2810.

- (20) Tho, I.; Liepold, B.; Rosenberg, J.; Maegerlein, M.; Brandl, M.; Fricker, G. *European Journal of Pharmaceutical Sciences* **2010**, *40*, 25-32.
- (21) Kawabata, Y.; Wada, K.; Nakatani, M.; Yamada, S.; Onoue, S. *International Journal of Pharmaceutics* **2011**, *420*, 1-10.
- (22) Frank, K. J.; Westedt, U.; Rosenblatt, K. M.; Hölig, P.; Rosenberg, J.; Mägerlein, M.; Fricker, G.; Brandl, M. *Journal of Pharmaceutical Sciences* **2014**, *103*, 1779-1786.
- (23) Li, B.; Konecke, S.; Harich, K.; Wegiel, L.; Taylor, L. S.; Edgar, K. J. *Carbohydr. Polym.* **2013**, *92*, 2033-2040.
- (24) Konno, H.; Taylor, L. S. *Pharmaceutical Research* **2008**, *25*, 969-978.
- (25) Rumondor, A. C. F.; Marsac, P. J.; Stanford, L. A.; Taylor, L. S. *Molecular Pharmaceutics* **2009**, *6*, 1492-1505.
- (26) Marsac, P. J.; Rumondor, A. C. F.; Nivens, D. E.; Kestur, U. S.; Stanciu, L.; Taylor, L. S. *Journal of Pharmaceutical Sciences*, *99*, 169-185.
- (27) Konno, H.; Taylor, L. S. *Journal of Pharmaceutical Sciences*, *95*, 2692-2705.
- (28) Rumondor, A. C. F.; Wikström, H.; Van Eerdenbrugh, B.; Taylor, L. S. *AAPS PharmSciTech* **2011**, *12*, 1209-1219.
- (29) Surov, A. O.; Solanko, K. A.; Bond, A. D.; Bauer-Brandl, A.; Perlovich, G. L. *CrystEngComm* **2013**, *15*, 6054-6061.
- (30) Marsac, P. J.; Konno, H.; Rumondor, A. C. F.; Taylor, L. S. *Pharmaceutical Research* **2008**, *25*, 647-656.
- (31) Won, D.-H.; Kim, M.-S.; Lee, S.; Park, J.-S.; Hwang, S.-J. *International Journal of Pharmaceutics* **2005**, *301*, 199-208.

- (32) Karavas, E.; Ktistis, G.; Xenakis, A.; Georgarakis, E. *Drug Development and Industrial Pharmacy* **2005**, *31*, 473-489.
- (33) Konno, H.; Taylor, L. S. *Journal of Pharmaceutical Sciences* **2006**, *95*, 2692-2705.
- (34) Song, Y.; Wang, L.; Yang, P.; Wenslow, R. M., Jr.; Tan, B.; Zhang, H.; Deng, Z. *Journal of Pharmaceutical Sciences*, *102*, 1915-1923.
- (35) Paulose Nadappuram, B.; McKelvey, K.; Byers, J. C.; Güell, A. G.; Colburn, A. W.; Lazenby, R. A.; Unwin, P. R. *Analytical Chemistry* **2015**, *87*, 3566-3573.
- (36) Miller-Chou, B. A.; Koenig, J. L. *Progress in Polymer Science* **2003**, *28*, 1223-1270.
- (37) Tres, F.; Treacher, K.; Booth, J.; Hughes, L. P.; Wren, S. A. C.; Aylott, J. W.; Burley, J. C. *Journal of Controlled Release* **2014**, *188*, 53-60.
- (38) Mirkin, M. V.; Bard, A. J. *Analytical Chemistry* **1992**, *64*, 2293-2302.
- (39) Mirkin, M. V.; Richards, T. C.; Bard, A. J. *The Journal of Physical Chemistry* **1993**, *97*, 7672-7677.
- (40) Bhole, P. G.; Patil, V. R. *Enhancement of water solubility of felodipine by preparing solid dispersion using poly-ethylene glycol 6000 and poly-vinyl alcohol*, 2009; Vol. 3.
- (41) Wilke, C. R.; Chang, P. *AIChE J.* **1955**, *1*, 264-270.
- (42) Macpherson, J. V.; Unwin, P. R. *J. Chem. Soc., Faraday Trans.* **1993**, *89*, 1883-1884.
- (43) Macpherson, J. V.; Unwin, P. R. *The Journal of Physical Chemistry* **1994**, *98*, 1704-1713.

(44) Macpherson, J. V.; Unwin, P. R. *The Journal of Physical Chemistry* **1995**, 99, 3338-3351.

(45) Ebejer, N.; Schnippering, M.; Colburn, A. W.; Edwards, M. A.; Unwin, P. R. *Analytical Chemistry* **2010**, 82, 9141-9145.

(46) Kinnear, S. L.; McKelvey, K. M.; Snowden, M. E.; Peruffo, M.; Colburn, A. W.; Unwin, P. R. *Langmuir* **2013**, 29, 15565-15572.

(47) Snowden, M. E.; Güell, A. G.; Lai, S. C. S.; McKelvey, K.; Ebejer, N.; O'Connell, M. A.; Colburn, A. W.; Unwin, P. R. *Analytical Chemistry* **2012**, 84, 2483-2491.

Chapter 5

Confined Crystallization of Organic Materials in Nanopipettes: Tracking the Early Stages of Crystal Growth and Making Seeds for Unusual Polymorphs

*Monitoring crystallization in real time at the nanoscale can provide valuable new insights into the nucleation process. Herein, the application of nanopipettes as nanoreactors to study the nucleation of organic materials (pharmaceutical crystals) is demonstrated, using bicalutamide (BIC), an active pharmaceutical ingredient of the prostate cancer drug CASODEX[®], as a model. Crystallization is achieved using a nanoscale antisolvent system, whereby a nanopipette containing an aqueous inert salt solution is brought into contact with a dimethyl sulfoxide (DMSO) solution containing soluble BIC and the same inert salt (at the same concentration). Crystallization is driven and controlled by a combination of the applied bias between an electrode in the nanopipette and one in the bulk DMSO phase and mixing of the two solvents at the mouth of the nanopipette. Crystallization at the tip of the nanopipette causes transient blockages, as BIC particles form and translocate at the end of the nanopipette opening. At low inert electrolyte concentration, the current-time signature is highly stochastic and comprises a sequence of current pulse increases and decreases, which could either indicate nucleation-dissolution during phase transformation, and/or be due to the particles formed being charged. Particles produced in this way can be used as seeds for crystal growth and Raman spectroscopy analysis of the crystals produced indicates the formation of Form II BIC which is rarely formed. Thus, in addition to monitoring nucleation, nanopipettes can serve as reactors to synthesize organic crystals with polymorphs that are not typically found. Finite element method modeling provides valuable insight on the solvent mixing process and effect of applied bias, and helps to explain some of the observations. This work is published in *Crystal Growth & Design*.*

5.1. Introduction

Crystallization at the nanoscale, in a confined environment, can have a significant impact on the properties of the emerging crystal structure, including the formation of unusual metastable polymorphs.¹

When compounds are capable of exhibiting polymorphism, the free energy profiles of the different polymorphs will determine the final crystal structure, shown in Figure 5.1. As polymorphs have different crystal structures, their specific surface energies, volume free energies, and crystal morphologies will differ. Accordingly, each polymorph will have distinct ΔG and critical nucleus size. Figure 5.1 illustrates free energy profiles in which polymorph B is more stable in bulk form but polymorph A is more stable at the critical size and slightly beyond. Thus, suggesting that crystallization in confined environments with dimensions at or near the critical size could lead to stabilization of metastable polymorphs (i.e. size-dependent polymorphism). As a result, confinement provides an alternative method for controlling polymorphism.

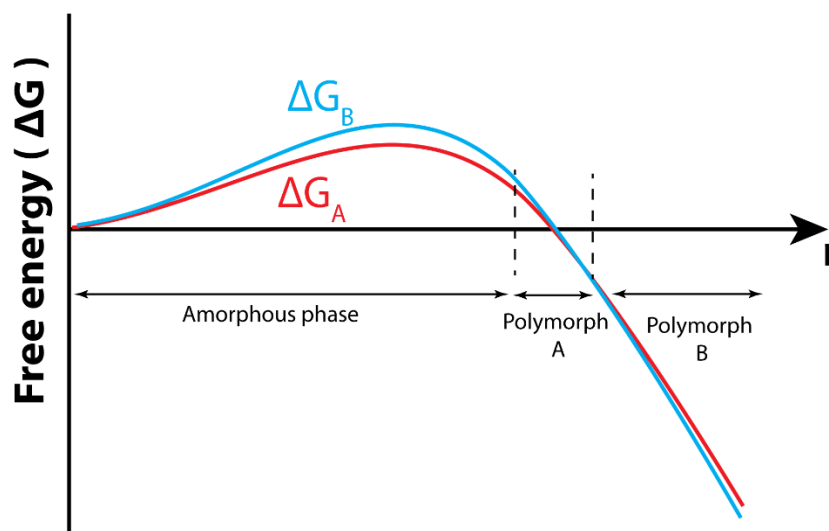


Figure 5.1. Schematic representation of the free energy profiles for two competing nuclei corresponding to polymorphs A and B, over a range of sizes.

Herein, nanopipettes are shown to provide a powerful methodology for detecting the nucleation and growth of seeds of pharmaceutical crystals, using bicalutamide (BIC) (shown in scheme 5.1), as an exemplar system. BIC is an active pharmaceutical ingredient (API) in AstraZeneca's prostate cancer product CASODEX[®], belonging to class II of the biopharmaceutics classification system (BCS) (low solubility and high permeability).^{2, 3} It has received considerable attention as a model for class II drugs.⁴⁻⁶ Crystal polymorph control is an important aspect of drug formulation, to ensure bioavailability and stability of the drug product. Unusual polymorphs may provide a route to enhancing solubility of class II biopharmaceutics,^{1, 7} and an aspect of this paper is the creation of polymorph II of BIC rather than the more stable polymorph I that is usually formed.

Nanopipettes and solid state nanopores, have become established as powerful tools in the detection and manipulation of single entities (nanoparticles and macromolecules) through the use of resistive pulse principles.⁸⁻¹⁵ As an entity translocates through a pore connecting two electrolytic solutions (for example between the inside and outside of a nanopipette), with an applied bias, resulting changes in the ionic current can provide information about the size and surface properties of the entity, as well as its speed of translocation.^{11, 16, 17} Typically, the presence of an insulating particle in the orifice of a pore causes a transient increase in the pore resistance (decrease in the ionic current),^{10, 17-19} the magnitude of which informs on the particle size.

Nanopipettes, are particularly attractive for resistive pulse experiments, as they can be prepared easily and rapidly from quartz or glass capillaries to give a range of tuned orifice sizes, usually of conical geometry, simply by adjusting the laser puller parameters.¹⁹⁻²³ The conical shape of the nanopore has potential benefits in that the electric field is greatest at the opening, where the nanopipette becomes narrower, providing a higher sensitivity for resistive pulse sensing.²² Consequently, applications of nanopipettes are expanding apace.²⁴⁻²⁶ Of relevance to the studies herein, the use of nanopipettes as reaction centers for monitoring the nanoscale crystallization of zinc phosphate has been described.²⁷ While applying a voltage bias across the nanopipette

opening, current oscillations were observed that were attributed to the precipitation and dissolution of zinc phosphate in the nanopipette opening. With precursor zinc and phosphate salts, one in the nanopipette and the other in the bathing solution, it was demonstrated that the sign of the applied bias could be used to drive either crystallization or dissolution at the nanopipette opening. We recently used this methodology to monitor the crystallization and dissolution of calcium carbonate in nanopipettes and showed this to be a powerful platform for rapidly screening crystal growth additives.²⁸ Additionally, the formation of inorganic salt nanoparticles in conical nanopores has been reported.²⁹⁻³¹

The above examples have considered aqueous crystallization, but some work in much larger pores, in borosilicate glass or silicon nitride, have considered the use of different solvents either side of the pore mouth (solvent/antisolvent system), which mix at the pore to produce a supersaturated solution.³² This is the type of system considered herein, but with the use of much smaller pores (50 nm diameter) formed using glass nanopipettes as illustrated in Figure 5.2.

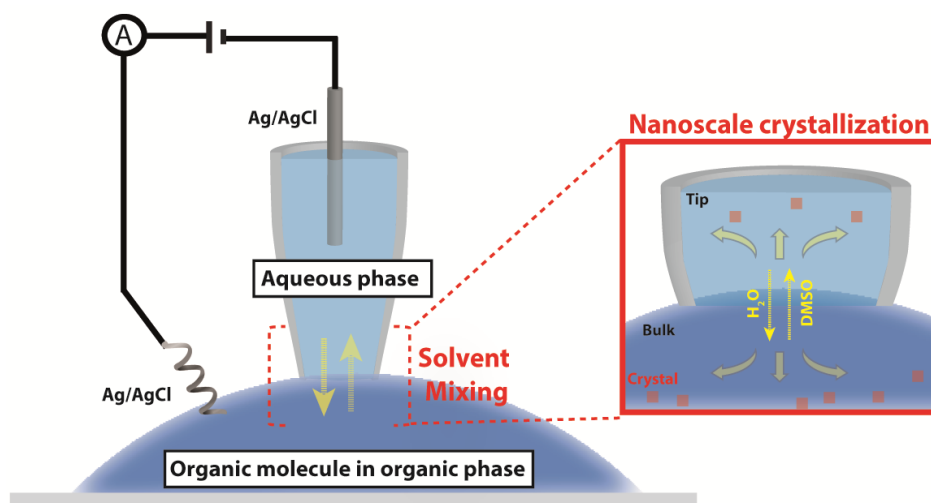
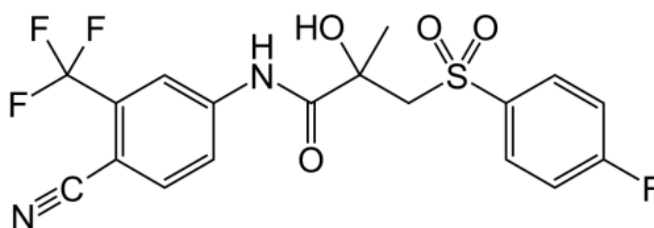


Figure 5.2. Schematic showing the crystallization of bicalutamide in a nanopipette.

Studies on this dimension are especially interesting because unusual polymorphs might be expected, due to the dramatic size-dependent stability properties of

polymorphs on this length scale.³³ With the use of finite element method (FEM) modeling, insight is provided into the solvent mixing phenomenon that leads to precipitation and the strong effect of applied bias that is observed. These new studies suggest that nanopipettes are potentially very useful devices for monitoring the nucleation of crystals in an antisolvent system and creating seeds for unusual polymorphs.



Scheme 5.1. Molecular structure of bicalutamide.

5.2. Experimental Section

5.2.1. Materials and Solutions

For all experiments, unless stated otherwise, the nanopipette contained 100 mM tetrabutyl ammonium chloride (TBA^+Cl^-), from Sigma-Aldrich, in ultrapure water (Purite, Select HP) of resistivity 18.2 $\text{M}\Omega\text{ cm}$ (at 25 °C). The bath solution consisted of dimethyl sulfoxide (DMSO, Fisher, purity 99.7%) solution containing 100 mM TBA^+Cl^- and 5 mM BIC. Solid crystalline BIC was kindly supplied by AstraZeneca.

5.2.2. Nanopipettes

Nanopipettes were fabricated from quartz capillaries, with an outer diameter of 1.00 mm and an inner diameter of 0.5 mm (Friedrich and Dimmock). Using a laser puller (P-2000, Sutter instruments), capillaries were pulled to give a nanopipette with an opening diameter of approximately 50 nm at the end and semi-angle that over a few

microns from the end approximated to *ca.* 3.7°. Several pulled pipettes were examined by transmission electron microscope (TEM) to confirm these dimensions were consistent.^{23, 34, 35}

5.2.3. BIC Crystallization Measurements

A two-electrode setup was employed with a AgCl-coated Ag QRCE inserted into a nanopipette filled with aqueous TBACl solution and a second similar QRCE was placed in the bulk DMSO solution. The current, I , was measured as a function of time with the potential, V , applied in a defined way (constant or linearly scanned with time), using a home-built potentiostat and electrometer. Potential control and data acquisition was achieved using an FPGA card (7852R, National Instruments) controlled by a LabVIEW 2013 interface, National Instruments. All measurements were made at 23 ± 1 °C. The potential of Ag/AgCl electrode in DMSO was monitored over time and was found to be stable as represented in Figure 5.3. This gives an idea of the overall equilibrium potential difference between the 2 electrodes in the experimental set up, which is small and close to zero compared to the applied potentials. The AgCl-coated Ag wire functions as a stable electrode in many aqueous media.^{28, 36-39}

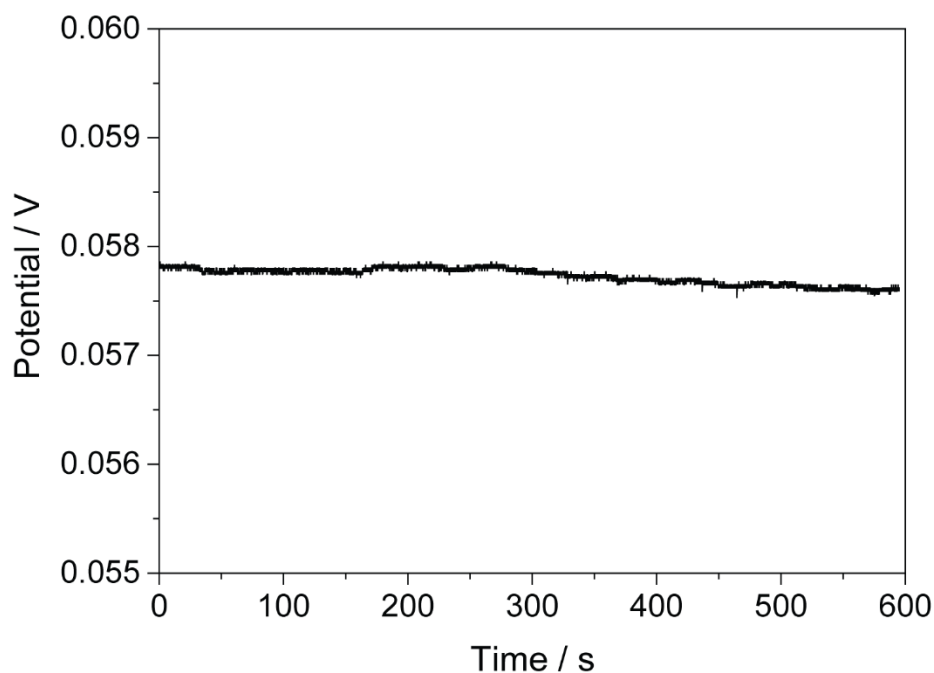


Figure 5.3. Using the same experimental setup as shown in Figure 5.4 and having no BIC in the bath solution, the stability of the Ag wire-coated Ag/AgCl in DMSO was measured by recording the potential of the electrode over time.

5.2.4. Raman Spectroscopy

Raman microscopy investigations of individual crystals employed a Renishaw inVia Reflex Raman Microscope fitted with a Charge Coupled Device (CCD) detector with a near-IR (633 nm) laser. A 50 \times objective lens was used.

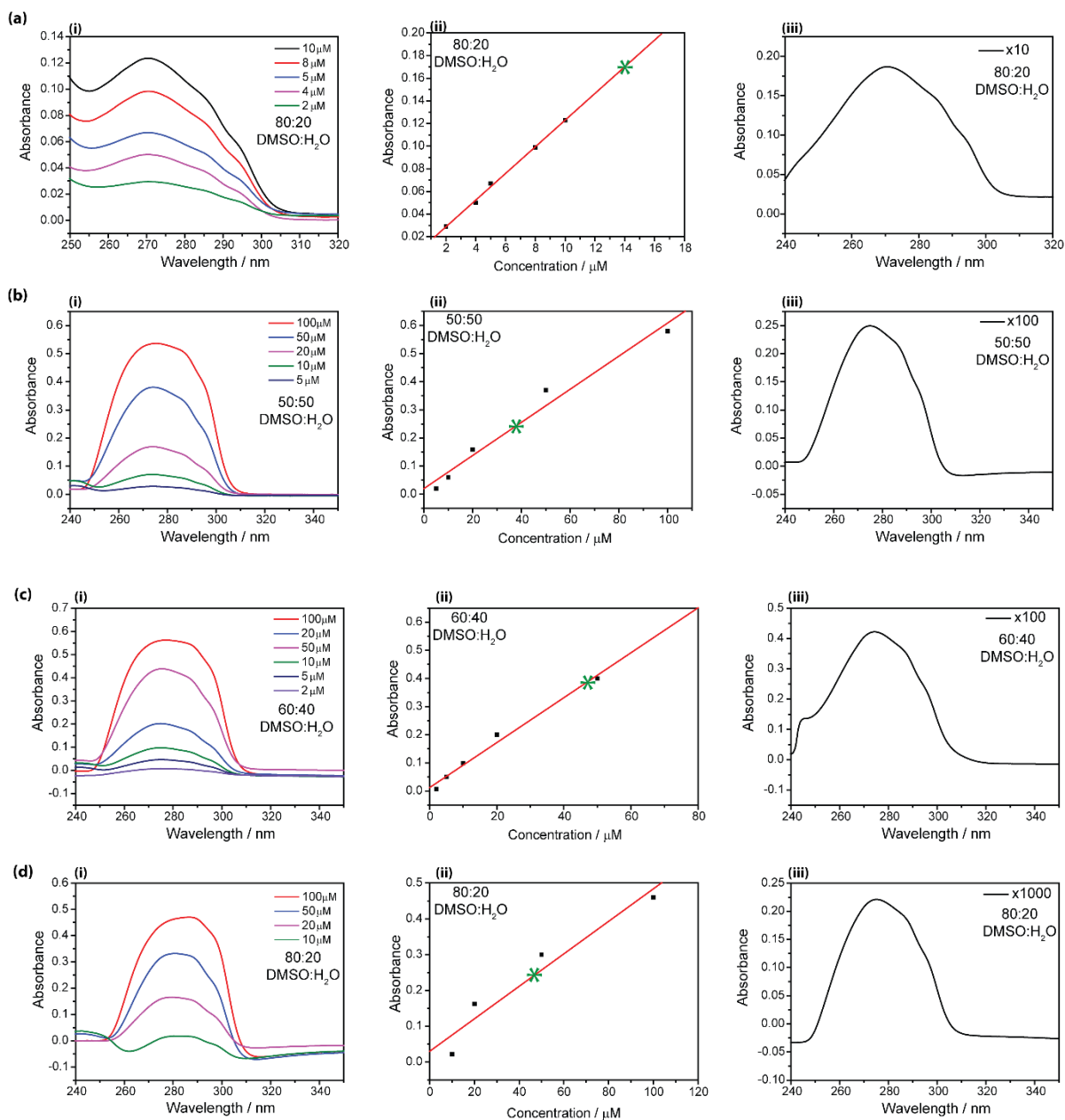
5.2.5. Finite Element Method Simulations

Finite element method (FEM) simulations were carried out to understand the mixing zone of the two solvents and extract saturation levels of BIC near the mouth of the nanopipette. These simulations were done using COMSOL Multiphysics 5.2a using

the transport of diluted species and electrostatics modules. Simulations used a 2D axisymmetric cylindrical geometry. The simulation domain, diffusion coefficients and boundary conditions are presented in the supporting information, section 5.5. Briefly, mixing of the solvents was treated as a diffusive process, given the nanoscale dimensions of the system⁴⁰, with bulk concentration of 55 M water initially inside the pipette and 14.1 M DMSO in the bulk solution. The simulations accounted for the dependence of the diffusion coefficient of H₂O and DMSO on the H₂O: DMSO ratio (see supporting information, section 5.5.2.), but for simplicity assumed no changes in the solution density (volume) in the mixing zone, so that a Newtonian fluid model could be assumed. The density and volume of mixed H₂O: DMSO solutions is known and was reasonably assumed no density or volume changes. For a mole fraction of water up to 0.65 which applies to most of the nanopipette tip, the density (and volume) of solutions is very similar to that of water.^{41,42} Although molar enthalpy is negative for H₂O, DMSO mixing,⁴³ the value is moderate, and due to the rapid mixing of solvents, and the nanoscale mixing zone in the tip, the temperature was considered to be constant.

100 mM TBA⁺Cl⁻ was present inside and outside the pipette, with 5 mM BIC in the bath solution. Simulations considered several different applied biases, of relevance to the experiments. Saturation levels of BIC at different spatial locations were calculated based on the local proportion of water to DMSO, and measured saturation levels, as shown in table 5.1 acquired from UV-Vis. All UV-Vis spectra were recorded in continuous mode with Jasco V-660 spectrophotometer for a range of DMSO: H₂O mixtures and different BIC concentration values, to produce calibration plots from which the BIC solubility could be determined in each case. UV-Vis spectra of BIC dissolved in different ratios of DMSO: H₂O solutions, represented in Figure 5.4 (a-g) (i) UV-Vis spectra of different concentrations of BIC in different compositions of DMSO: H₂O mixtures. (a-g) (ii) Linear fit showing peak absorption acquired from (i) versus BIC concentration. (a-g) (iii) Spectra recorded in different compositions of H₂O and DMSO containing BIC at the saturated concentration, with the solution then

diluted by the factor indicated as an inset. Using the linear calibration fits of absorbance versus concentration for each ratio represented in (a-g) (ii), the concentration value that corresponded to the acquired absorption point for all the different compositions were obtained, represented by the green asterisk, from which the BIC solubility values shown in Table 5.1 were obtained.



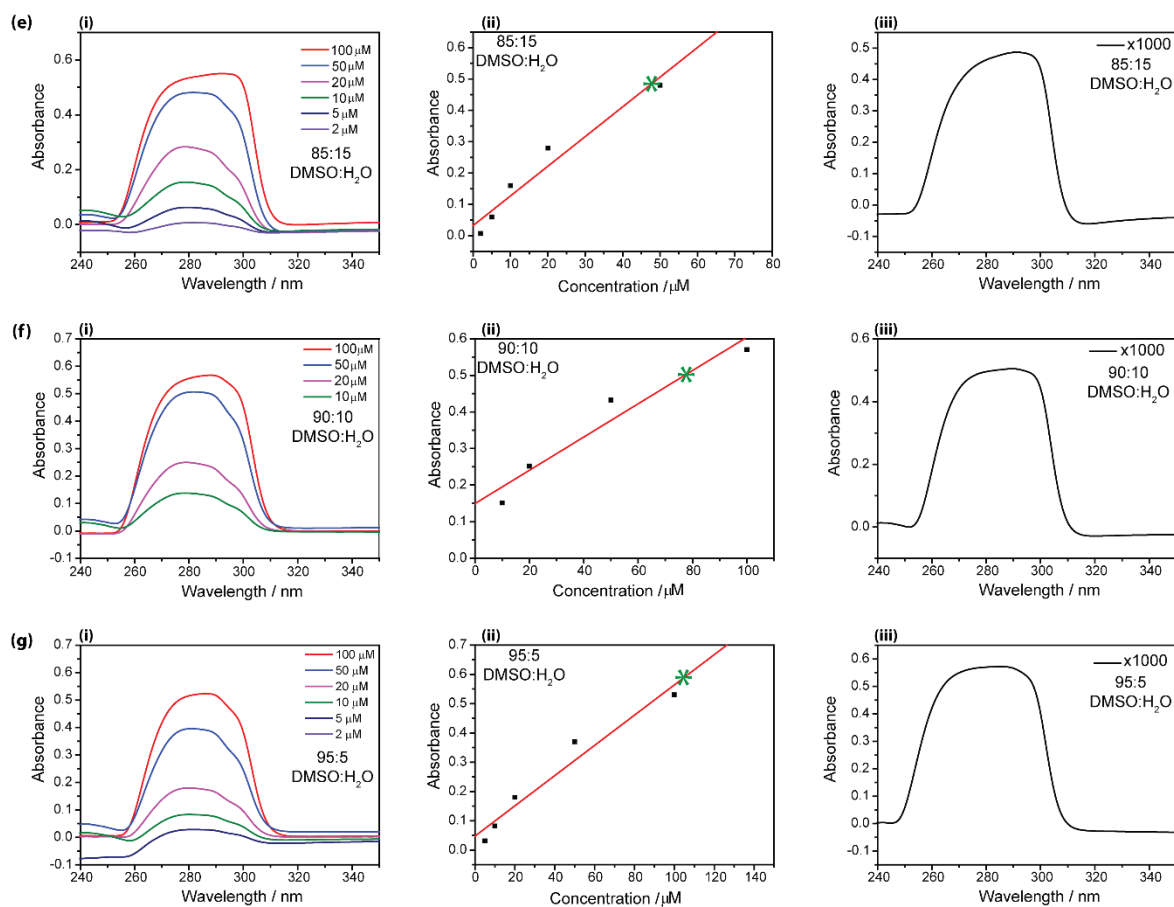
Figure 5.4. UV-Vis spectra of BIC dissolved in different ratios of DMSO: H₂O solutions.

Table 5.1. Solubility concentrations of BIC

Volume ratio (DMSO : H ₂ O)	Solubility concentration (mM)
95:05	103
90:10	78
85:15	47
80:20	43
60:40	4.8
50:50	3.7
20:80	0.14

5.3. Results and Discussion

5.3.1. Crystallization of Bicalutamide in a Nanopipette

A schematic of the typical experimental setup for monitoring BIC nucleation and growth events is depicted in Figure 5.5. As mentioned above, the nanopipette was filled with 100 mM TBA⁺Cl⁻ dissolved in water, and this was placed in a bath consisting of 5 mM BIC and 100 mM TBA⁺Cl⁻ dissolved in DMSO. Note that for many of the experiments the concentration of BIC used (5 mM) was much lower than the saturation concentration in pure DMSO (200 mM), but occasionally different concentrations were used, as stipulated herein. A bias applied between the QRCE in the nanopipette and one in bulk solution generated an ionic current that could be used to monitor changes in the resistance at the end of the nanopipette. When a bias of -0.3

V was applied to the nanopipette electrode, transient current blockages (current decreases) were observed in the current-time ($I-t$) trace, as shown in Figure 5.6 (a) (i). These events, which have a frequency of $8 \pm 1 \text{ s}^{-1}$ (*vide infra*), are attributed to the formation of BIC crystals near the end of the nanopipette, causing an increase in the system resistance and decrease in the ionic current. A zoom view of one of the events (Figure 5.6 (a) (ii)) shows that they are relatively slow (*ca.* 100 ms), with a very sharp decrease in current, followed by a slower recovery to the nanopipette open state current. Experiments performed with different biases revealed that these events exhibited a dependence on the applied bias. Figure 5.6 (b) and (c) show samples from $I-t$ traces performed with applied bias of -0.1 V and -0.5 V. With increasing bias, a higher frequency of blockage events was observed.

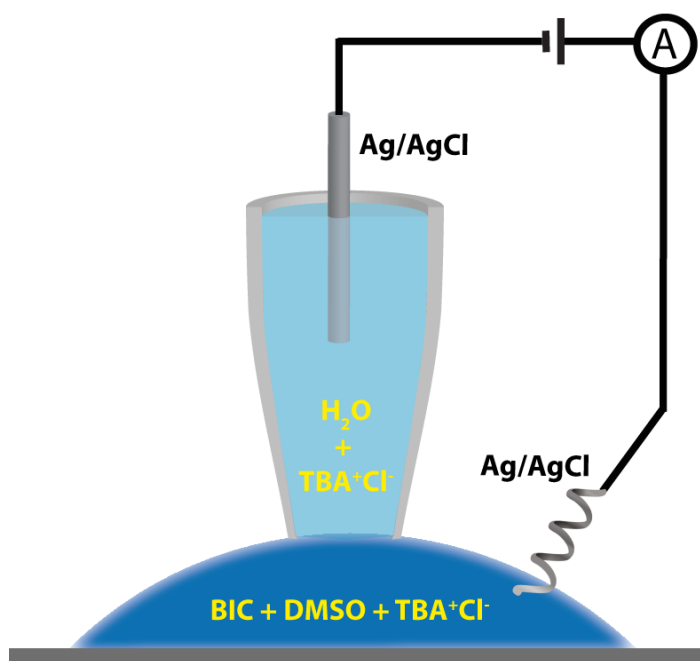


Figure 5.5. Setup (not to scale) for voltage dependent nucleation of BIC in conical nanopipettes. A bias was applied between an electrode in a nanopipette containing aqueous electrolyte and an electrode in DMSO solution containing BIC. The current response was measured as a function of time and applied potential.

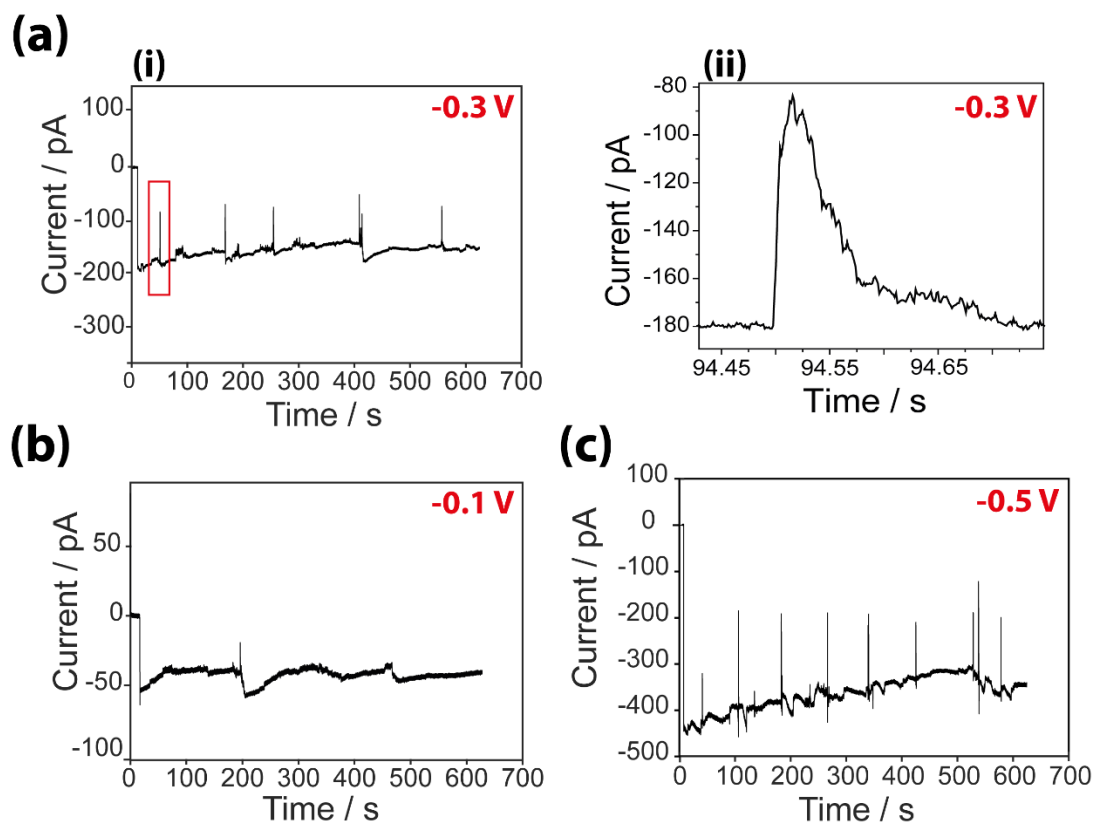


Figure 5.6. Current-time response with 5 mM BIC in the DMSO bath at different potentials applied to the tip with respect to the Ag/AgCl electrode in bulk: (a) (i) -0.3 V, with inset (ii) showing expanded view of highlighted event; (b) -0.1 V; and (c) -0.5 V.

To confirm that the blockage events were due to BIC, the I - t and current-voltage (I - V) behavior were also recorded in cases where 0 mM and 200 mM BIC was present in the bath DMSO solution. Figure 5.8 (a) (i) shows example I - t data for a tip bias of -0.3 V for the case where no BIC was present in the bath solution. Under these conditions, a featureless, steady I - t trace was observed, with no transient blockages, suggesting that the nanopipette remained in its open state throughout. The open state current is *ca.* -150 pA, broadly similar to the open state in Figure 5.6 (a) (i), recorded with a

different nanopipette. Likewise, the I - V curve in Figure 5.8 (a) (ii) shows the rectification characteristics expected for a small tip of this size,⁴⁴ that have negatively charged walls.⁴⁵⁻⁴⁷

With the same nanopipette electrode bias of -0.3 V, but higher concentration of 200 mM BIC in the DMSO phase (Figure 5.8 (b) (i)), a very high frequency of blockages was observed, manifested as an oscillating current between the open and blocked state. In fact, the frequency of events is so high that a fully open state current is never achieved. At 10 mM and 20 mM BIC in the DMSO solution the event frequency was 4.1 ± 0.2 and $8.2 \pm 0.4 \text{ min}^{-1}$, respectively (data provided in Figure 5.8). These data indicate that the frequency of events is strongly dependent on BIC concentration in the DMSO phase.

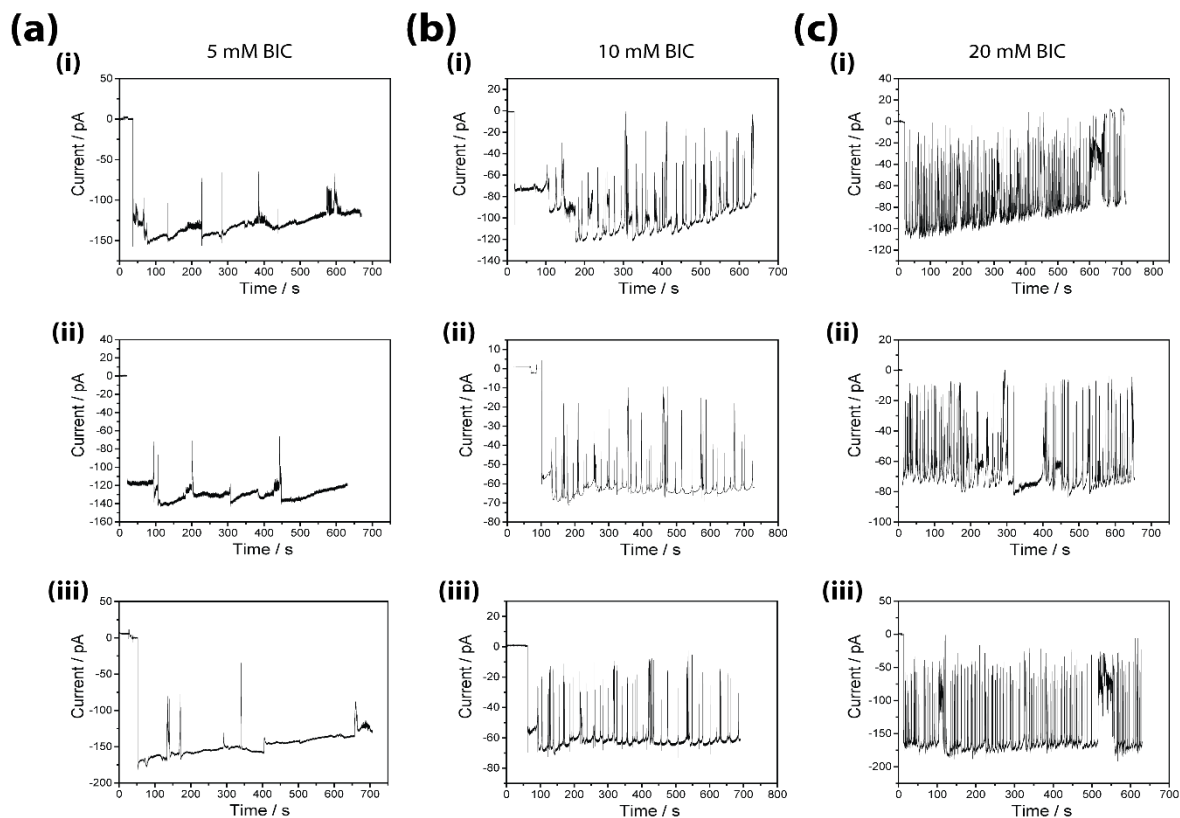


Figure 5.7. Current-time response at 0.3 V with different concentrations of BIC in the DMSO bath; 5mM, 10 mM and 20 mM. Shown are 3 sets of repeats (i-iii) for each concentration.

The I - V measurements presented in Figure 5.7 (b) (ii) further reveals the effect of applied bias on the blockage behavior. At negative tip potentials with 200 mM BIC in DMSO, rapid blockage and clearance events to an open state are observed, but such behavior is not seen at positive tip potentials or in the case where no BIC is present (Figure 5.7 (a) (ii)).

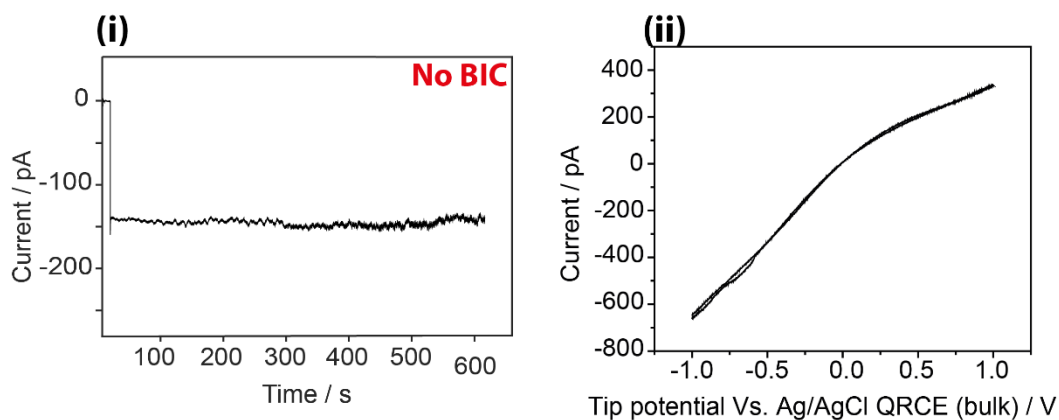
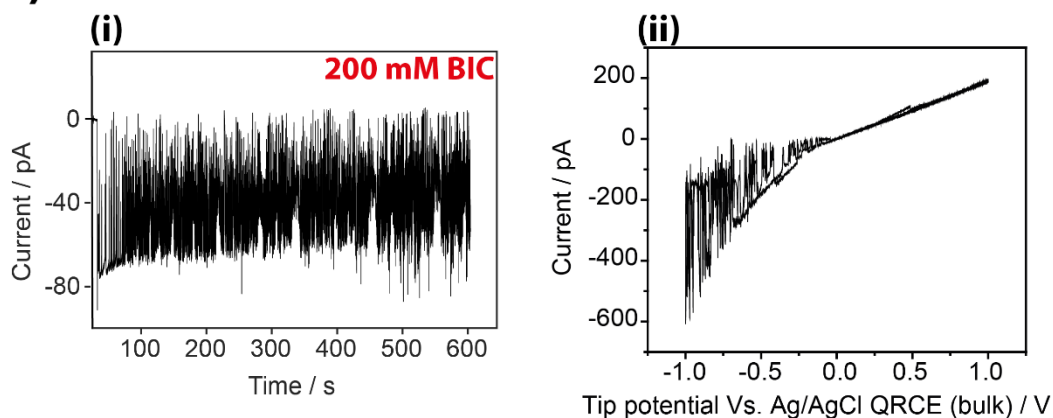
(a)**(b)**

Figure 5.8. Current-time response at a nanopipette electrode potential of -0.3 V for: (a) (i) no BIC in DMSO and (b) (i) 200 mM BIC in DMSO. Corresponding I - V curves of each nanopipette prior to current-time measurements are shown in (a) (ii) and (b) (ii).

Nanoprecipitation events observed herein are driven predominantly by the antisolvent effect⁴⁸ due to the poor solubility of BIC in water ($11.6 \mu\text{M}$).⁴ Based on our experimental observations, proposed is that the DMSO and water phases mix locally and rapidly (*vide infra*) at the nanopipette opening. This mixing leads to the protonation of BIC by water, as BIC has a pK_a of 12,⁵ as illustrated in Figure 5.9.

Consequently, at negative nanopipette electrode biases, protonated BIC (positively charged) will be driven into the body of the nanopipette by the applied electric field, but the high-water content of the mixed phase at the end of the nanopipette (*vide infra*), means that the solution becomes locally supersaturated with respect to BIC and nucleation occurs. Particle formation (and growth) causes a transient increase in the system resistance and blockage of the ionic current. In contrast, in the case where a positive tip bias was applied, no blockage events were seen, consistent with protonated BIC being largely excluded from the nanopipette opening. Thus, the applied bias has a significant effect in promoting or inhibiting crystallization, even though the two solvents presumably mix to similar extents irrespective of the bias.

The blip responses observed, suggest a process where BIC particles form (leading to a decrease in the ion conductance current) and subsequently either translocate out of the pipette orifice or move further up the conical pipette whose dimensions get wider, re-establishing the baseline open-state conductance current. It has previously been shown that the surface charge of a translocating particle can have an impact on the shape of the resistive pulse and is strongly influenced by the concentration of supporting electrolyte used.^{11, 49, 50} High electrolyte concentration screens the charge on the particle and the nanopipette walls (short Debye length) and so particle charge has little effect, whereas at low electrolyte concentration the Debye length is larger. To explore this aspect, *I-t* measurements were performed with a lower electrolyte concentration (10 mM TBA⁺Cl⁻), with some example data shown in Figure 5.10. In these instances, the transient shape is more complicated showing both an increase resistive pulse, described above, but accompanied by an increase in conductance state at some times in an overall “event”. These features are broadly similar to features seen on charged particles⁴⁹⁻⁵³ although in the case of Figure 5.10, the features are much more complex and could also result from some repetitive nucleation and redissolution events in the growth of a particle (e.g. transformation from one solid phase to another via a solution-mediated process). Additionally, these events are somewhat slow for a particle translocation event,⁴⁹ and would suggest that the particle, and evolving entity, rattles

in the end of the pipette before leaving the reaction zone. Based on the fact that BIC is protonated in the aqueous phase, the surface charge of the particle is likely to be positive. In this case, the particle would be expected to migrate into the nanopipette (given the applied field) but, as we show below, some particles evidently leave the nanopipette, perhaps due to physical flow of the more dense aqueous phase into the DMSO phase, which is not considered in the simplified model that is presented below.

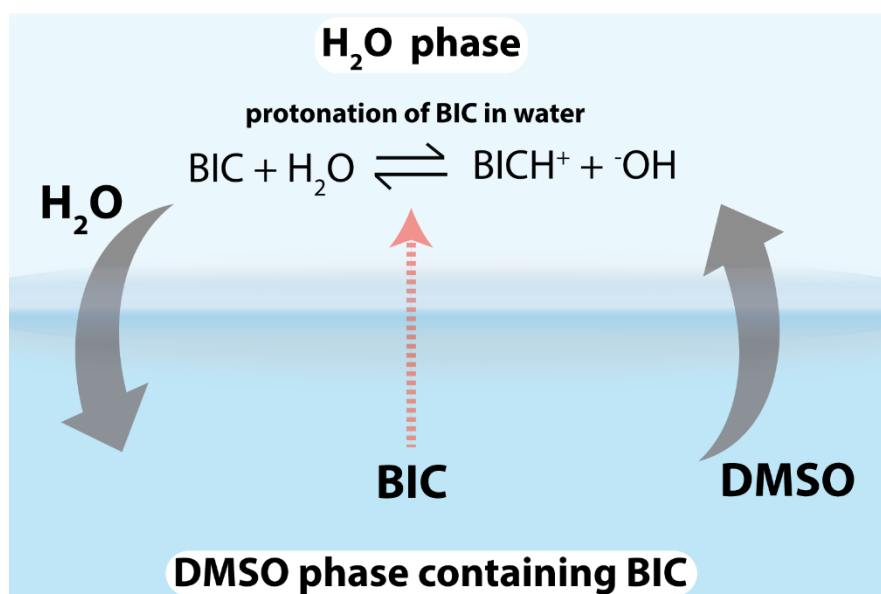


Figure 5.9. Water-DMSO mixing near the mouth of the nanopipette and the subsequent transfer and protonation of BIC in the water phase.

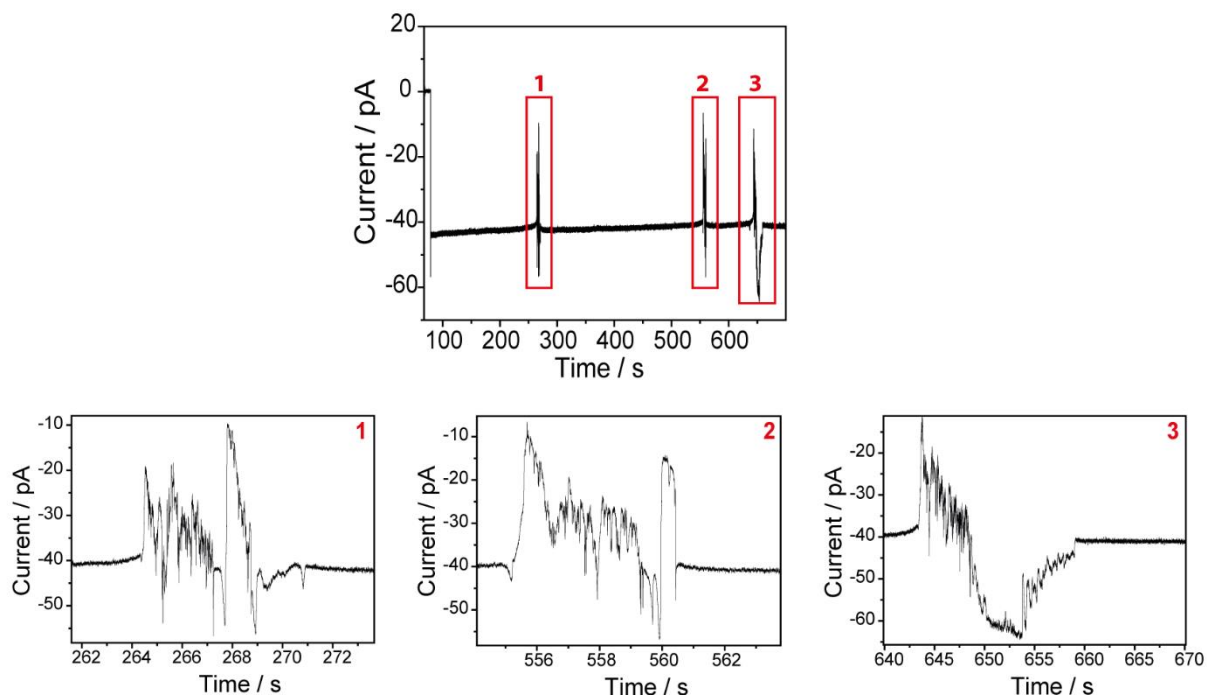


Figure 5.10. Current-time response at a nanopipette electrode potential of -0.3 V using 10 mM TBA^+Cl^- in each phase and 5 mM BIC in the DMSO phase. Expanded views of highlighted events (1-3) are shown.

In order to estimate saturation levels of BIC inside a nanopipette, time-dependent FEM simulations were performed with 100 mM TBA^+Cl^- in the nanopipette (water) and bath DMSO solutions. 5 mM BIC was present in the bath solution at the start of the simulation. BIC had neutral charge in the bulk organic phase and became protonated in the aqueous phase, as shown in Figure 5.9.

Figure 5.11 presents profiles that show of how the concentrations of water and DMSO in the end of the nanopipette, as well as the local saturation level of BIC, varies with time after immersing a nanopipette (aqueous solution) into a bath (DMSO). A bias of -0.3 V was applied to the nanopipette electrode. It can be seen that the water concentration towards the end of the pipette decreases from the bulk value, as water is transported out of the nanopipette into the DMSO phase. The DMSO concentration, on the other hand, can be seen to propagate up the length of the pipette with increasing

time as DMSO diffuses into the pipette. The diffusion of BIC into the nanopipette, together with the higher concentration of water, results in the solution becoming highly supersaturated with respect to BIC, with extreme saturation levels ($\Omega = [\text{BIC}]_{\text{total}} / [\text{BIC}]_{\text{sat}}$) of up to 140, which is the reason why the crystallization process is so driven. It can be seen that quasi-steady profiles are produced at times between 10 ms and 100 ms.

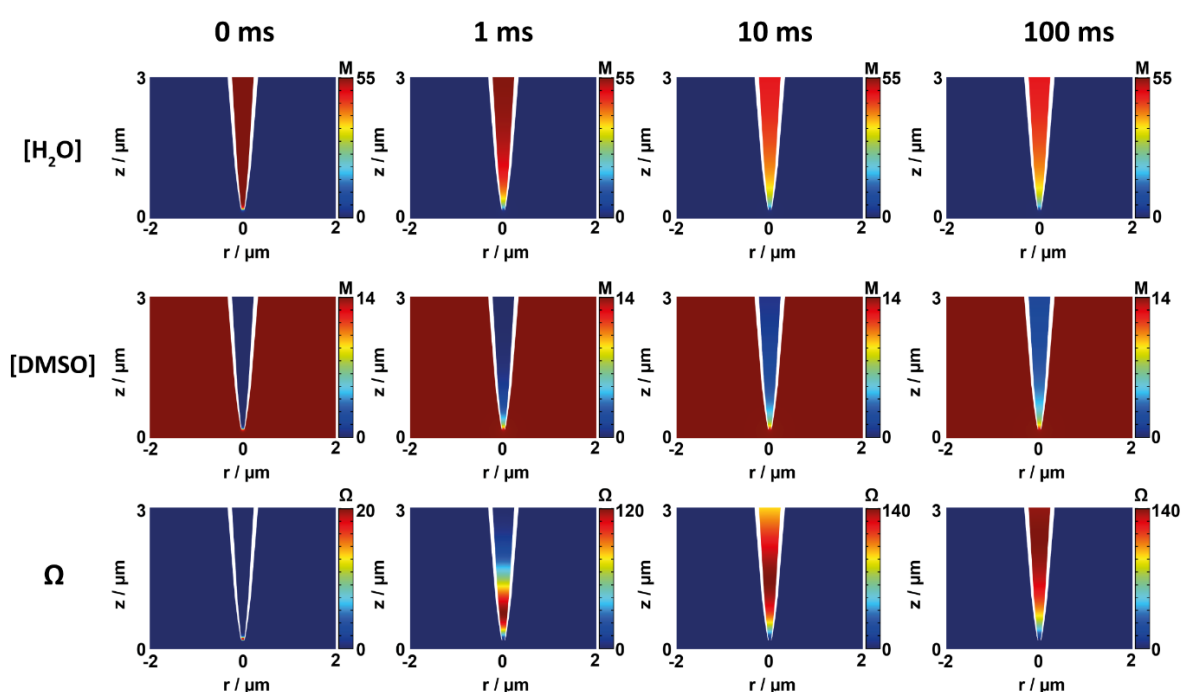


Figure 5.11. Concentration profiles of water, DMSO and BIC saturation levels ($\Omega = [\text{BIC}]_{\text{total}} / [\text{BIC}]_{\text{sat}}$) at times of 0 ms, 1 ms, 10 ms and 100 ms after immersing a nanopipette containing aqueous electrolyte into DMSO (5 mM BIC and electrolyte).

Nanopipette electrode bias of -0.3 V.

The experimental data presented and discussed above, suggest a strong influence of the applied bias polarity on the crystallization process. Crystallization was only seen

in the case where a negative bias was applied to the nanopipette electrode. This behavior was explored further with FEM simulations. After a diffusional mixing time of 1 second, with an applied bias of -0.3 V to the nanopipette electrode, high relative saturation levels were observed throughout the tip, of up to $\Omega = 142$ were observed a few microns up the length of the nanopipette (Figure 5.12 (a)). At these high saturation levels, nucleation and growth of BIC crystals is strongly favored, as mentioned above. In contrast, in the case where a positive bias was applied, Ω values above 1 were not seen, as shown in Figure 5.12 (b) and so crystallization would not be expected, as is the case experimentally under these conditions. Importantly, the solution was never supersaturated ($\Omega > 1$) outside of the nanopipette domain, in either case, suggesting that any BIC particles must form inside the pipette.

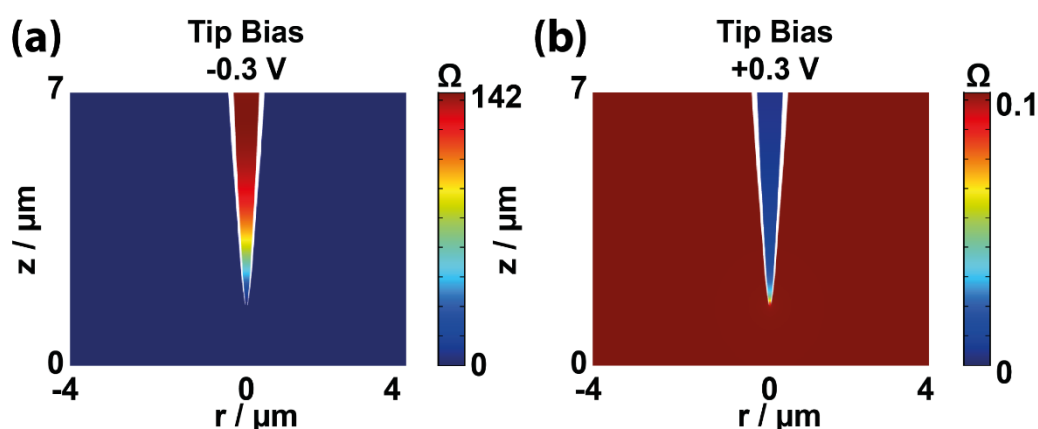


Figure 5.12. Predicted BIC saturation levels with a bias of -0.3 V (a) and +0.3 V (b) applied to the upper nanopipette boundary. Simulations were performed in 100 mM TBA⁺Cl⁻ with 5 mM BIC in the DMSO phase initially.

To accelerate the process, Figure 5.14 (a) shows an optical micrograph taken of a nanopipette after BIC growth experiments had been performed for ~10 min with 200 mM BIC in the bath. It reveals solid products formed from these experiments inside

the tip. Crystals were also found to grow on the glass surface directly beneath where the probe was positioned for these growth experiments (Figure 5.14 (b)). The presence of these crystals outside the nanopipette is evidence that particles translocate the nanopipette orifice, and continue to grow and settle on the glass substrate beneath. Crystals were not observed in cases where a positive tip bias was applied to the electrode in the nanopipette.

To confirm that the crystals formed were BIC, Raman Spectroscopy was employed, shown in Figure 5.14 (c). BIC has two polymorphs, represented in Figure 5.13.

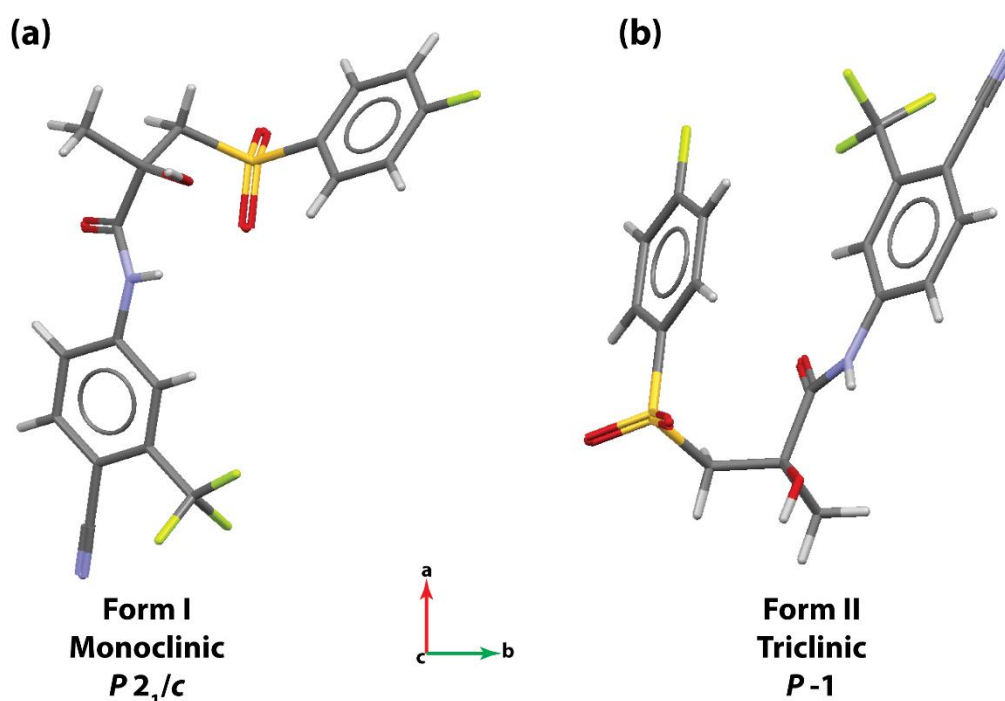


Figure 5.13. Single molecule diagrams of bicalutamide form I and II.

Characterization of the resulting peaks for these samples lead to the conclusion that the formed crystals are of Form II BIC (comparing the data to Raman spectroscopy of reference compounds elsewhere).⁵⁴ In particular, the strong peak at around 1600 cm^{-1} is found in both BIC Forms, but the Form II crystal has π - π stacking interactions, which

causes an extra peak at 1582 cm^{-1} , as highlighted in Figure 5.14 (c) that is not present in the spectrum of Form I. Form I is the more stable polymorph at all temperatures and Form II is labelled as the metastable state.⁵⁵ Crystallization of BIC from bulk solutions at room temperature usually leads to Form I. Form II can be produced from the transformation of (solid-state) amorphous BIC at room temperature and this could be the route followed in this case, i.e. the high supersaturations that are attained at the end of the nanopipette (Figure 5.14 (a)) could promote crystallization of the amorphous form, with transition to Form II.⁵⁵ A further consideration is that at the nanoscale, smaller crystals generally have higher free energies than larger ones, and the formation of the polymorph with the thermodynamically most stable bulk structure is not necessarily the one with the most stable surface structure.⁵⁶⁻⁵⁸ Crystal surface energy is significant for polymorph stability and the effect is further emphasized when the nature of the solvent is considered.^{33, 56}

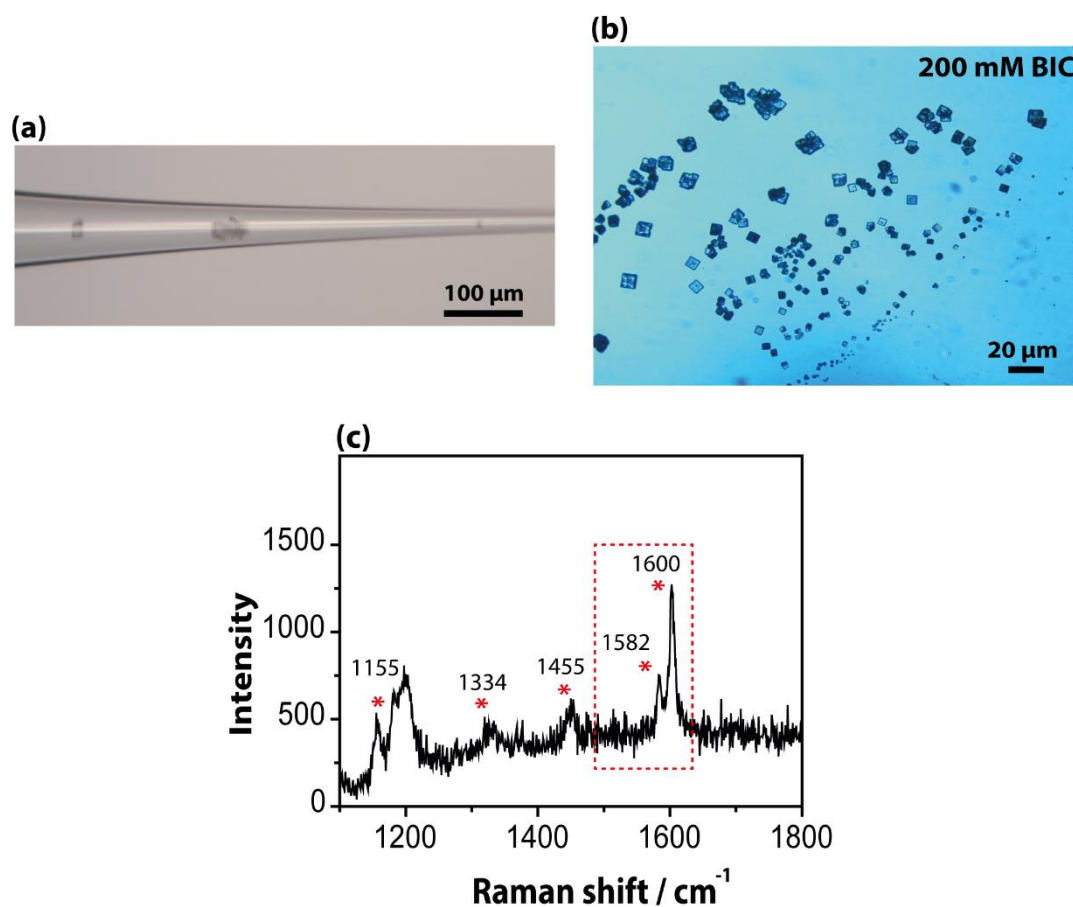


Figure 5.14. (a) Optical image of a typical nanopipette used in time-current measurements with 200 mM BIC in bath showing the formation of crystals inside the tip. (b) Additional formation of crystals in the bath containing 200 mM BIC after a nanopipette crystallization experiment. (c) Raman spectrum of BIC crystals formed, with main peak positions marked. The peaks highlighted at 1582 and 1600 cm^{-1} are most useful in resolving the BIC crystal type.

5.4. Conclusions

In this study, it is shown that the nucleation and growth of BIC nanoparticles can be induced and monitored in real time using a simple nanopipette system. The approach advocated is an antisolvent/solvent approach in which crystallization is induced by the mixing of DMSO and water at the mouth of a nanopipette, with the applied bias providing control over the extent of crystallization. The bias applied can be used to promote or stop nucleation. Simultaneously, by measuring the current-time response at a given applied potentials current oscillations are observed which were attributed to, and shown to result from, the formation, and subsequent translocation, of BIC particles near the nanopipette orifice.

With this simple approach, it has been demonstrated that seeds can be produced that lead to the formation of Form II BIC at room temperature. To support the experiments, detailed FEM simulations have provided valuable information that help to validate the nucleation process, and provide estimates for the supersaturation levels achieved experimentally. In the future, with this unique, simple yet powerful nanoscale methodology, other APIs with polymorphic properties could be explored, as well as formulations of amorphous solid dispersions. There is also, the possibility of implementing this system for seed synthesis at larger scales, using multi porous membranes and designer potential-time profiles that promote nucleation and particle ejection.

5.5. Supporting Information

5.5.1. Finite Element Method Simulations

In order to estimate the saturation levels of BIC that would be attained in nanopipette experiments, FEM simulations were performed with a 50 nm inner diameter nanopipette positioned in bulk solution. The concentrations applied inside and outside of the nanopipette are displayed in Figure 5.15. Ionic transport was assumed to follow the Nernst-Planck relationship, where the flux, J_i , of species, i , is given as:

$$J_i = -D_i \Delta c_i - z_i \frac{F}{RT} D_i c_i \nabla \phi \quad (1)$$

and the Poisson equation describes the electrical potential, ϕ :

$$\nabla^2 \phi = -\frac{F}{\epsilon \epsilon_0} \sum_i z_i c_i \quad (2)$$

where c_i denotes the species concentration, D_i and z_i denote the diffusion coefficient and charge number of the charge of species i and F , R , T , ϵ and ϵ_0 specify constants: the Faraday constant, gas constant, temperature, relative permittivity and vacuum permittivity, respectively. The diffusion coefficients for water and DMSO were obtained from Table 5.2 and varied freely in the simulations according to the local liquid composition. The diffusion coefficient for BIC, as a function of solvent composition, was estimated from the local mole fraction of water and DMSO and the pure solvent diffusion coefficients, presented in Table 5.3, assuming a linear relationship between mole fraction and diffusion coefficient. BIC was initially considered to have a charge of zero when in the organic phase. The protonation of BIC in the aqueous phase was included in the simulations with the rate of formation of BICH^+ from BIC given in equation 3.

$$R_{\text{BICH}^+} = k[\text{BIC}][\text{H}_2\text{O}] \quad (3)$$

where k was set to be $10 \times 10^8 \text{ mol}^{-1} \text{ dm}^3 \text{ s}^{-1}$, rapid compared to the diffusional mixing time, and $[\text{BIC}]$ and $[\text{H}_2\text{O}]$ are the local concentrations of the deprotonated form of BIC and water respectively. OH^- ions are formed at the same rate, with the neutral form of BIC removed (mass balance).

Time-dependent simulations were performed allowing 1 second of mixing to give the saturation profiles presented in Figure 5.11. The saturation level, Ω was defined as:

$$\Omega = \frac{[\text{BIC}]_{\text{total}}}{[\text{BIC}]_{\text{sat}}} \quad (4)$$

where $[\text{BIC}]_{\text{total}}$ includes protonation and neutral forms and $[\text{BIC}]_{\text{sat}}$ was the value measured by UV-Vis spectroscopy.

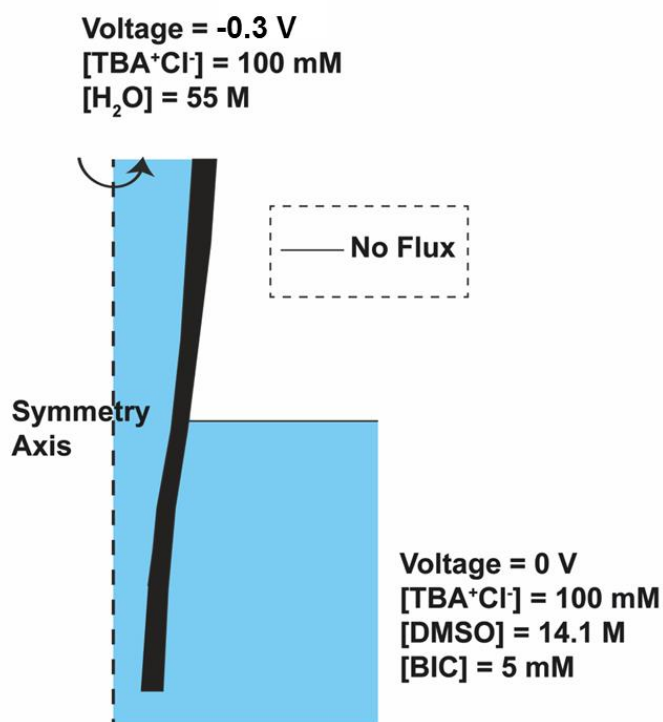


Figure 5.15. Schematic of FEM simulation domain with applied boundary conditions.

5.5.2. Diffusion Coefficients

Table 5.2. Diffusion coefficients of H₂O and DMSO in different compositions of DMSO and H₂O,⁵⁹ as used for FEM simulations

Mole fraction H ₂ O	Diffusion coefficient (cm ² /s) of H ₂ O	Diffusion coefficient (cm ² /s) of DMSO
0	0	8.50×10^{-6}
0.1	8.40×10^{-6}	7.50×10^{-6}
0.2	8.00×10^{-6}	7.20×10^{-6}
0.3	8.40×10^{-6}	6.00×10^{-6}
0.4	8.30×10^{-6}	5.30×10^{-6}
0.5	8.00×10^{-6}	4.80×10^{-6}
0.6	7.00×10^{-6}	4.00×10^{-6}
0.7	6.80×10^{-6}	4.00×10^{-6}
0.8	1.00×10^{-5}	5.30×10^{-6}
0.9	1.20×10^{-5}	6.50×10^{-6}
1	2.60×10^{-5}	0

Table 5.3. Calculated Diffusion coefficients of bicalutamide in H₂O and DMSO using the Wilke Chang equation.⁶⁰

Diffusion coefficient of bicalutamide in H ₂ O (cm ² /s)	Diffusion coefficient of bicalutamide in DMSO (cm ² /s)
4.48×10^{-6}	3.34×10^{-6}

5.6. References

- (1) Vippagunta, S. R.; Brittain, H. G.; Grant, D. J. W. *Advanced Drug Delivery Reviews* **2001**, 48, 3-26.
- (2) Abu-Diak, O. A.; Jones, D. S.; Andrews, G. P. *Journal of Pharmaceutical Sciences* **2012**, 101, 200-213.
- (3) Andrews, G. P.; AbuDiak, O. A.; Jones, D. S. *Journal of Pharmaceutical Sciences*, 99, 1322-1335.
- (4) Ren, F.; Jing, Q.; Tang, Y.; Shen, Y.; Chen, J.; Gao, F.; Cui, J. *Drug Development and Industrial Pharmacy* **2006**, 32, 967-972.
- (5) Kumbhar, D. D.; Pokharkar, V. B. *Colloids and Surfaces A: Physicochemical and Engineering Aspects* **2013**, 416, 32-42.
- (6) Li, C.; Li, C.; Le, Y.; Chen, J.-F. *International Journal of Pharmaceutics* **2011**, 404, 257-263.
- (7) Singhal, D.; Curatolo, W. *Advanced Drug Delivery Reviews* **2004**, 56, 335-347.

- (8) DeBlois, R. W.; Bean, C. P. *Review of Scientific Instruments* **1970**, *41*, 909-916.
- (9) Kozak, D.; Anderson, W.; Vogel, R.; Trau, M. *Nano today* **2011**, *6*, 531-545.
- (10) Berge, L. I.; Feder, J.; Jo/ssang, T. *Review of Scientific Instruments* **1989**, *60*, 2756-2763.
- (11) Holden, D. A.; Hendrickson, G.; Lyon, L. A.; White, H. S. *The Journal of Physical Chemistry C* **2011**, *115*, 2999-3004.
- (12) Keyser, U. F. *Journal of The Royal Society Interface* **2011**, *8*, 1369-1378.
- (13) Venkatesan, B. M.; Bashir, R. *Nature Nanotechnology* **2011**, *6*, 615-624.
- (14) Heins, E. A.; Siwy, Z. S.; Baker, L. A.; Martin, C. R. *Nano Letters* **2005**, *5*, 1824-1829.
- (15) Shi, W.; Friedman, A. K.; Baker, L. A. *Analytical Chemistry* **2017**, *89*, 157-188.
- (16) Fraccari, R. L.; Ciccarella, P.; Bahrami, A.; Carminati, M.; Ferrari, G.; Albrecht, T. *Nanoscale* **2016**, *8*, 7604-7611.
- (17) Bayley, H.; Martin, C. R. *Chemical Reviews* **2000**, *100*, 2575-2594.
- (18) DeBlois, R. W.; Bean, C. P.; Wesley, R. K. A. *Journal of Colloid and Interface Science* **1977**, *61*, 323-335.
- (19) Howorka, S.; Siwy, Z. *Chemical Society Reviews* **2009**, *38*, 2360-2384.
- (20) Murray, R. W. *Chemical Reviews* **2008**, *108*, 2688-2720.
- (21) Dekker, C. *Nature Nanotechnology* **2007**, *2*, 209-215.
- (22) Lan, W.-J.; Holden, D. A.; Zhang, B.; White, H. S. *Analytical Chemistry* **2011**, *83*, 3840-3847.

- (23) Perry, D.; Momotenko, D.; Lazenby, R. A.; Kang, M.; Unwin, P. R. *Analytical Chemistry* **2016**, 88, 5523-5530.
- (24) Vilozy, B.; Actis, P.; Seger, R. A.; Vallmajo-Martin, Q.; Pourmand, N. *Analytical Chemistry* **2011**, 83, 6121-6126.
- (25) Cai, H.; Wang, Y.; Yu, Y.; Mirkin, M. V.; Bhakta, S.; Bishop, G. W.; Joshi, A. A.; Rusling, J. F. *Analytical Chemistry* **2015**, 87, 6403-6410.
- (26) Morris, C. A.; Friedman, A. K.; Baker, L. A. *Analyst* **2010**, 135, 2190-2202.
- (27) Vilozy, B.; Actis, P.; Seger, R. A.; Pourmand, N. *ACS Nano* **2011**, 5, 3191-3197.
- (28) Perry, D.; Parker, A. S.; Page, A.; Unwin, P. R. *ChemElectroChem* **2016**, 3, 2212-2220.
- (29) Siwy, Z. S.; Powell, M. R.; Petrov, A.; Kalman, E.; Trautmann, C.; Eisenberg, R. S. *Nano Letters* **2006**, 6, 1729-1734.
- (30) Powell, M. R.; Sullivan, M.; Vlassioug, I.; Constantin, D.; Sudre, O.; Martens, C. C.; Eisenberg, R. S.; Siwy, Z. S. *Nature Nanotechnology* **2008**, 3, 51-57.
- (31) Innes, L.; Powell, M. R.; Vlassioug, I.; Martens, C.; Siwy, Z. S. *The Journal of Physical Chemistry C* **2010**, 114, 8126-8134.
- (32) Yusko, E. C.; Billeh, Y. N.; Mayer, M. *Journal of Physics: Condensed Matter* **2010**, 22, 454127.
- (33) Belenguer, A. M.; Lampronti, G. I.; Cruz-Cabeza, A. J.; Hunter, C. A.; Sanders, J. K. M. *Chemical Science* **2016**, 7, 6617-6627.
- (34) Sa, N.; Baker, L. A. *Journal of the Electrochemical Society* **2013**, 160, H376-H381.
- (35) Chen, C.-C.; Baker, L. A. *Analyst* **2011**, 136, 90-97.

- (36) Ebejer, N.; Güell, A. G.; Lai, S. C.; McKelvey, K.; Snowden, M. E.; Unwin, P. R. *Annual Review of Analytical Chemistry* **2013**, *6*, 329-351.
- (37) Patel, A. N.; Collignon, M. G.; O'Connell, M. A.; Hung, W. O. Y.; McKelvey, K.; Macpherson, J. V.; Unwin, P. R. *Journal of the American Chemical Society* **2012**, *134*, 20117-20130.
- (38) Maddar, F. M.; Lazenby, R. A.; Patel, A. N.; Unwin, P. R. *Physical Chemistry Chemical Physics* **2016**, *18*, 26404-26411.
- (39) Güell, A. G.; Meadows, K. E.; Dudin, P. V.; Ebejer, N.; Macpherson, J. V.; Unwin, P. R. *Nano Letters* **2014**, *14*, 220-224.
- (40) Lee, C.-Y.; Chang, C.-L.; Wang, Y.-N.; Fu, L.-M. *International journal of molecular sciences* **2011**, *12*, 3263-3287.
- (41) Cowie, J. M. G.; Toporowski, P. M. *Canadian Journal of Chemistry* **1961**, *39*, 2240-2243.
- (42) De Visser, C.; Heuvelsland, W. J.; Dunn, L. A.; Somsen, G. *Journal of the Chemical Society, Faraday Transactions 1: Physical Chemistry in Condensed Phases* **1978**, *74*, 1159-1169.
- (43) Catalán, J.; Díaz, C.; García-Blanco, F. *The Journal of Organic Chemistry* **2001**, *66*, 5846-5852.
- (44) Wei, C.; Bard, A. J.; Feldberg, S. W. *Analytical Chemistry* **1997**, *69*, 4627-4633.
- (45) White, H. S.; Bund, A. *Langmuir* **2008**, *24*, 2212-2218.
- (46) Momotenko, D.; Girault, H. H. *Journal of the American Chemical Society* **2011**, *133*, 14496-14499.
- (47) Lan, W.-J.; Edwards, M. A.; Luo, L.; Perera, R. T.; Wu, X.; Martin, C. R.; White, H. S. *Accounts of Chemical Research* **2016**, *49*, 2605-2613.

- (48) Lonare, A. A.; Patel, S. R. *International Journal of Chemical Engineering and Applications* **2013**, *4*, 337.
- (49) Lan, W.-J.; Kubeil, C.; Xiong, J.-W.; Bund, A.; White, H. S. *The Journal of Physical Chemistry C* **2014**, *118*, 2726-2734.
- (50) Menestrina, J.; Yang, C.; Schiel, M.; Vlassiounk, I.; Siwy, Z. S. *The Journal of Physical Chemistry C* **2014**, *118*, 2391-2398.
- (51) Chang, H.; Kosari, F.; Andreadakis, G.; Alam, M. A.; Vasmatazis, G.; Bashir, R. *Nano Letters* **2004**, *4*, 1551-1556.
- (52) Kowalczyk, S. W.; Dekker, C. *Nano Letters* **2012**, *12*, 4159-4163.
- (53) Smeets, R. M. M.; Keyser, U. F.; Krapf, D.; Wu, M.-Y.; Dekker, N. H.; Dekker, C. *Nano Letters* **2006**, *6*, 89-95.
- (54) Tres, F.; Patient, J. D.; Williams, P. M.; Treacher, K.; Booth, J.; Hughes, L. P.; Wren, S. A. C.; Aylott, J. W.; Burley, J. C. *Molecular Pharmaceutics* **2015**, *12*, 1512-1522.
- (55) Vega, D. R.; Polla, G.; Martinez, A.; Mendioroz, E.; Reinoso, M. *International Journal of Pharmaceutics* **2007**, *328*, 112-118.
- (56) Navrotsky, A.; Mazeina, L.; Majzlan, J. *Science* **2008**, *319*, 1635-1638.
- (57) McHale, J. M.; Navrotsky, A.; Perrotta, A. J. *The Journal of Physical Chemistry B* **1997**, *101*, 603-613.
- (58) Navrotsky, A. *ChemPhysChem* **2011**, *12*, 2207-2215.
- (59) Packer, K. J.; Tomlinson, D. J. *Transactions of the Faraday Society* **1971**, *67*, 1302-1314.
- (60) Wilke, C.; Chang, P. *AIChE Journal* **1955**, *1*, 264-27

Chapter 6

Electrochemical oxidation of dihydronicotinamide adenine dinucleotide (NADH): Comparison of highly oriented pyrolytic graphite (HOPG) and polycrystalline boron-doped diamond (pBDD) electrodes

The electro-oxidation of nicotinamide adenine dinucleotide (NADH) is studied at bare surfaces of highly oriented pyrolytic graphite (HOPG) and semi-metallic polycrystalline boron-doped diamond (pBDD). A comparison of these two carbon electrode materials is interesting because they possess broadly similar densities of electronic states that are much lower than most metal electrodes, but graphite has carbon sp^2 -hybridization, while in diamond the carbon is sp^3 -hybridised, with resulting major differences in bulk structure and surface termination. Using cyclic voltammetry (CV), it is shown that NADH oxidation is facile at HOPG surfaces but the reaction products tend to strongly adsorb, which causes rapid deactivation of the electrode activity. This is an important factor that needs to be taken into account when assessing HOPG and its intrinsic activity. It is also shown that NADH itself adsorbs at HOPG, a fact that has not been recognized previously, but has implications for understanding the mechanism of the electro-oxidation process. Although pBDD was found to be less susceptible to surface fouling, pBDD is not immune to deterioration of the electrode response, and the reaction showed more sluggish kinetics on this electrode. Scanning electrochemical cell microscopy (SECCM) highlights a significant voltammetric variation in electroactivity between different crystal surface facets that are presented to solution with a pBDD electrode. The electroactivity of different grains correlates with the local dopant level, as visualized by field emission-scanning electron microscopy. SECCM measurements further prove that the basal plane of HOPG has high activity towards NADH electro-oxidation. This work is published in Physical Chemistry Chemical Physics.

6.1. Introduction

Nicotinamide adenine dinucleotide (NADH) is an essential co-factor in various naturally occurring enzymatic reactions such as the oxidation of ethanol catalyzed by the enzyme alcohol dehydrogenase.¹ NADH is the terminal electron donor in the mitochondrial electron transport chain. As such, the development of robust methods of analysis for NADH is of considerable importance, with electrochemical methods proving particularly effective. The mechanism of NADH oxidation has been studied extensively by Moiroux and Elving²⁻⁵ and it is well established that at neutral pH, NADH undergoes a two-electron one-proton oxidation process of the ECE (electron transfer-chemical step-electron transfer) type:



A wide range of carbon electrode materials have received considerable attention for NADH electro-oxidation, including glassy carbon,^{4,6} carbon paste,⁷ carbon nanotubes,^{8,9} graphene¹⁰ and graphene composites,¹¹⁻¹³ pyrolytic graphite¹⁴ and boron-doped diamond.¹⁵ The study of NADH oxidation on bare carbon electrode surfaces is non-trivial.¹⁶ Relatively high overpotentials are often required and, furthermore, the oxidation products of NADH, particularly NAD^+ tend to adsorb strongly and foul surfaces quickly.^{5,17, 18}

Electrode surface modification has been considered as a means of achieving an effective decrease in overpotential for NADH oxidation.^{19,20} However, studies of unmodified electrodes are valuable both to provide a benchmark and to seek the optimal electrode format. The electrochemistry of NADH at conducting

diamond has received attention, but the focus has mainly been on hydrogen-terminated diamond,^{15, 21} with oxygen terminated diamond¹⁴ receiving only scant attention. Despite its importance as a well-defined model surface for sp^2 carbon, there are no reports of NADH oxidation at highly oriented pyrolytic graphite (HOPG) electrodes. It is important to note that the oxidation of NADH has been investigated at edge plane pyrolytic graphite (EPPG) and basal plane pyrolytic graphite (BPPG),¹⁴ but these materials should not be confused with HOPG. BPPG is a material with a much smaller crystallite size than HOPG, and hence has considerable edge plane character similar, in fact, to EPPG.²²

Comparison of electrochemical processes at HOPG and pBDD electrodes is interesting as they have broadly similar densities of electronic states (DOS) at the Fermi level over the typical range of potentials relevant for electrochemistry *ca.* $(2-6) \times 10^{20} \text{ cm}^{-3} \text{ eV}^{-1}$,^{23,24} that is about 1-2 orders of magnitude lower than metal electrodes. Yet, in other respects these materials may show different properties from each other. pBDD is sp^3 hybridized and compared to other carbon electrodes, shows relatively high immunity to deactivation via fouling, long term stability and excellent reproducibility of voltammetry for many electrode reactions and repetitive voltammetric cycling.²⁵ HOPG is an sp^2 carbon, the surface of which can readily be prepared and renewed via mechanical cleavage. It comprises of extensive basal terraces with a low density of point defects,^{26,27} and a step edge density that depends on the grade (quality) of the HOPG.^{28,29} Although early work considered the basal surface of HOPG to have ultra-low (or no) electrochemical activity,^{27,29-39} recent studies have highlighted the high activity of the basal surface for both simple redox reactions and more complex coupled electron-proton transfer processes.^{22,40,41} In the case of outer sphere redox processes, electron transfer rates are at least as fast at HOPG as on platinum.²⁷

The studies reported herein on the electrochemical oxidation of NADH at HOPG and oxygen-terminated pBDD reinforce, and amplify, the recent models on the

properties and activity of these electrode materials, while also providing detailed new insights on adsorption and surface fouling (contamination) processes. These measurements are complemented with high resolution scanning electrochemical cell microscopy (SECCM)^{42,43} experiments to map the electrochemical activity of HOPG and pBDD and confirm the macroscopic findings. Making extensive use of macroscopic measurements at well-defined surfaces, for example, comparing the intrinsic activity of three different grades of HOPG that span step-edge density of more than 2 orders of magnitude.^{29, 41}

6.2. Experimental Section

6.2.1. Materials and Solutions

All chemicals were used as received. Aqueous solutions were prepared using high purity water (Purite, Select HP) with a resistivity of 18.2 MΩ cm at 25 °C. β-Nicotinamide adenine dinucleotide, reduced dipotassium salt hydrate (NADH, > 98 %), and phosphate buffer solution (pH 7.2) were purchased from Sigma-Aldrich. Sodium chloride (NaCl, 99.0 %, Sigma-Aldrich) was added to the phosphate buffer to give a phosphate buffer saline (PBS) solution. The working electrodes used in this study were a highly doped pBDD electrode, and HOPG electrodes of varying step edge densities. A 1 mm diameter pBDD disk electrode, used for macroscale electrochemistry was prepared in house from DIAFILM EA grade material (Element Six Ltd.).^{26,54} The average boron doping level of the pBDD material was *ca.* 5×10^{20} atoms cm⁻³, above the metallic threshold as confirmed by secondary ion mass spectrometry (SIMS).⁵³ The pBDD had a roughness of 1-2 nm within a facet and 1-5 nm between grains, flat on the scale of SECCM and voltammetric measurements.⁵¹ Studies of basal plane HOPG employed one of three different grades: either ZYB or SPI-3 grade (SPI Supplies, West Chester, PA), or an ungraded HOPG sample of the highest

quality,³⁰ originating from Dr. Arthur Moore at Union Carbide (now GE Advanced Ceramics), and kindly provided by Prof. R. L. McCreery of the University of Alberta, Canada, which is referred to throughout as “AM grade”). All HOPG samples were cleaved with Scotch tape to remove surface layers and reveal a fresh surface for study. This procedure has been shown to produce a very similar surface to mechanical cleavage.³⁰

6.2.2. Macroscale Electrochemistry

Cyclic voltammetry (CV) was carried out in a three-electrode setup using a potentiostat (CH Instruments Model 750A, Austin, TX). A silver chloride coated Ag wire (Ag/AgCl) served as a quasi-reference electrode (QRE), while Pt gauze was used as the counter electrode. The Ag/AgCl QRE has a stable potential because AgCl has fast dissolution kinetics and it is sparingly soluble.⁴⁴ All potentials are quoted against this QRE. The working electrodes (HOPG or pBDD) were as described above. On HOPG, a Teflon cell designed in house was used to provide a well-defined 3 mm diameter working cell; this has been described in detail in chapter 2.²⁹ Because the BDD disk was encapsulated in glass, this could simply be immersed in solution, along with the other electrodes. Solutions contained different concentrations of NADH, as specified, in 0.1 M PBS. All solutions were prepared fresh on the day of the experiments and kept in the dark at all times when not in use. CV was performed at various potential scan rates (50, 100, 200, 400, 600 and 800 mV s⁻¹) for the electro-oxidation of NADH at potentials between 0.0 and 1.0 V. CV measurements were made either: (1) as a series of different scan rates on an HOPG sample that was freshly cleaved before the series or (2) on a freshly cleaved surface for each scan rate. Making it clear when each protocol was used. The well-known scotch tape method was used to cleave HOPG.^{23,27-29,33,41,45-49} Similarly, the CV response of pBDD was measured either with or without polishing the electrode surface between each CV, and again state when each method was used. The pBDD electrode was polished with alumina particles (*ca.* 0.05 μm particle size,

Micropolish, Buehler, Germany) on a deionized water saturated polishing pad (Microcloth, Buehler, Germany) and then rinsed with deionized water to ensure the complete removal of alumina particles.

6.2.3. Scanning Electrochemical Cell Microscopy

High-resolution electrochemical imaging (SECCM) was performed on freshly cleaved HOPG (AM grade) and pBDD. The setup is shown schematically in Figure 6.1 and is described thoroughly elsewhere.⁴³ In brief, a tapered dual-channel borosilicate pipette, (with an opening diameter of *ca.* 400 nm for experiments on HOPG and *ca.* 1 μm for experiments on pBDD) was filled with electrolyte solution. Since the laser pipette pulling procedure produces two probes of closely similar dimension, the sister probe to that used for imaging was characterized with field emission-scanning electron microscopy (FE-SEM), at 5 kV using a SUPRA 55 variable-pressure system (Zeiss). The probe used was filled with 1 mM NADH (for experiments on HOPG) and 0.5 mM NADH in 0.1 M PBS solution (for experiments on pBDD). A Ag/AgCl quasi-reference counter electrode (QRCE) was inserted in each channel. The SECCM instrument comprised of a high dynamics *z*-piezoelectric positioner (P-753.3CD LISA, Physik Instrumente), on which the pipette probe was mounted and an *xy*-piezoelectric stage (P-622.2CL PIHera, Physik Instrumente) for sample mounting. Instrument control and data acquisition was achieved using an FPGA card (PCIe-7852R) with a LabVIEW 2011 interface (LabVIEW 9.0, National Instruments). A video camera (PL-B776U, Pixelink) with a $\times 2$ magnification lens (44 mm, InfiniStix, Edmund Optics) was used to aid tip-positioning.

A 200 mV bias, V_1 , was applied between the two QRCEs, giving rise to an ion conductance current (i_{DC}) across the meniscus formed at the end of the pipette (see Figure 6.1). The tip was oscillated sinusoidally perpendicular to the surface, using the output generated by a lock-in amplifier, at a frequency of 260 Hz, with a 20 nm peak-to-peak amplitude for the tip used for measurements on HOPG

and a 60 nm peak-to-peak amplitude for the tip used for pBDD measurements. The oscillation induced an alternating component of the ion conductance current (i_{AC}) across the meniscus, when the meniscus was in contact with the substrate, and this was used as a set-point for feedback, to maintain a constant tip-to-substrate separation during imaging.⁴³ The currents, i_{AC} and i_{DC} , were measured simultaneously along with the electrode surface current (i_{sub}).

The SECCM maps covered a $10 \times 10 \mu\text{m}$ area of HOPG consisting of 32 line scans (16 forward and 16 reverse) at a tip scan rate of $0.3 \mu\text{m s}^{-1}$. Each line comprised of 12957 pixels, each pixel representing a current value that was the average of 256 readings. These measurements were made at a fixed working electrode of 0.5 V (low driving force, *vide infra*). For pBDD, voltammetric SECCM⁵⁰ were employed in which the potential was swept between 0.0 and 0.8 V, at 300 mV s^{-1} in which the theta pipette probe was approached to the surface until meniscus contact was made, as sensed by a change in i_{AC} . At each pixel (point of meniscus contact) the working electrode potential was swept between 0.0 V to 0.8 V (vs. Ag/AgCl QRCE) and the current-voltage response was recorded. Hopping scans on pBDD recorded (typically with a resolution of 40×30 pixels) over an area of $60 \times 45 \mu\text{m}$ and consisted of the following: a probe approach rate towards the surface of $0.3 \mu\text{m s}^{-1}$ to meniscus contact; potential sweep of 300 mV s^{-1} (potential swept between 0.0 and 0.8 V); $1.2 \mu\text{m}$ retraction distance at a rate of $5 \mu\text{m s}^{-1}$, enough to break the meniscus contact and move to the next position at a scan rate of $1.2 \mu\text{m s}^{-1}$. The distance between each hop (pixel) was chosen to be $1.5 \mu\text{m}$, to avoid the overlap of adjacent probed areas.

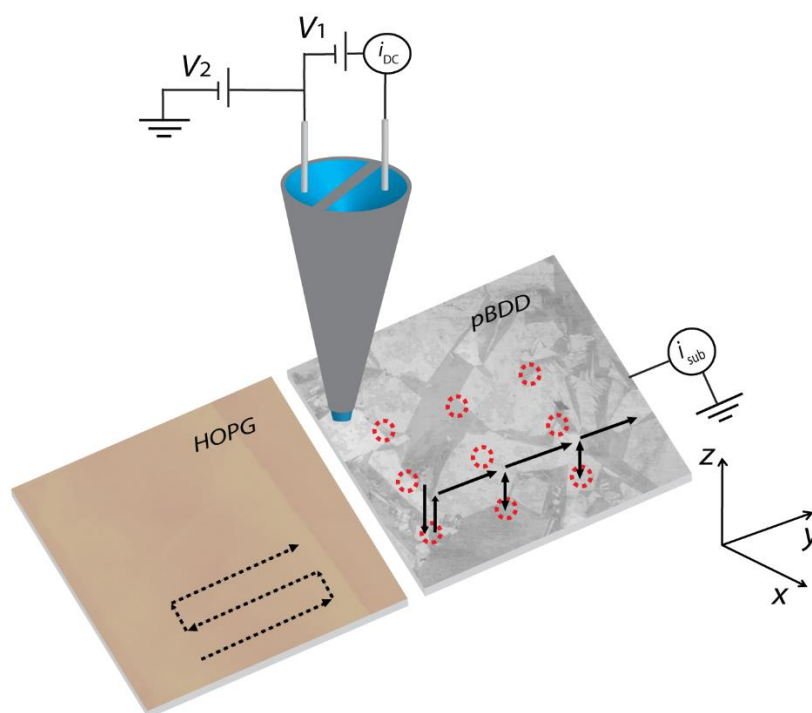


Figure 6.1. Schematic of the SECCM setup in which a theta pipette was used to create a tiny meniscus electrochemical cell on a carbon electrode surface (HOPG or pBDD) with the working electrode size determined by the size of the pipette opening and meniscus wetting of the substrate. An ion conductance current (i_{DC}) was generated by the potential bias, V_1 , between the two barrels of the pipette, while the voltage, V_2 , provided additional control of the potential of the working electrode. The resulting electrochemical current, i_{sub} , was measured to determine the local electroactivity. The conductance current has an AC component (see text for details), at the frequency of the pipette.

6.2.4. Atomic Force Microscopy

AFM images of HOPG topography were recorded in air, using an Innova® AFM in tapping mode (AM and SPI-3 HOPG) and a BioScope Catalyst™ BioAFM in ScanAsyst mode (ZYB HOPG).

6.3. Results and Discussion

6.3.1. Voltammetry of NADH Oxidation on HOPG and pBDD

Firstly, macroscale cyclic voltammetry (CV) measurements as a function of scan rate for ZYB grade HOPG and pBDD are considered. For the detail in Figure 6.2 (a) and (b), where j represents current density, an initial CV was run on either a freshly cleaved graphite surface, or polished pBDD, respectively, with no subsequent cleaning or cleaving before the subsequent voltammetric sweeps. In order to determine whether there was any electrode surface blocking, or other systematic effects, from the electrochemical process, as alluded to in the introduction, the first sweep was run at 50 mV s^{-1} , followed by a set of subsequent sweeps at a series of increasingly faster scan rates (100, 200, 400, 600 and 800 mV s^{-1}). The first thing to note is the significant difference in the onset potential for the oxidation of NADH at the two different electrodes. On pBDD (Figure 6.2 (a)), the NADH oxidation peak occurred at a potential of *ca.* $+0.55 \text{ V}$ (at 50 mV s^{-1}), which is in agreement with literature.¹⁵ As already noted, pBDD electrodes have high immunity to chemical fouling compared to other electrodes,²⁵ and so fairly well-defined successive waves are observed. The oxidation peak potential shifts slightly with increasing scan rate to a more positive potential. In comparison, in Figure 6.2 (b), at HOPG, electro-oxidation is much more facile, occurring at a lower anodic potential with a value of *ca.* $+0.40 \text{ V}$ for the peak current (at 50 mV s^{-1}). However, for CVs at increasing scan rates, the peak current does not increase as much at HOPG as might be expected, compared to the pBDD case, with the maximum peak current density

being only *ca.* $153 \mu\text{A cm}^{-2}$ at 800 mVs^{-1} (*cf.* $596 \mu\text{A cm}^{-2}$ at 800 mV s^{-1} for pBDD). Moreover, it can be seen that with increasing scan rates (number of scans), the voltammetric response becomes complex, with additional features appearing at more anodic potentials. This behavior, and its comparison to the pBDD response and the behavior on a surface freshly prepared before each voltammogram (discussed below), is strongly indicative of the HOPG surface becoming blocked by NADH oxidation products, as found for other carbon electrode materials.^{5, 14}

For comparison, CVs were run, for the same scan rates, at freshly polished pBDD or freshly cleaved HOPG prior to each CV. The results, shown in Figure 6.2 (c) and (d), highlight similar voltammetric behavior at pBDD to the response in Figure 6.2 (a), in which the surface was not cleaned between each CV at each scan rate. For HOPG, the difference between Figure 6.2 (b) and Figure 6.2 (d) is stark. CVs on freshly cleaved surfaces showed well-defined peaks of much higher current density magnitude that scale reasonably with the square root of scan rate, as indicative of a diffusion-limited process. The positive shift in oxidation peak potential for the electrode process is mostly a consequence of the strong adsorption of NAD^+ that is produced at the electrode during the oxidation of NADH. Although NAD^+ may behave as a mediator of electron transfers from NADH to the electrode through the adsorbed layer, it inhibits the rate of the reaction.²

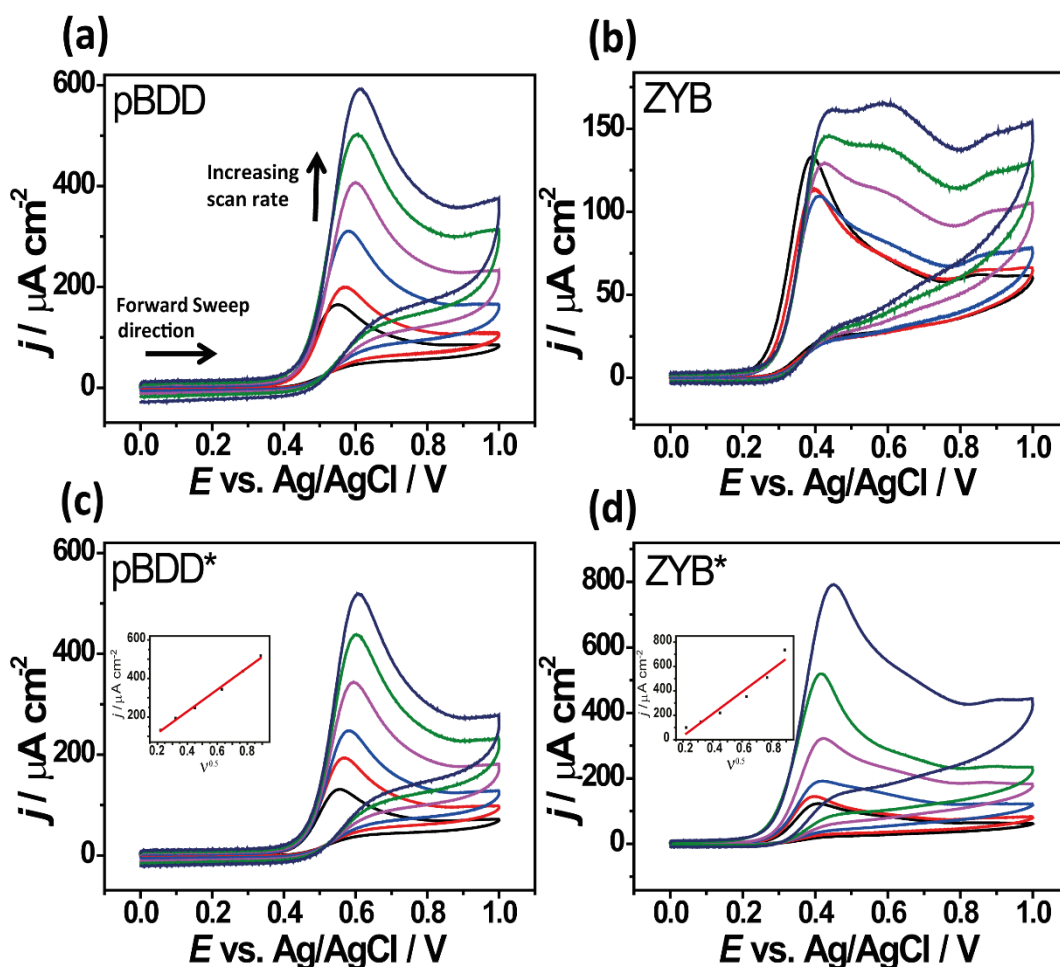


Figure 6.2. Oxidation of 1 mM NADH in 0.1 M PBS at various potential scan rates: 50, 100, 200, 400, 600 and 800 mV s^{-1} . For (a) pBDD and (b) ZYB the surface was cleaned or cleaved, respectively, prior to the first 50 mV s^{-1} scan, after which subsequent scans at increasing scan rates were run without further pretreatment or preparation of the electrode surface. For (c) pBDD* and (d) ZYB*, each voltammetric scan was made on a freshly polished pBDD or a freshly cleaved HOPG surface. The insets show plots of peak current vs. the square root of scan rate.

6.3.2. Repetitive Cyclic Voltammetric Response

The extent to which the responses of the different carbon electrodes changed during NADH (1 mM) oxidation was studied by recording consecutive CVs (10 runs at 100 mV s^{-1}), with 5 s intervals between each CV, for each electrode. Figure 6.3 shows characteristic CVs for repetitive cycling using three grades of HOPG: (a) AM, (b) ZYB and (c) SPI-3, and (d) pBDD.

The behavior of the three different grades of HOPG is closely similar for the initial scan, even though the step edge densities vary by more than 2 orders of magnitude,⁴¹ as shown in Figure 6.4. This strongly suggests that for graphite the electrochemical response is mainly determined by the basal surface, not the step edges. In the case of pBDD,⁵¹⁻⁵³ although recognized for combining high stability and resistance to chemical fouling, the repetitive cycling showed a decrease in current response over the 10 cycles, but not to the same extent as HOPG.

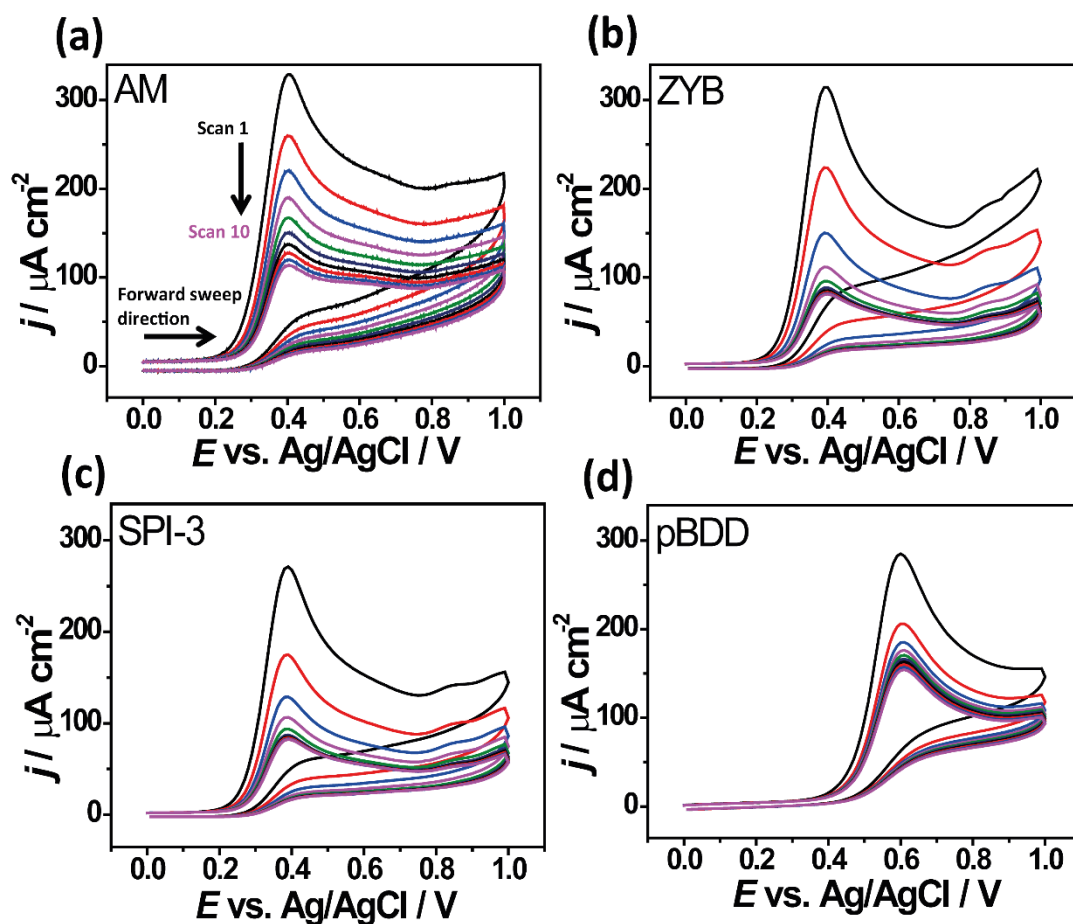


Figure 6.3. Repetitive cyclic voltammograms for the oxidation of 1 mM NADH on (a) AM, (b) ZYB, (c) SPI-3 grade HOPG and (d) pBDD in 0.1 M PBS, at a potential sweep rate of 100 mV s^{-1} . Each voltammogram was run with a 5 s interval between for a total of 10 cycles.

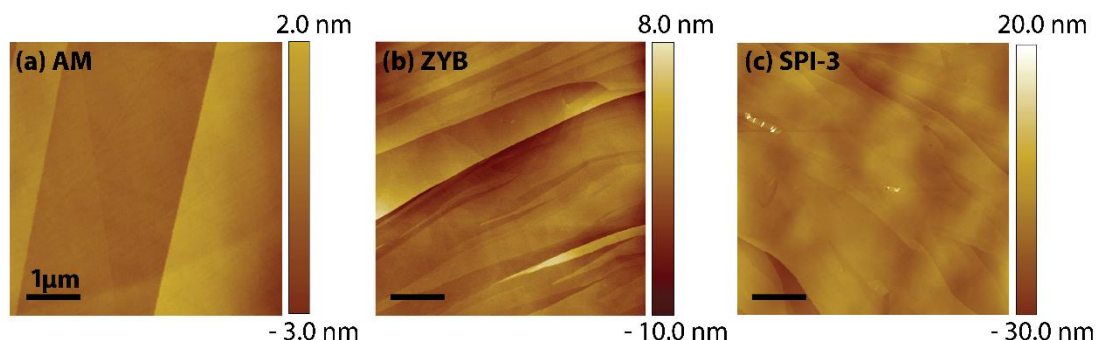


Figure 6.4. AFM topography images of freshly cleaved HOPG: (a) AM, (b) ZYB and (c) SPI-3 grades

6.3.3. Adsorption Behavior of NADH on HOPG

Although the studies herein indicate that the product of NADH adsorption, NAD^+ , adsorbs on both HOPG and pBDD, in line with studies on other electrodes,^{4,5} sought to elucidate whether NADH adsorbed. Early work suggested that NADH does not adsorb on pyrolytic graphite electrodes, although measurements were made at mM levels of NADH in bulk solution, and low to moderate voltammetry scan rates,⁴ where low levels of adsorption would be difficult to detect. For such studies HOPG was used, for which the background current is very low and decreased the concentration of NADH to $5\ \mu\text{M}$ where the diffusional-electrochemical response would be greatly attenuated, compared to any signal for adsorbed material. CVs were run on freshly cleaved surfaces of AM, ZYB and SPI-3 HOPG at different scan rates (Figure 6.5 (a-c) (i)). Significant oxidative signals are seen that can be attributed to adsorbed NADH, and the lack of any reverse process indicates that this is an irreversible (anodic stripping) process.⁵⁴ The data in Figure 6.5 (a-c) (ii) illustrate that the anodic peak current varies linearly with scan rate, as expected for electron-transfer to an adsorbed layer. Furthermore, the current density is noticeably greater on AM grade as compared to ZYB and SPI-3 HOPG. These latter grades of HOPG have higher step edge densities and have found in some other cases,^{27, 28} that this

appears to inhibit molecular adsorption. This suggests that the lateral interaction between adsorbed NADH is important, which is promoted on the extended basal surface of AM HOPG (Figure 6.4 (a)). This is also another explanation as to why NADH adsorption was not seen on pyrolytic graphite for which the step edge density is very high, along with the background (capacitive) currents during linear sweep voltammetry²²

To quantify amount of NADH adsorption, the area of the adsorbed voltammetric peaks was integrated to give the charge density, Q , for adsorbed NADH:

$$Q = nF\Gamma \quad (4)$$

where $n = 2$ is the number of electrons involved in the redox reaction, and F is the Faraday constant, from which Γ , the surface concentration of NADH (mol cm⁻²) could be obtained. Plots of charge density versus scan rate (ν) for each HOPG grade are given in Figure 6.5 (a-c) (iii) from which Γ values of 2.05×10^{-11} mol cm⁻² (AM grade), 1.03×10^{-11} mol cm⁻² (ZYB) and 1.21×10^{-11} mol cm⁻² (SPI-3) were obtained. Thus, the adsorption extent is rather small, but detectable, due to the low background currents at HOPG.

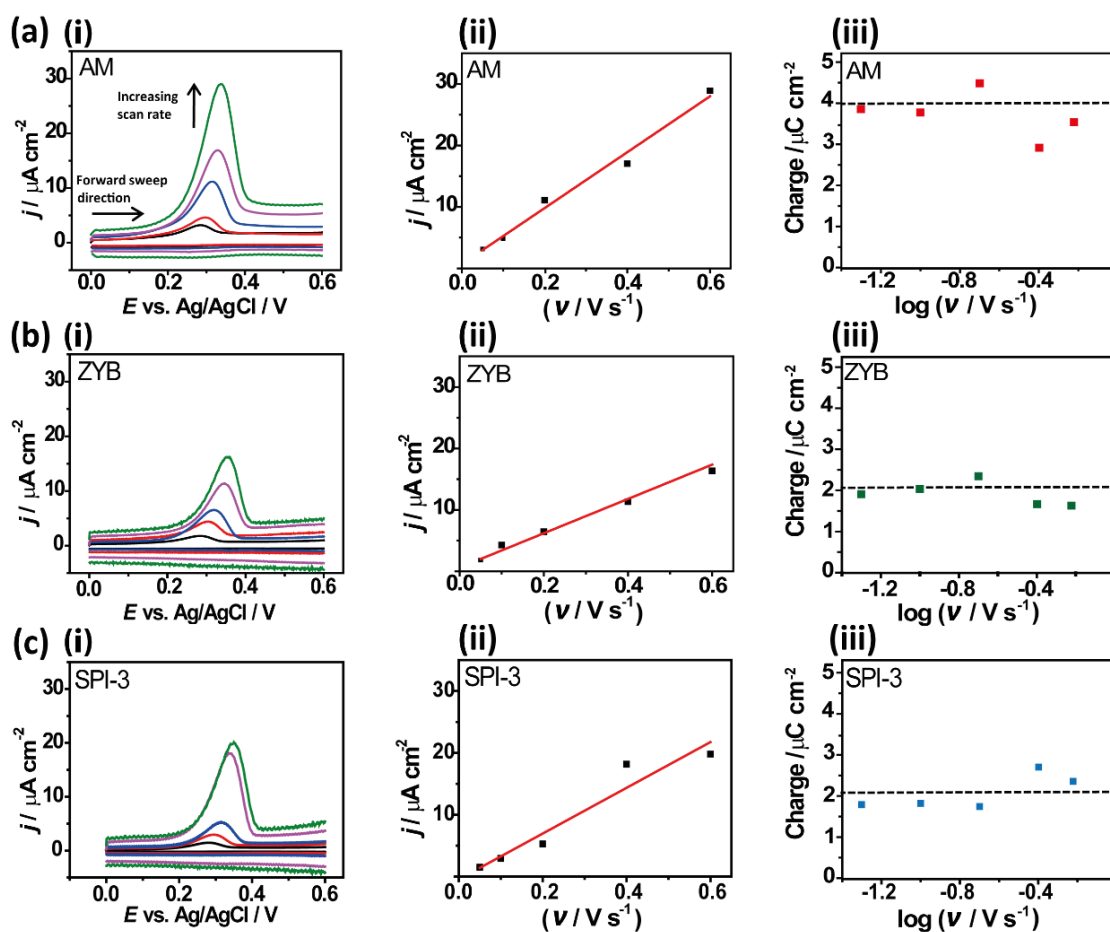


Figure 6.5. Oxidation of 5 μM NADH in 0.1 M PBS at various scan rates: 50, 100, 200, 400, and 600 mV s^{-1} at (a) (i) AM (b) (i) ZYB and (c) (i) SPI-3. (a-c) (ii) Plots of current density (forward wave) against scan rate and (a-c) (iii) variation of forward peak charge with the log of scan rate for the 3 different HOPG grades.

6.3.4. High Resolution Imaging of Electrochemical Activity

SECCM allows the measurement of surface electroactivity free from the topographical effects.⁵⁵ As highlighted above, the process of NADH oxidation can lead to the rapid deterioration of the electrode surface activity, which means that conventional electrochemical imaging techniques, where the whole electrode surface would be immersed in solution and carrying out this reaction - as in the case for scanning electrochemical microscopy (SECM)³² - would be of limited use. The advantage of SECCM is that only a small fraction of the surface at a time is in contact with the electrolyte solution during a scan. Moreover, by judicious selection of the local meniscus contact time, measurements can be made on a close to pristine surface, before surface blocking occurs, and blocking products can be left behind as the probe meniscus moves to a new location on the surface.⁵⁶

Firstly, SECCM measurements were performed on HOPG (AM grade). Two successive CVs with 1 mM NADH on AM grade HOPG at 100 mV s⁻¹ with a meniscus contact diameter of 400 nm are shown in Figure 6.6 (a). A large hysteresis between the forward and reverse waves is observed. On this CV time scale, which has a relatively high mass transfer coefficient, similar to a disk electrode of about 10 times the contact diameter (i.e. 4 μ m), a sigmoidal response would have been expected for a simple electrochemical reaction, with the forward and reverse waves closely similar.⁵⁷ The observation can be attributed to a blocking of the electrode. Additionally, the peak in the first forward wave decreases in the second scan, also indicating blocking of the electrode by reaction products. SECCM mapping of surface electrochemistry was carried out with 1 mM NADH in 0.1 M PBS at a potential of 0.5 V (Figure 6.6 (a)), in order to not fully drive the oxidation reaction and minimize blocking, with a lateral probe scan rate of 0.3 μ m s⁻¹. The residence time was about 1 s and based on the measured currents of *ca.* 4 pA, about 10⁷ molecules were turned over at the surface in contact with the meniscus cell. Figure 6.6 (b), the SECCM

electrochemical activity map of HOPG, reveals fairly uniform activity across the surface, with current values similar to those in the initial values. Additionally, Figure 6.6 (c) shows uniform conductance current between the QRCEs in the barrels of the SECCM tip, indicating very stable meniscus contact and surface wetting, during imaging. From these maps we can readily conclude that the electrochemical reaction occurs easily at the basal surface of HOPG.

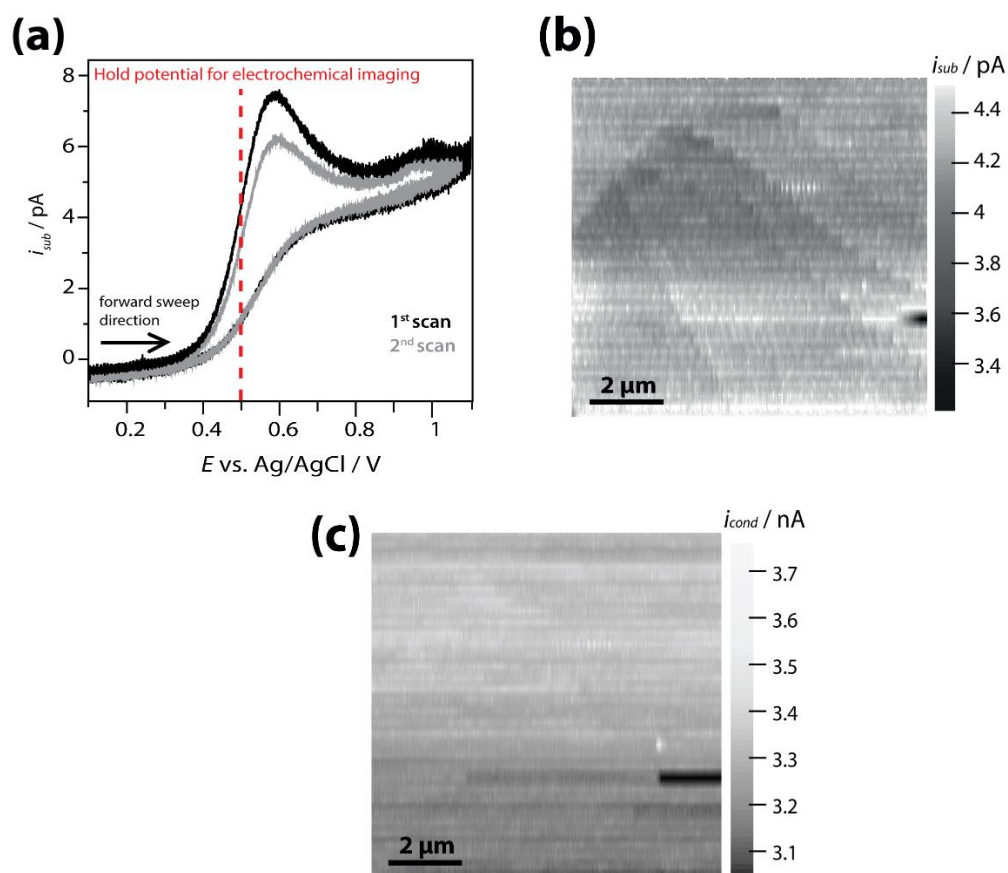


Figure 6.6. (a) SECCM CVs for the oxidation of 1 mM NADH in 0.1 M PBS at 100 mV s^{-1} . SECCM maps of (b) surface electrochemical activity and (c) conductance current (DC component) recorded at the half-wave potential for the oxidation of 1 mM NADH at HOPG (AM), obtained with a ca. 400 nm diameter pipette.

Next, pBDD electrode was considered. Figure 6.7 (a) (i) and (iii) show an optical image of the SECCM probe and electrode before and after an image. Using the in-rig camera, the area where the image was made is marked by the deposition of material. As mentioned in the experimental section, these measurements were run in a hopping-voltammetry mode (300 mV s^{-1}). This was possible because the extent of blocking of pBDD by NADH oxidation products is less extensive, although still occurs, as the positions where measurements were made were clearly revealed using FE-SEM by spot deposits left behind (Figure 6.7 (a) (ii)). These spots are fairly consistent and approximate to the tip size (Figure 6.7 (a) (iv)). After cleaning the pBDD surface, with FE-SEM the area in which an SECCM image was recorded was visualized. (Figure 6.7 (b) (i)). Previous FE-SEM studies confirmed that lighter and darker areas correspond to less-doped (more charging) and more-doped (less charging) facets respectively.^{56,58} Potential-resolved snap shots of electrochemical activity, from a series of images, at potentials of 0.5 V, 0.6 V and 0.7 V are shown in Figure 6.7 (b) (ii-iv). Close to the onset of the oxidation current (0.5 V), we begin to see the appearance of the more-doped facets on the electrochemical image, and as the working electrode potential is scanned positive, there is an increase in surface current, but particularly so in the more doped facets. Thus, for pBDD, the variation in the dopant level appear to have a significant impact on local electrochemical activity, as seen for a range of other reaction.^{24,56} This needs to be taken into account to understand the electrochemical properties of this material and particularly in the analysis of macroscopic and voltammetric data.

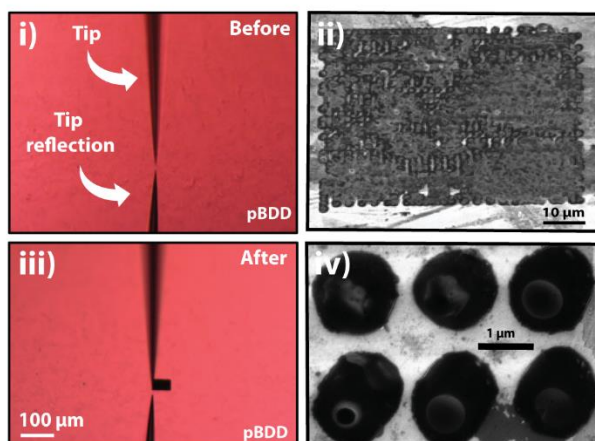
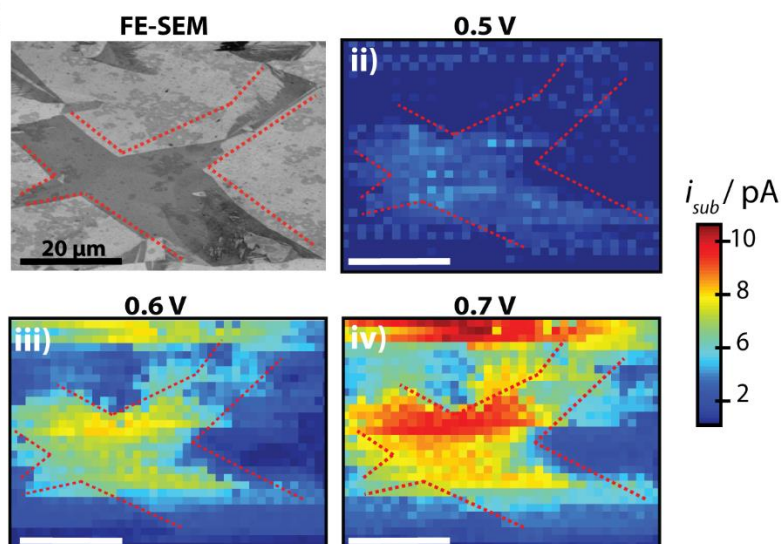
(a)**(b)**

Figure 6.7. (a) (i) Optical microscope image of the pBDD substrate, taken using the in-rig camera before performing the SECCM map and (ii) after scan. (iii) FE-SEM micrograph of the scanned area, covered by spots of reaction products formed during each local voltammetric scan. (iv) FE-SEM micrograph showing a zoom of typical spots after hopping voltammetric mode SECCM imaging. (b) (i) FE-SEM image of the same area of pBDD after cleaning to remove the adsorbed material. (ii-iv) Snap shot SECCM electrochemical maps ($60\ \mu\text{m} \times 45\ \mu\text{m}$) at different potentials, as marked above each map.

6.4. Conclusions

The voltammetric response of NADH at freshly cleaved HOPG and oxygen-terminated pBDD has been analyzed in detail at the macroscale using high-resolution electrochemical imaging. These two materials have relatively similar DOS, yet the electro-oxidation of NADH is much faster on the basal plane of HOPG than on pBDD. On the other hand, the electrochemical oxidation of NADH is a redox process complicated by side reactions. Oxidation products tend to adsorb onto the surface and as manifest in a deterioration of the electrochemical response, with this process occurring more extensively on HOPG than on pBDD. These effects need to be recognized and accounted for when considering the intrinsic behavior of these electrode materials.

The observations reported herein demonstrate that the electro-oxidation of NADH is facile at the basal plane of HOPG and independent of step edge density, as is the deterioration of the electrode response due to blocking by reaction products. The high intrinsic activity of the basal plane HOPG for these reactions has been demonstrated unequivocally using high resolution electrochemical imaging. An important new feature to NADH oxidation at sp^2 carbon electrodes revealed by this work is a contribution to the electrochemical response from adsorbed NADH, providing a further illustration of the potential importance of adsorbed reactants in electrochemistry at HOPG. The extent of adsorption (as inferred from the electrochemical signal) is enhanced at the highest quality (low step edge density) HOPG, i.e. is promoted by extensive basal surface regions.

In contrast to HOPG, electrochemical currents for NADH oxidation at pBDD electrodes are strongly correlated with the local boron dopant concentration in individual facets. This is an important issue that must be taken into account in order to gain a holistic view of pBDD electrochemical characteristics.

6.5. References

- (1) Lau, C.; Flechsig, G.-U.; Gründler, P.; Wang, J. *Analytica Chimica Acta* **2005**, *554*, 74-78.
- (2) Moiroux, J.; Elving, P. J. *Journal of the American Chemical Society* **1980**, *102*, 6533-6538.
- (3) Moiroux, J.; Elving, P. J. *Analytical Chemistry* **1979**, *51*, 346-350.
- (4) Moiroux, J.; Elving, P. J. *Journal of Electroanalytical Chemistry and Interfacial Electrochemistry* **1979**, *102*, 93-108.
- (5) Moiroux, J.; Elving, P. J. *Analytical Chemistry* **1978**, *50*, 1056-1062.
- (6) Musameh, M.; Wang, J.; Merkoci, A.; Lin, Y. *Electrochemistry Communications* **2002**, *4*, 743-746.
- (7) Gorton, L. *Electroanalysis* **1995**, *7*, 23-45.
- (8) Musameh, M.; Lawrence, N. S.; Wang, J. *Electrochemistry Communications* **2005**, *7*, 14-18.
- (9) Wooten, M.; Gorski, W. *Analytical Chemistry* **2010**, *82*, 1299-1304.
- (10) Ritzert, N. L.; Li, W.; Tan, C.; Rodriguez-Calero, G. G.; Rodriguez-Lopez, J.; Hernandez-Burgos, K.; Conte, S.; Parks, J. J.; Ralph, D. C.; Abruna, H. D. *Faraday Discuss* **2014**, *172*, 27-45.
- (11) Ratinac, K. R.; Yang, W.; Gooding, J. J.; Thordarson, P.; Braet, F. *Electroanalysis* **2011**, *23*, 803-826.
- (12) Chen, K.; Zhang, Z.-L.; Liang, Y.-M.; Liu, W. *Sensors (Basel, Switzerland)* **2013**, *13*, 6204-6216.

- (13) Lin, W.-J.; Liao, C.-S.; Jhang, J.-H.; Tsai, Y.-C. *Electrochemistry Communications* **2009**, *11*, 2153-2156.
- (14) Banks, C. E.; Compton, R. G. *Analyst* **2005**, *130*, 1232-1239.
- (15) Rao, T. N.; Yagi, I.; Miwa, T.; Tryk, D. A.; Fujishima, A. *Analytical Chemistry* **1999**, *71*, 2506-2511.
- (16) Nowall, W. B.; Kuhr, W. G. *Analytical Chemistry* **1995**, *67*, 3583-3588.
- (17) Samec, Z.; Elving, P. J. *Journal of Electroanalytical Chemistry and Interfacial Electrochemistry* **1983**, *144*, 217-234.
- (18) Blaedel, W. J.; Jenkins, R. A. *Analytical Chemistry* **1975**, *47*, 1337-1343.
- (19) Gorton, L. *Journal of the Chemical Society, Faraday Transactions 1: Physical Chemistry in Condensed Phases* **1986**, *82*, 1245-1258.
- (20) Gorton, L.; Domínguez, E. In *Encyclopedia of Electrochemistry*; Wiley-VCH Verlag GmbH & Co. KGaA, 2007.
- (21) Fujishima, A.; Rao, T. N.; Popa, E.; Sarada, B. V.; Yagi, I.; Tryk, D. A. *Journal of Electroanalytical Chemistry* **1999**, *473*, 179-185.
- (22) Patel, A. N.; Tan, S.-y.; Miller, T. S.; Macpherson, J. V.; Unwin, P. R. *Analytical Chemistry* **2013**, *85*, 11755-11764.
- (23) Kneten, K. R.; McCreery, R. L. *Analytical Chemistry* **1992**, *64*, 2518-2524.
- (24) Patten, H. V.; Meadows, K. E.; Hutton, L. A.; Iacobini, J. G.; Battistel, D.; McKelvey, K.; Colburn, A. W.; Newton, M. E.; Macpherson, J. V.; Unwin, P. R. *Angewandte Chemie International Edition* **2012**, *51*, 7002-7006.
- (25) Hutton, L. A.; Iacobini, J. G.; Bitziou, E.; Channon, R. B.; Newton, M. E.; Macpherson, J. V. *Analytical chemistry* **2013**, *85*, 7230-7240.

- (26) Chang, H.; Bard, A. J. *Journal of the American Chemical Society* **1991**, *113*, 5588-5596.
- (27) Zhang, G.; Cuharuc, A. S.; Guell, A. G.; Unwin, P. R. *Physical Chemistry Chemical Physics* **2015**, *17*, 11827-11838.
- (28) Zhang, G.; Kirkman, P. M.; Patel, A. N.; Cuharuc, A. S.; McKelvey, K.; Unwin, P. R. *Journal of the American Chemical Society* **2014**, *136*, 11444-11451.
- (29) Patel, A. N.; Collignon, M. G.; O'Connell, M. A.; Hung, W. O. Y.; McKelvey, K.; Macpherson, J. V.; Unwin, P. R. *Journal of the American Chemical Society* **2012**, *134*, 20117-20130.
- (30) Davies, T. J.; Moore, R. R.; Banks, C. E.; Compton, R. G. *Journal of Electroanalytical Chemistry* **2004**, *574*, 123-152.
- (31) McDermott, M. T.; McCreery, R. L. *Langmuir* **1994**, *10*, 4307-4314.
- (32) Bowler, R.; Davies, T. J.; Hyde, M. E.; Compton, R. G. *Analytical Chemistry* **2005**, *77*, 1916-1919.
- (33) Lai, S. C. S.; Patel, A. N.; McKelvey, K.; Unwin, P. R. *Angewandte Chemie International Edition* **2012**, *51*, 5405-5408.
- (34) Güell, A. G.; Cuharuc, A. S.; Kim, Y.-R.; Zhang, G.; Tan, S.-y.; Ebejer, N.; Unwin, P. R. *ACS Nano* **2015**, *9*, 3558-3571.
- (35) Tan, S.-y.; Zhang, J.; Bond, A. M.; Macpherson, J. V.; Unwin, P. R. *Analytical Chemistry* **2016**, *88*, 3272-3280.
- (36) Cuharuc, A. S.; Zhang, G.; Unwin, P. R. *Physical Chemistry Chemical Physics* **2016**, *18*, 4966-4977.

- (37) Frederix, P. L.; Bosshart, P. D.; Akiyama, T.; Chami, M.; Gullo, M. R.; Blackstock, J. J.; Dooleweerd, K.; de Rooij, N. F.; Staufer, U.; Engel, A. *Nanotechnology* **2008**, *19*, 384004.
- (38) Kim, Y.-R.; Lai, S. C. S.; McKelvey, K.; Zhang, G.; Perry, D.; Miller, T. S.; Unwin, P. R. *The Journal of Physical Chemistry C* **2015**, *119*, 17389-17397.
- (39) Lai, S. C. S.; Lazenby, R. A.; Kirkman, P. M.; Unwin, P. R. *Chemical Science* **2015**, *6*, 1126-1138.
- (40) Patel, A. N.; McKelvey, K.; Unwin, P. R. *Journal of the American Chemical Society* **2012**, *134*, 20246-20249.
- (41) Patel, A. N.; Tan, S.-y.; Unwin, P. R. *Chemical Communications* **2013**, *49*, 8776-8778.
- (42) Snowden, M. E.; Güell, A. G.; Lai, S. C. S.; McKelvey, K.; Ebejer, N.; O'Connell, M. A.; Colburn, A. W.; Unwin, P. R. *Analytical Chemistry* **2012**, *84*, 2483-2491.
- (43) Ebejer, N.; Schnippering, M.; Colburn, A. W.; Edwards, M. A.; Unwin, P. R. *Analytical Chemistry* **2010**, *82*, 9141-9145.
- (44) Macpherson, J. V.; Unwin, P. R. *The Journal of Physical Chemistry* **1994**, *98*, 1704-1713.
- (45) Rice, R. J.; McCreery, R. L. *Analytical Chemistry* **1989**, *61*, 1637-1641.
- (46) McDermott, M. T.; Kneten, K.; McCreery, R. L. *The Journal of Physical Chemistry* **1992**, *96*, 3124-3130.
- (47) Bowling, R. J.; Packard, R. T.; McCreery, R. L. *Journal of the American Chemical Society* **1989**, *111*, 1217-1223.
- (48) Edwards, M. A.; Bertocello, P.; Unwin, P. R. *The Journal of Physical Chemistry C* **2009**, *113*, 9218-9223.

- (49) Pumera, M. *Chemical Society Reviews* **2010**, 39, 4146-4157.
- (50) Chen, C.-H.; Jacobse, L.; McKelvey, K.; Lai, S. C. S.; Koper, M. T. M.; Unwin, P. R. *Analytical Chemistry* **2015**, 87, 5782-5789.
- (51) Compton, R. G.; Foord, J. S.; Marken, F. *Electroanalysis* **2003**, 15, 1349-1363.
- (52) Kraft, A. *International Journal of Electrochemical Science* **2007**, 2, 355-385.
- (53) Luong, J. H.; Male, K. B.; Glennon, J. D. *Analyst* **2009**, 134, 1965-1979.
- (54) Bard, A. J.; Faulkner, L. R.; Leddy, J.; Zoski, C. G. *Electrochemical methods: fundamentals and applications*; Wiley New York, 1980; Vol. 2.
- (55) Ebejer, N.; Guell, A. G.; Lai, S. C.; McKelvey, K.; Snowden, M. E.; Unwin, P. R. *Annu Rev Anal Chem (Palo Alto Calif)* **2013**, 6, 329-351.
- (56) Patten, H. V.; Lai, S. C. S.; Macpherson, J. V.; Unwin, P. R. *Analytical Chemistry* **2012**, 84, 5427-5432.
- (57) Banks, C. E.; Davies, T. J.; Wildgoose, G. G.; Compton, R. G. *Chemical Communications* **2005**, 829-841.
- (58) Wilson, N. R.; Clewes, S. L.; Newton, M. E.; Unwin, P. R.; Macpherson, J. V. *The Journal of Physical Chemistry B* **2006**, 110, 5639-5646.

Chapter 7

Conclusions

Fundamental understanding of the kinetics and mechanisms of dissolution and growth are very beneficial in the pharmaceutical science. Despite their importance and many years of research, the general processes governing dissolution and crystallization of crystals at the nanoscale need to be better understood, particularly for pharmaceutical crystals and other molecules. Thus, innovative approaches are highly desired. A major new aspect of the work in this thesis is the application of multi-microscopy systems and techniques to gain a holistic overview and understanding of dissolution and growth of pharmaceuticals. The combined use of a range of scanning probe microscopy and spectroscopy techniques, as well as complementary FEM simulations, have provided new insight into API dissolution and growth behaviour. Such methodologies allowed the study of dissolution from single crystal faces, from targeted regions of a crystal face/amorphous surface, and visualisation of the reactivity of whole crystals in real time.

Drugs with poor aqueous solubility demonstrate low oral bioavailability, which is a major challenge to pharmaceutical scientists. This has been one of the most critical issues in pharmaceutical industry for many years and, thus, chapter 3 focused on fundamental understanding of API dissolution, with a study of bicalutamide, as an exemplar. The combined use of AFM and FEM allowed the surface processes which accompany dissolution to be monitored in real time and dissolution kinetics to be obtained. Morphological changes and formation of pits associated with surface controlled dissolution were observed. AFM data were used to parameterise FEM model simulations of a dissolving BIC microcrystal to provide direct concentration distributions around and at individual crystal faces. As a result, determining the

importance of surface kinetic compared to mass transport for each crystal face was possible. Importantly, all BIC crystal faces showed surface kinetic controlled dissolution behaviour, being far from mass transport limited regime. However, the degree of mixed control changed dramatically during the process. This work has shown that, generally, the use of a single microcrystal drug can give a big insight in understanding drug dissolution kinetics and thus assist in the pharmaceutical formulation development of poorly soluble drugs.

One of the most significant approaches to enhance dissolution rates and achieve higher apparent solubility of drugs is the development of ASDs. In view of that, Chapter 4 uniquely demonstrated the use of a multi-microscopy approach to locally probe the aqueous dissolution process of ASD comprising of felodipine API and copovidone polymer in real time. It presented the use of a droplet-based electrochemical technique, a methodology that was previously shown to reveal considerable quantitative information on various surfaces and interfacial processes. Quad-probes made of quartz nanopipettes were used to monitor dissolution of two different formulations, one containing 15% w/w felodipine and the other of higher API dosage of 50% w/w. The droplet cell incorporating two working electrodes enabled localized dissolution flux measurements. A much-enhanced current response, for the detection of dissolving felodipine was observed for the 15 % drug loaded dispersion compared to the 50 % dispersion as dissolution initiated. These studies were complemented with *in situ* AFM and Raman spectroscopy that enabled mechanistic and kinetic insights on changes in the solid-state material during ASD dissolution. With Raman spectroscopy, the dissolution was monitored of both the API and polymer simultaneously. For the 50 % drug loaded dispersion, recrystallization of felodipine was observed. This was further proved by AFM studies, where change in topography was tracked over time and formation of particles on the surface was observed. In contrast, the Raman spectra recorded for the 15 % drug loaded dispersion did not show any significant changes during dissolution. This indicates that felodipine and copovidone dissolve as a single entity. Such observations and those seen at the nanoscale agreed well with other

findings emphasizing the importance of drug/polymer ratio in ASD formulations, where they influence the overall dissolution mechanism. Consequently, with this multi-microscopy approach, other ASD formulations of different API/polymer content could be investigated to further improve the understanding of ASD performance *in vivo*.

Focusing on the applications of nanopipette-based methods, chapter 5 demonstrated the use of nanopipettes as nanoreactors to study the crystallization of BIC in an antisolvent configuration (BIC in DMSO, mixed at the nanoscale with water). Voltage-controlled ion migration was used to mix two different solutions to induce crystallization at the nanopore interface generating oscillating current blockades. The frequency of these events and the extent of tip blockage was shown to be altered by variation in the potential bias and concentration of BIC in the bath. Monitoring crystallization in real time at the nanoscale provided unique information about the nucleation process, and indeed the analysis of formed crystals with Raman spectroscopy showed the formation of the metastable Form II BIC. Thus, the use of nanopipettes provides a simple, but powerful, way to form organic crystals of different polymorphs. Additionally, with this simple growth methodology one can examine the effect additives have on growth/dissolution rates.

Finally, Chapter 6, shows the robustness, unique capabilities and advantages of a droplet based technique showing the implementation of SECCM on other complex systems. Herein, SECCM was used in the study of NADH oxidation at bare surfaces of HOPG and pBDD; two carbon electrode materials possessing broadly similar densities of electronic states, but radically differ in *sp* hybridization and surface termination, and hence 3D structure. We have shown that the electrochemical oxidation of NADH is indeed a complex redox process and its oxidation is very much related to the history of the electrode surface used. Results showed unequivocally that the pristine HOPG surface, which has been previously described as supporting only sluggish electron transfer behaviour, or even as being completely inert has, in fact, considerable activity. Additionally, with SECCM it was possible to map grain

boundaries of pBDD and unambiguously observe no enhancement in activity for the oxidation of NADH compared to the grain surface. Due to SECCM's ability of obtaining localized droplet electrochemical measurements of which droplet size depends on the dimensions of the nanopipette, these novel observations of such complex system were made possible.

Overall, I hope that this thesis has given a unique scope on the use of microscopy and electrochemical techniques to study dissolution and growth of APIs. Introducing such methodologies, particularly nanopipettes, into the pharmaceutical domain can certainly lead to exciting new findings that can help to elucidate fundamental processes. The last results chapter further shows that the methods developed have wider application.